

Physical Conditions of Five O VI Absorption Systems Towards PG 1522 + 101

Sriram Sankar^{1*}, Anand Narayanan^{2†}, Blair D Savage³, Vikram Khaire⁴,
Benjamin E Rosenwasser³, Jane Charlton⁵, and Bart P Wakker³

¹*Department of Mechanical Engineering, Federal Institute of Science And Technology, Ernakulam 683577, Kerala, INDIA*

²*Department of Earth and Space Sciences, Indian Institute of Space Science & Technology, Thiruvananthapuram 695547, Kerala, INDIA*

³*Department of Astronomy, University of Wisconsin - Madison, Madison, WI*

⁴*Department of Physics, University of California, Santa Barbara 93106, California, USA*

⁵*Department of Astronomy & Astrophysics, The Pennsylvania State University, 525 Davey Laboratory University Park, PA, 16802, USA*

Accepted 2020 August 21. Received 2020 August 09; in original form 2020 May 18

ABSTRACT

We present the analysis of five O VI absorbers identified across a redshift path of $z \sim (0.6 - 1.3)$ towards the background quasar PG 1522 + 101 with information on five consecutive ionization stages of oxygen from O II to O VI. The combined *HST* and *Keck* spectra cover UV, redshifted EUV, and optical transitions from a multitude of ions spanning ionization energies in the range of $\sim (13 - 300)$ eV. Low ionization (C II, O II, Si II, Mg II) and very high ionization species (Ne VIII, Mg X) are non-detections in all the absorbers. Three of the absorbers have coverage of He I, in one of which it is a $> 3\sigma$ detection. The kinematic structures of these absorbers are extracted from C IV detected in *HIRES* spectra. The farthest absorber in our sample also contains the detections of Ne V and Ne VI. Assuming co-spatial absorbing components, the ionization models show the medium to be multiphased with small-scale density-temperature inhomogeneities that are sometimes kinematically unresolved. In two of the absorbers, there is an explicit indication of the presence of a warm gas phase ($T \gtrsim 10^5$ K) traced by O VI. In the remaining absorbers, the column densities of the ions are consistent with a non-uniform photoionized medium. The sub-solar [C/O] relative abundances inferred for the absorbers point at enrichment from massive Type II supernovae. Despite metal enrichment, the inferred wide range for [O/H] $\sim [-2.1, +0.2]$ amongst the absorbers along with their anti-correlation with the observed H I suggest poor small-scale mixing of metals with hydrogen in the regions surrounding galaxies and the IGM.

Key words: quasars: absorption lines – galaxies: haloes – galaxies: intergalactic medium

1 INTRODUCTION

Quasar absorption line observations remain one of the most sensitive tools for examining the diffuse gaseous component of the universe. At low redshifts ($z \lesssim 1$) such studies are particularly challenging as the gas beyond galaxies is inhomogeneously distributed over a broad temperature - density range. The circumgalactic medium (CGM) is one of the major reservoirs of such gas with L^* galaxies possessing halo baryonic masses of $\gtrsim 10^{10} M_\odot$ and collectively accounting for $\sim 25\%$ of the cosmic baryon budget at $z \sim 0$ (Peebles et al. 2014, Shull et al. 2014, Keeney et al. 2017, Hafen et al. 2019). Absorption systems featuring ions of low and high ionization energies show the CGM to be a richly multiphased region whose ionization, metallicity, and absorption ve-

locity spreads induced by temperature and turbulence, span a wide range of values (Richter et al. 2011, Werk et al. 2013, Fox et al. 2014, Liang & Chen 2014, Nuza et al. 2014, Richter et al. 2016, Tumlinson et al. 2017).

The multiphase properties are many a times brought out by the diversity of metal lines featured in spectroscopic observations. For example, the presence of a diffuse warm ($T \gtrsim 10^5$ K) component to the CGM is known through absorption from high ions such as O VI and Ne VIII, whereas concurrent detections of lower ionization species such as C II and Si II reveals much cooler $T \lesssim 10^4$ K CGM gas phases in the same environment (Savage et al. 2011, Narayanan et al. 2012, Pachat et al. 2017, Narayanan et al. 2018, Pradeep et al. 2020). The scale height of these low and high ions also serve to define a boundary to the chemically enriched CGM within the dark matter envelope of galaxies (Liang & Chen 2014, Liang et al. 2016, (See also Project AMIGA - Lehner et al. 2020). The metallicities inferred from the low and high ions and their kinematic properties

* E-mail: sriram10sankar@gmail.com

† E-mail: anand@iist.com

have also served as a tools to probe gas flows in and out of galaxies (Kereš et al. 2005, Lilly et al. 2013, Kacprzak et al. 2019). The properties of the CGM are also explored in great detail by hydrodynamic simulations. The recent emphasis in this direction has been in reproducing the wide scatter seen in cloud-to-cloud metallicities within the CGM, and also the differences in physical sizes of gas of various ionizations (Rauch et al. 2001b, Rauch et al. 2001a, Lopez et al. 2005, Misawa et al. 2013, Muzahid 2014, Churchill et al. 2015, McCourt et al. 2018). Given the complex kinematics, phase structure, and patchy metal distributions with the CGM, these simulations require resolutions of gas structures at sub-kiloparsec scales and the inclusion of sub-grid scale physical processes such as radiative cooling, stellar and AGN feedback, and accretion of gas in cold streams, to match the observed statistical properties of CGM absorption (Schaye et al. 2015, Oppenheimer et al. 2016, Oppenheimer et al. 2018, Peebles et al. 2019, Suresh et al. 2019, Hummels et al. 2019).

The gas beyond the extended halos of galaxies also possess a complex multiphase structure. A significant mass density of baryons in the intergalactic medium (IGM) is in the cool ($T \lesssim 10^4$ K) and diffuse phase, with a roughly equal amount at warm-hot ($10^5 \lesssim T \lesssim 10^7$ K) temperatures (e.g., Martizzi et al. 2019). The cool clouds heated through photoionization and with neutral fractions of $f_{\text{H I}} = N(\text{H I})/N(\text{H}) \sim 10^{-4}$ is probed well by the discrete Ly α forest absorption features seen in quasar spectra (Shull et al. 2012). Compared to this cool phase, resolving the phase structure of the warm-hot gas in the IGM has been challenging. Here again the observational strategy has been to focus on absorbers that feature O VI, Ne VIII, and BLAs (thermally broadened Ly α with $b(\text{H I}) > 40 \text{ km s}^{-1}$). A general challenge in this case, especially with O VI absorbers, is in discriminating photoionized gas from hotter collisionally ionized gas when the phases are kinematically overlaid. In such cases, detailed spectral line analysis and ionization modeling of the ions of different energy states help to segregate the neutral and low ionization phases from the high ionization gas traced by O VI (Narayanan et al. 2010, Narayanan et al. 2011, Pachat et al. 2016, Narayanan et al. 2018).

The intracluster medium (ICM), which dominates the baryonic mass in galaxy clusters, is also a strongly multiphased environment. Emission and absorption in X-rays are typically the probes for studying the $T \gtrsim 10^7$ K fully ionized ICM plasma. Quasar absorption lines, on the other hand, aid in detecting phases of the ICM that are cooler and denser, but with mass fractions comparable to that of the hot gas, especially in regions beyond the cluster virial radius (Emerick et al. 2015, Butsky et al. 2019). Observations of such $T \sim 10^4 - 10^5$ K ICM gas is a means to study important physical processes such as ram-pressure and tidal stripping of cluster galaxies, stellar and AGN feedback that push interstellar gas out into the ICM, as well as cold gas inflows through cosmic web filaments that penetrate into the cluster medium (Conselice et al. 2001, Ehlert et al. 2013, Zinger et al. 2016, Pradeep et al. 2019, Manuwal et al. 2019).

While H I and ionized metal transitions in the near and far-UV have been efficient in revealing diffuse gas with $T \sim 10^4 - 10^6$ K, the detection of hotter baryons ($T \sim 10^6 - 10^7$ K) have relied on X-ray emission studies of gas around individual massive galaxies ($M^* \sim 10^{11} M_{\odot}$), and also stacking X-ray measurements to detect diffuse emission further along the galactocentric radius (e.g., Anderson et al. 2013, Singh et al. 2018). Such studies show that the hot phase of the CGM accounts for only $\sim 8 - 10\%$ of the expected cosmic baryon fraction (Li et al. 2018). The baryon deficit is an indication that the CGM is multiphased with some significant

baryonic mass entrenched in cool/warm gas phases corresponding to accretion and feedback from star formation and AGN activity, although this in itself is not adequate to explain the shortfall in baryon fraction (Anderson & Bregman 2010). Dispersion measurements of millisecond duration Fast Radio Bursts (FRBs) is an emerging technique that can provide an ionization model independent account of the baryonic mass retained in the CGM and IGM. Macquart et al. (2020) recently reported an independent measurement of the cosmic baryon density, $\Omega_b = 0.051^{+0.021}_{-0.025} h_{70}$ (95% confidence) using the dispersion of a small sample of localized FRBs and thus confirming the existence of highly ionized gas and solving the missing baryons problem. Although a larger sample of localized FRBs are required to make more robust measurements and studies await the data from current and forthcoming facilities like Australian Square Kilometre Array Pathfinder (ASKAP), the Deep Synoptic Array (DSA) etc. (e.g., McQuinn 2014, Shull & Danforth 2018, Prochaska & Zheng 2019, Ravi 2019, Ravi et al. 2019, Macquart et al. 2020).

Irrespective of whether a given line of sight is probing halo gas, or the intra-group/cluster medium, or the clumpy mass distributions that characterize the filamentary IGM, an insight into the ionization states, densities and chemical compositions in the absorbing clouds is possible only when information on many ions diagnostic of the different gas phases is available. In this paper, we present the analysis of five distinct intervening metal line systems in the redshift interval $z = 0.6 - 1.3$ towards the background quasar PG 1522 + 101. Combining archival *HST*/COS, *HST*/STIS and Keck/HIRES observations, we have information on near-UV (NUV), far-UV (FUV) and extreme-UV (EUV) metal lines from nearly twenty different ionic species that represent a wide range of ionization energies from 13 eV - 350 eV, including the successive ionizations of oxygen from O II to O VI, and also C II to C IV, Ne V to Ne VIII and Mg X. Three of the absorbers also cover the EUV lines of He I at 584.334 Å, 537.029 Å, in one of which it is a $> 3\sigma$ detection.

Information on many ions spanning a continuous series of ionization energies is valuable for probing small scale density-temperature structures within the absorbing material that are otherwise difficult to detect. Furthermore, the multiple ionization stages of oxygen in the five systems presents the possibility of constraining [O/H] in O VI bearing gas, a parameter that is crucial in the estimations of the absorber population's contribution to the closure density [i.e., $\Omega_b(\text{O VI})$, Danforth & Shull 2005, Tripp et al. 2008, Savage et al. 2014]. From the perspective of absorber-galaxy associations, the line of sight probes diffuse gas spread over a redshift epoch that immediately follows the peak in global star formation rate. The increased rate of stellar winds and supernova feedback that ensue rapid star formation is expected to significantly enhance the covering fraction of metals around galaxies and alter the distributions of cold, warm and hot gas phases in their haloes at $z \lesssim 1$ (e.g., Simcoe et al. 2006, Wakker & Savage 2009, Tumlinson et al. 2011, Hummels et al. 2013, Barai et al. 2013, Peebles et al. 2014). The redshift range also encompasses the time period where spectroscopic imprints on the morphological evolution of galaxies towards the Hubble sequence can be seen from the kinematics of absorption lines directly probing gas within galaxy potential wells (Mshar et al. 2007, Rodríguez Hidalgo et al. 2012).

The paper is organized as follows. In Section 2, we provide information on the archival COS, STIS, and HIRES spectra and our data analysis methods. We begin the subsequent section by describing our approach to ionization modeling, the assumptions made and the choice of extragalactic ionizing background radiation. This is

followed by subsections where we address individual absorption systems in detail along with results from their modeling. In Section 9, we conclude with a discussion and summary of the results. The line measurements for all the ions and the system plots showing all available important transitions are included as appendix material.

2 SPECTROSCOPIC DATA IN THE UV & OPTICAL

The spectra for the QSO PG 1522 + 101 include archival data from *HST*/COS (Prog ID. 11741, PI. Todd Tripp), *HST*/STIS (Prog ID. 13846, PI. Todd Tripp) and Keck/HIRES (Prog ID. U066Hb, PI. Xavier Prochaska). Table 1 lists the parameters of the instruments used in our study. The COS FUV gratings G130M, and G160M and the NUV grating G185M offer a combined wavelength coverage from 1100 Å to 2100 Å with an average signal-to-noise ratio of $S/N \sim 10$ per 20 km s⁻¹ resolution element, after Nyquist sampling. The data were initially reduced with the CalCOS calibration pipeline. The CalCOS wavelength uncertainties of ~ 15 km s⁻¹ vary with wavelength and become as large as 40 km s⁻¹ at the edges of both detector segments. To improve the CalCOS wavelength calibration, a further set of customized velocity alignment and co-addition steps were applied, following the procedures described in detail in the appendix of Wakker et al. (2015). We recalibrate the CalCOS wavelengths in individual detector segment exposures by cross-correlating relatively strong and well observed galactic ISM lines in individual extractions of the same QSO to determine velocity offsets as a function of wavelength between the different segment observations. The different segment observations are then combined. The absolute wavelength scale is then established as a function of wavelength by comparing the velocities of ISM absorption lines with 21 cm H I emission spectra having high velocity accuracy. The full procedure produces final calibrated spectra with velocity errors estimated to be ~ 10 km s⁻¹. The final spectrum is an improvement over the coadded version available through the *HST* Legacy Archive¹. The STIS E230M grating has a spectral resolution of 10 km s⁻¹ over the wavelength range 1600 Å to 3100 Å but the data is of a lower S/N ratio compared to COS. The HIRES spectra were obtained from the Keck Observatory Archive (KOA)². The orders were extracted using the MAKEE package (MAuna Kea Echelle Extraction) written by T. Barlow³ and inverse variance weighted coaddition was performed to generate the final one-dimensional spectrum. The HIRES spectrum has a $S/N \sim 25$ per 7 km s⁻¹ resolution.

3 ANALYSIS OF ABSORPTION SYSTEMS & IONIZATION MODELING

The absorbers identified along this sightline are at $z = 0.67556$, $z = 0.72885$, $z = 1.09457$, $z = 1.16592$, and $z = 1.27768$, which would place them at $\Delta v \sim -95185$ km s⁻¹, $\Delta v = -86663$ km s⁻¹, $\Delta v = -31560$ km s⁻¹, $\Delta v = -21598$ km s⁻¹, and $\Delta v = -6552$ km s⁻¹ from the emission redshift of the quasar ($z = 1.32801 \pm 0.00044$) (Hewett & Wild 2010). The systems were identified from a search for O VI doublets along this sightline with simultaneous information on O II to O V offering a continuous range of diagnostics for

the gas phases in the absorbers. For the two absorbers at $z < 1$, the O V 629 Å line is below the COS G130M grating coverage. The cumulative *HST* and *Keck* spectra offer coverage of a large number of interesting ultraviolet and optical metal line transitions for all the absorbers. For instances where a given line is covered by multiple instruments, the spectrum with the best S/N ratio was used for analysis. Low order polynomials were used to fit the local continuum, avoiding evident absorption features. Equivalent width and profile measurements were carried out on the continuum-normalized spectra. The integrated column densities were measured using the apparent optical depth (AOD) method of (Savage & Sembach 1991) by converting velocity-resolved flux profiles of unsaturated lines into apparent column densities. For saturated lines, the AOD method provides a lower limit on the column density. Only those lines with a significance of $\gtrsim 3\sigma$ are considered as detected. For the others, useful upper limits are estimated from the 3σ equivalent width limits, obtained by integrating over the same velocity range as other prominent detected lines, and determining the corresponding column density from the linear regime of the curve-of-growth. Voigt profile fitting was also performed on these lines using the VPFIT routine (ver.10.4, (Carswell & Webb 2014)) after convolving the model profiles with the instrument line spread functions for COS⁴ and STIS and with a Gaussian of $v \sim 6.6$ km s⁻¹ for HIRES spectra. Multiple lines from a given ion are fitted together, with the fitting procedure optimizing on the unsaturated lines. This means that in the case of species like H I, the column density and b-value are predominantly constrained by the unsaturated higher order Lyman transitions. In the case of single lines that are saturated, fitting is done simultaneously with lines of similar ionization from other elements for which better constraints or multiple lines are available (e.g., C III and O III, C IV and O IV). In the three absorbers at $z > 1$, the C IV $\lambda\lambda 1548, 1550$ lines in the higher S/N and resolution HIRES data were used to establish the component structure of lines seen in the COS data. Components with velocity centroids that are within 10 km s⁻¹ (the velocity calibration uncertainty) are treated as coinciding in velocity. We adopt multi-component fitting for saturated lines such as Ly- α only when there is evidence of kinematic sub-components in the metal lines. The atomic line list and oscillator strength values used for fitting are from Morton (2003) for lines with $\lambda > 912$ Å and from Verner & Ferland (1996) for lower wavelengths.

Photoionization modelling using Cloudy(17.01) (Ferland et al. 2017) was carried out to derive the physical conditions and chemical abundances in the absorbers. The gas clouds are modeled as plane parallel slabs of constant temperature and density, with zero dust content. The ionization in the cloud is taken to be dominated by photoionization by the extragalactic UV background radiation at the absorber redshifts, for which we have used the model given by Khaire & Srianand 2019 (fiducial Q18 model; hereafter KS19). In Figure 1, we show the specific intensity ($4\pi\nu J_\nu$) of the KS19 background for the mean redshift of $\langle z \rangle \sim 0.99$ of our sample along with ionization energies of key species present in the absorbers. In addition, we also explore collisional ionizations caused by energetic free electrons colliding with atoms and ions using the models of Gnat & Sternberg 2007 as a potential source of ionization.

Assuming the solar relative elemental abundances of Asplund et al. 2009, photoionization simulations were run for the observed values of H I column density, and gas densities ranging from 10^{-6}

¹ <https://archive.stsci.edu/missions-and-data/hst-spectroscopic-legacy-archive-hsla>

² <https://koa.ipac.caltech.edu/cgi-bin/KOA/nph-KOAlogin>

³ <http://www.astro.caltech.edu/tb/makee/>

⁴ <http://www.stsci.edu/hst/instrumentation/cos/performance/spectral-resolution>

Instrument	Wavelength Coverage ^a (Å)	Spectral Resolution $R = \lambda/\Delta\lambda$	Velocity Resolution $\Delta v \text{ km s}^{-1}$	Exposure Time ^b t (ks)	S/N per resolution element ^c	Program ID
<i>HST</i> /COS ^d	1100 – 2100	12,000 – 20,000	17 – 20	54.60	5 – 20	11741, 13846
<i>HST</i> /STIS	1600 – 3100	~ 30,000	~ 10	20.88	4 – 11	13846
Keck/HIRES	3047 – 5895	~ 47,000	~ 7	00.80	10 – 25	U066Hb

Table 1. Table describes the instrument parameters of the archival data used in this study. ^a The wavelength range consists of different gratings and frames and thus small coverage gaps in between. ^b Total exposure time listed is the sum of multiple observations with multiple instrumental settings. ^c The S/N in each line profile can be estimated from the noise level plotted at the bottom of each panel illustrated in Figures 3A to 7A. ^d The COS LSF has broad non-Gaussian wings which affects the measurements on narrow and closely separated line features.

to 10^{-1} cm^{-3} . A suite of ionization models were generated by varying metallicities over a wide range to determine the physical conditions that best explains the observed column densities and the temperatures implied by the line widths. Multiple components in an absorber are modeled separately. Absorption components of different ions that are aligned in velocity (within 10 km s^{-1} of each other) are considered together for a single phase model. In such cases, multiphase models are sought only when the observed column densities are significantly different from the predictions from a narrow range of density phase solutions with reasonable relative elemental abundance variations. The abundances we derive based on the ionization models will carry uncertainties from the H I and metal line column densities in addition to the uncertainty in the shape of the EBR. The latter can induce errors of ~ 0.5 dex in the derived metallicities (Howk et al. 2009).

In cases where the centroid velocities of the lines and their Doppler b parameters imply a single phase, the best constraints on the physical conditions are provided by the column density ratios between adjacent ionization stages of oxygen. In Figure 2 is shown the observed column densities of the oxygen ions in the five absorbers. General conclusions can be drawn on the ionization based on a comparison of these successive ionic column densities. In four out of five of these absorbers the $N(\text{O IV}) > N(\text{O V}) > N(\text{O III}) > N(\text{O VI})$ ⁵. This trend is valid under photoionization equilibrium at gas densities in the range of $n_{\text{H}} = (0.2 - 2) \times 10^{-3} \text{ cm}^{-3}$. Here the lower bound is set by the $N(\text{O IV}) > N(\text{O V}) > N(\text{O VI})$, and the upper bound by $N(\text{O IV}) > N(\text{O III})$. In all these absorbers, therefore, the low to high ionization stages of oxygen can exist in photoionized gas with densities that are within an order of magnitude of each other. This is only a general estimate, and does not involve the nuanced phase structure these absorbers can have with the O VI predominantly from gas that is significantly ionized compared with the intermediate ions such as O III and O IV.

Since the high ions, especially O VI, can have an origin in warm collisionally ionized plasma, we consider the predictions from such models as well. In Figure 2, we show the column density predictions of O IV, O V, and O VI in a cloud of solar metallicity and arbitrary H I column density, for temperatures at which equilibrium (CIE) and non-equilibrium collisional ionizations (NECI) are significant. The computations are based on the models of Gnat & Sternberg (2007). As seen in Figure 2, at $T < 5 \times 10^6 \text{ K}$ the O V and O VI predictions under NICE depart significantly from their CIE values, with the column density predictions differing by > 1 dex. The presence of metals enhances the cooling rate of the

plasma significantly. The temperature of the gas declines faster with the recombination between ions and electrons lagging behind. This results in enhanced high ion fractions at lower temperatures in comparison with CIE. With decrease in metallicity, the difference between CIE and NECI predictions tend to get less. Furthermore, even at temperatures where collisions tend to dominate the ionization, photoionization from the extragalactic background radiation can raise the ionization levels of gas to some degree (Oppenheimer & Schaye 2013). These aspects are also considered in our analysis of the absorbers. In the subsequent sections, we discuss the ionization models for each absorber in detail, the results of which are summarized in Table 2. The full system plots (Appendix Figures from B1 to B5) and table of measurements (Refer Appendix Tables from B1 to B10) are listed in the appendix section.

The QSO PG 1522 + 101 was observed as part of an HST program to study Ne VIII bearing warm-hot gas, which excluded lines of sight with strong Lyman Limit Systems. The target selection may have led to a bias towards high ionization absorbers. However, low ionization phases traced by C II, O II, Si II are commonly detected in intervening O VI and Ne VIII systems (e.g., Narayanan et al. 2012, Meiring et al. 2013, Hussain et al. 2015, Pachat et al. 2017, Rosenwasser et al. 2018). The simultaneous non-detections of low ions and Ne VIII in the O VI absorber sample presented here can be suggestive of the absorbers probing relatively narrow density-temperature phase structures.

4 THE $Z_{\text{ABS}} = 0.67556$ ABSORBER

4.1 Characterization of the $z_{\text{abs}} = 0.67556$ absorber

This is the lowest redshift O VI absorber along this sightline that we report on. The absorber has detections of O III, O IV, and O VI. The redshifted O V 629 line is below the far-UV coverage of COS. The system plot for this absorber is shown in Figure 3A (the full version in Appendix Figure B1) and the line measurements are listed in Appendix Tables B1 and B2. In addition to the oxygen lines, the COS spectrum also shows C III. Key species including C II, N II, O II, Al II, Si II, N III, Al III, Si III, and Ne VIII are non-detections. The C IV 1548 line is affected by contamination from Galactic Mn II 2594. The C IV 1551 line is detected as a weak feature. The high S/N HIRES data shows the Mg II $\lambda\lambda 2796, 2803$ lines as non-detections, consistent with the non-detections of C II, O II, and Si II lines in the COS data, since these low ions have similar ionization potentials. The AOD integrated column densities of the various oxygen lines are comparable to their Voigt profile fitted values to within 1σ uncertainty, indicating that unresolved saturation is either absent or not significant. The absorption in O III and

⁵ O V covered and detected only in the $z = 1.09457$, $z = 1.16592$ and $z = 1.27768$ absorbers.

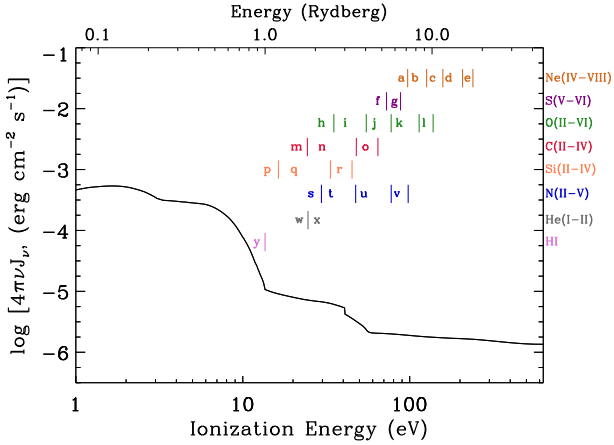


Figure 1. SED of the extragalactic background radiation (KS19, Khaire & Srianand (2019)) which is an improvement over the Haardt & Madau (2001) model as it incorporates the most recent measurements of the quasar luminosity function (Croom et al. 2009, Palanque-Desabrouille et al. 2013) and star formation rate densities (Khaire & Srianand 2015). The vertical tick marks signify the creation and destruction energies of key species covered in our sample of absorbers.

C III coincides with H I, but is centered 25 km s⁻¹ from O IV and O VI (see Figure 3B). Such velocity offsets between high and low ions is common to many O VI absorbers (e.g., Savage et al. 2011, Fox et al. 2013) and are thought to occur when the line of sight is probing a flow of warm interface gas between a cold cloud and a hot surrounding medium (Boehringer & Hartquist 1987, Savage & Lehner 2006).

Neutral hydrogen is detected in a number of Lyman series lines. The unsaturated H I lines from 937 to 919 Å and the non-detections of higher order transitions constrains the H I column density to $\log [N(\text{H I}), \text{cm}^{-2}] = 15.87 \pm 0.04$, and b -parameter to $b(\text{H I}) = 37 \pm 2 \text{ km s}^{-1}$. The H I and metal line absorption profiles in this systems are modeled with a single component since there are no adequate constraints in the data to adopt a rigid multi-component model. Kinematic sub-components that are unresolved by COS or STIS, if present, will be an additional source of uncertainty in the temperature and ionization model parameters we infer. The wings of the Ly α between $75 < v < 175 \text{ km s}^{-1}$ is contaminated by the Ly γ feature associated with the $z = 1.09457$ O VI absorber (refer Appendix Figure B3). The system plot of Figure 3A shows the extent of this contamination. As mentioned earlier, the H I, C III, and O III lines have an offset of $\Delta v \sim 25 \text{ km s}^{-1}$ relative to the O IV and O VI. The offset is evident in the apparent column density comparison plots of Figure 3B. The O IV 787 line, covered by the G130M grating of COS, occurs in between the O III 702 and O III 832 lines. The O III lines are well aligned relative to each other, but offset from the O IV. Furthermore, the O IV 787 observed by the G130M grating is well aligned with the O VI doublet lines that appear at the edge of the G160M spectrum. The velocity difference is therefore unlikely to be an artifact of COS wavelength calibration. Such offsets between O VI and ions of lower ionization is usually an indication of multiphased gas, a possibility we consider during the ionization modeling of the absorber. The H I lines are only as broad as the well-aligned C III and O III lines indicating a predominance of non-thermal broadening. The $b(\text{H I}) = 36 \pm 2 \text{ km s}^{-1}$, and $b(\text{C III}) = 33 \pm 6 \text{ km s}^{-1}$ imply a $T < 4.7 \times 10^4 \text{ K}$ based on the 1σ uncertainties in b . The

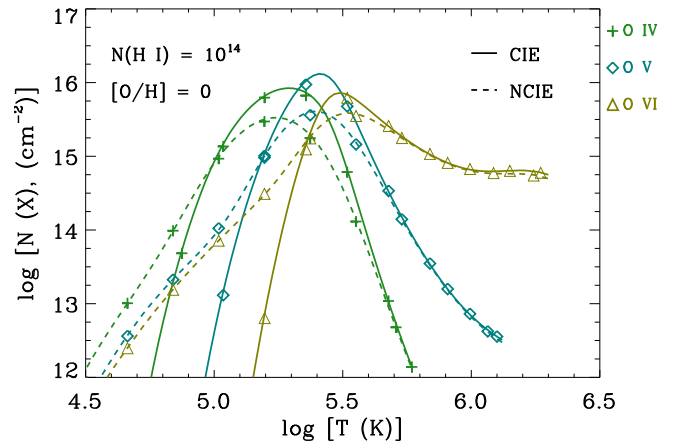
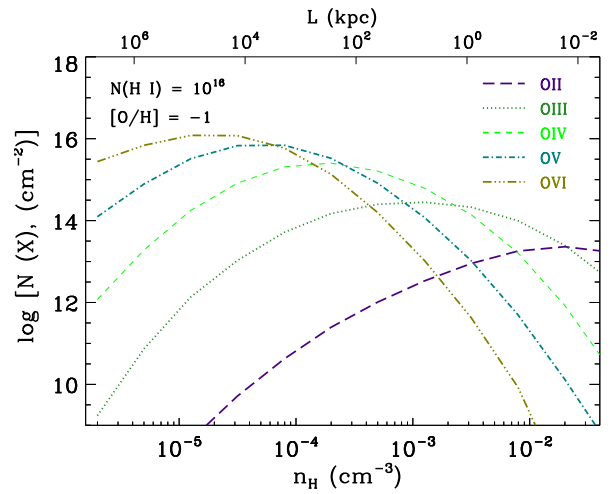
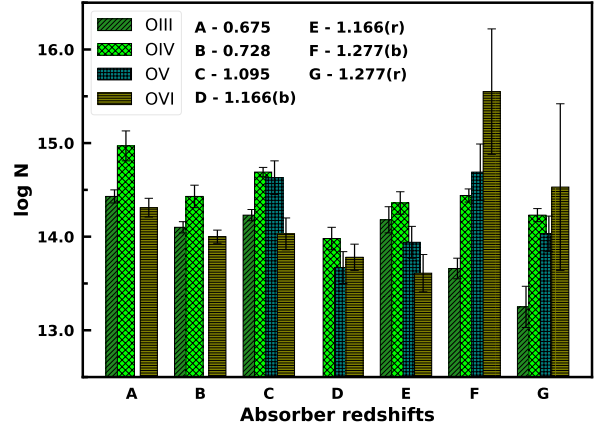


Figure 2. *Top* panel shows comparison of the column densities of the different oxygen ions in the five absorbers. In the $z = 1.165$ and $z = 1.277$ absorbers, the negative and positive velocity components are separately measured and indicated as "b" and "r". The O v is not covered by the COS spectra for $z < 1.09$. The panel on the *middle* shows a fiducial PIE model computed for an average value of $\log N(\text{H I})$ for our sample, an oxygen abundance of one-tenth solar, and an ionizing background corresponding to the mean redshift of our sample. The different curves are the PIE model predicted column densities for the five successive ionization stages of oxygen. *Bottom* panel shows the column densities of O IV, O V, and O VI in a cloud of solar metallicity and $N(\text{H I}) \sim 10^{14} \text{ cm}^{-2}$, for the range of temperatures at which collisional ionization equilibrium (CIE) and non-equilibrium collisional ionizations (NECI) are significant. The computations are based on the models of Gnat & Sternberg (2007)

$b = 39 \pm 11 \text{ km s}^{-1}$ for the kinematically offset O VI places a much higher limit of $T < 2.5 \times 10^6 \text{ K}$ for the O VI bearing gas.

4.2 Ionization Models for the $z_{abs} = 0.67556$ absorber

The photoionization model results are shown in Figure 3C. The observed $N(\text{C III})/N(\text{C IV}) = 0.07 \pm 0.27$ is used to constrain the density at $n_{\text{H}} \sim (0.2 - 0.7) \times 10^{-3} \text{ cm}^{-3}$. The column density predictions from the PIE models yield an $[\text{O}/\text{H}] = -0.9 \pm 0.1$ for the O III to be produced at the mean of that density range, with the uncertainty in the metallicity a cumulative of the measurement errors in H I and O III. The predicted column density ratio of C III to O III is a constant over two orders of magnitude in density ($n_{\text{H}} \sim 10^{-4} - 10^{-2} \text{ cm}^{-3}$), indicating that these two species would trace the same phase of the absorber. The observed column densities of these ions thus offer a direct insight into the relative elemental abundance between C and O. For the model predicted C III and O III column densities to match their observed values at the mean density of $n_{\text{H}} \sim 0.5 \times 10^{-3} \text{ cm}^{-3}$, the PIE models require $[\text{C}/\text{O}] = -0.5 \pm 0.2 \text{ dex}$. For this phase, the PIE models also predict the observed C IV and O IV to within their 1σ uncertainty. The O VI however is under-produced by $\sim 0.75 \text{ dex}$. The column density ratio plot of Figure 3C also reflect this where the observed O IV to O VI column density ratio matches with its model predicted value at a density of $n_{\text{H}} = 0.2 \times 10^{-3} \text{ cm}^{-3}$ which is about five times lower. The line of sight could be tracing a column of gas with a narrow spread of densities from $n_{\text{H}} = (0.2 - 0.7) \times 10^{-3} \text{ cm}^{-3}$ where all the observed metal ions are produced (yellow zone in Figure 3C). This density range also constraints the total hydrogen column density to within $\log N(\text{H}) = 19.93 - 19.20 \text{ cm}^{-2}$, gas temperatures to $T = (2.9 - 2.2) \times 10^4 \text{ K}$, pressure of $p/K = (4.6 - 15.9) \text{ cm}^{-3} \text{ K}$, and thickness along the line of sight of $L = (172.4 - 7.2) \text{ kpc}$. Such a medium is also consistent with the non-detections of C II, Si II, and Mg II, that are generally tracers of denser and more compact gas.

However, the $\Delta v \sim 25 \text{ km s}^{-1}$ velocity offset of O VI and O IV with O III, C III and H I implies at least two distinct gas phases. The bulk of the O VI could be from gas at $T > 10^5 \text{ K}$ where collisions dominate the ionization. The $b(\text{O VI}) = 39 \pm 11 \text{ km s}^{-1}$ suggests that the temperature in this O VI phase can be as high as $T < 2.5 \times 10^6 \text{ K}$ (1σ upper limit), assuming negligible non-thermal broadening. Such a warm/hot phase can contribute significant amounts of O IV as well. It is difficult to disentangle the separate contributions to the observed O IV from the photoionized and collisionally ionized phases. The O IV absorption coinciding in velocity with O VI points to a significant portion of the O IV coming from the O VI phase. Nonetheless, we consider the O IV to O VI observed column density ratio as an upper limit while constraining the warm O VI phase. In gas that is subjected to CIE, the observed $\log[N(\text{O IV})/N(\text{O VI})] \leq 0.66$ is valid for $T > 0.3 \times 10^6 \text{ K}$ as shown by the collisional ionization models of Figure 3C. Given the low neutral fraction at such temperatures ($f_{\text{H I}} = 1.95 \times 10^{-6}$, [Gnat & Sternberg 2007](#)), the H I from this phase is expected to be a shallow feature, with a $b(\text{H I}) \geq 64 \text{ km s}^{-1}$ corresponding to a $T > 0.2 \times 10^6 \text{ K}$ from the H I - O VI combined b -parameters. Figure 3A shows the possible presence of such a broad-Ly α (BLA). The BLA column density has to be $\log N(\text{H I}) \leq 13.7$ for the cumulative model profile to not exceed the absorption seen in Ly α and the higher Lyman transitions. At this limiting temperature, the observed $N(\text{O VI})$ is reproduced by the CIE models for a $[\text{O}/\text{H}] = -0.9$, identical to the abundance derived for the cooler photoionized phase using O III as the constraint. The abundance is not ad-

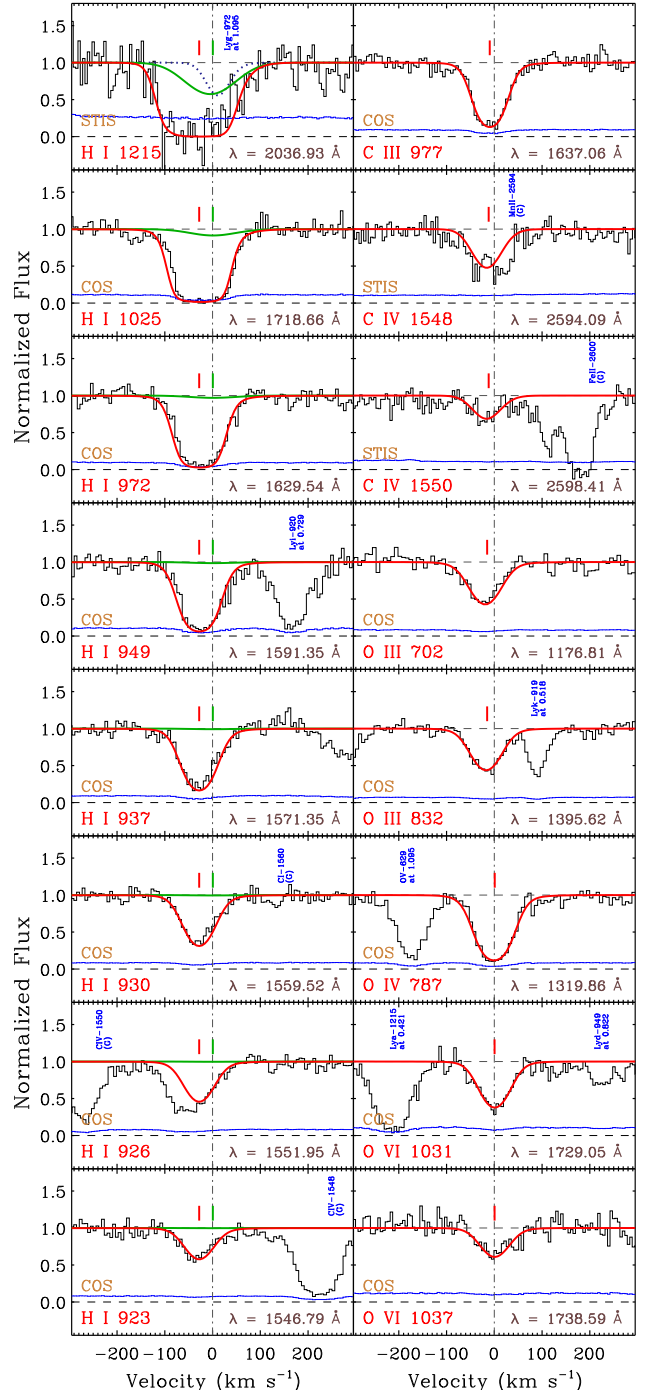


Figure 3A. System plot of the $z_{abs} = 0.67556$ absorber, with continuum-normalized flux along the Y-axis and the velocity scale relative to the redshift of the absorber along the X-axis. The $v = 0 \text{ km s}^{-1}$, marked by the dashed-dotted vertical line, indicates the absorber redshift. The 1σ uncertainty in flux is represented by the blue curve at the bottom of each panel. The red curves are the best-fit Voigt profiles. The observed wavelength of each transition is also indicated in the respective panels. Interloping features unrelated to the absorber are labeled. In the Lyman Lines panels, the synthetic profile of a BLA with $\log N(\text{H I}) = 13.7$ and $b(\text{H I}) = 80 \text{ km s}^{-1}$ associated with O VI is also shown (green solid curve). The blue dashed curve in the Lyman α panel shows the contaminating feature of Lyman γ of the absorber at 1.09457.

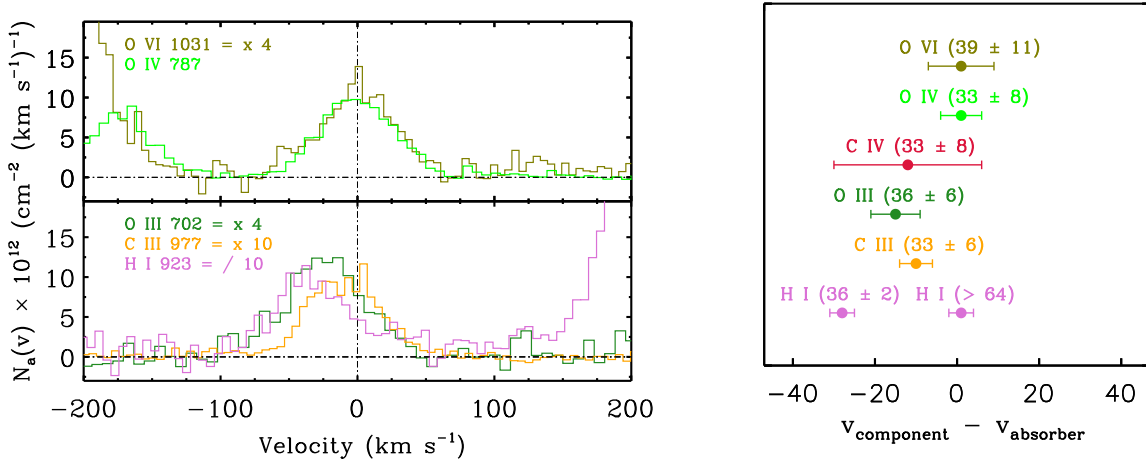


Figure 3B. Apparent column density comparison between the different detected species of the $z_{abs} = 0.67556$ absorber. The high ions are plotted on the top panel and the intermediate ions on the bottom panel. An offset of 25 km s^{-1} is seen between the intermediate and high ions. The b parameter of O VI also appears to be a bit higher than the other species. The figure on the right shows the velocity centroids of each line with their uncertainty relative to the absorber redshift, as derived from profile fitting. The b -parameter measured for the various ions are indicated within the parentheses.

equately constrained due to lack of information on the exact temperature of the O VI gas, and the H I associated with the O VI. The BLA properties are comparable to the characteristic value predicted for absorption tracing hot circumgalactic gas around galaxies with virial halo masses of $\log(M/M_{\odot}) \sim 10^{11}$ (Richter 2020).

An alternative is for the O VI to be produced via photoionization. Assuming a $\log[N(\text{H I})/\text{cm}^{-2}] = 13.7$, the PIE models require oxygen abundance to be at least $[\text{O}/\text{H}] \geq -0.5$, with a corresponding density lower limit of $\log[n(\text{H}), \text{cm}^{-3}] \geq -5.0$, with higher densities requiring higher metallicities. The $[\text{O}/\text{H}]$ thus estimated is assuming $\log[N(\text{H I})/\text{cm}^{-2}] = 13.7$ corresponding to the upper limit in the column density of the BLA. Lower values of $N(\text{H I})$ for the BLA would require higher $[\text{O}/\text{H}]$ for the O VI to be recovered. The PIE model for the lower limit on density yields a temperature of $T = 4.9 \times 10^4 \text{ K}$, which predicts a thermal line width of $b \sim 7 \text{ km s}^{-1}$ that is a factor of ~ 4 less than the observed $b(\text{O VI})$. The metallicity will have to be super-solar for the O IV to be produced at detectable levels from this photoionized O VI phase. This would also mean that the photoionized low and high phases would have a metallicity gradient of more than an order of magnitude. Metallicity differences of as much as ~ 1 dex between aligned components have been reported before (Prochter et al. 2010, Tripp et al. 2011, Crighton et al. 2013, Rosenwasser et al. 2018, Lehner et al. 2019, Zahedy et al. 2019). The differences often stem from the low and high ions tracing gas of different enrichment history, particularly when the line of sight is probing material proximate to galaxies where superwinds and AGN outflows can create patchy metal distributions (e.g., Zonak et al. 2004, Veilleux et al. 2005). An alternative explanation involves the intermediate ions tracing photoionized gas, and the O VI (and some substantial fraction of O IV) coming from a warm ($T \gtrsim 3 \times 10^5 \text{ K}$) higher ionization phase with a metallicity similar to the photoionized gas.

5 THE $Z_{ABS} = 0.72885$ ABSORBER

5.1 Characterization of the $z_{abs} = 0.72885$ absorber

The system plot displaying the key transitions in this absorber is shown in Figure 4A (the full version is available in Appendix Figure B2) and line measurements are given in Appendix Tables B3 and B4. The absorber has C III, O III, O IV, and O VI ions detected at $\geq 3\sigma$. Apparent column density comparison between the detected lines is shown in the *top* panel of Figure 4B. The O VI 1037 Å line is severely contaminated by O IV 787 from $z = 1.277$ and Ly α from $z = 0.475$. We consider the absorption at $\lambda = 1784.05 \text{ \AA}$ as O VI 1031 Å. The feature is weaker and more spread out compared to any of the other detected ions (see $N_a(v)$ comparison of Figure 4B). Equivalent width estimation over the velocity range in which absorption is seen shows the feature to be of $\gtrsim 3\sigma$ significance.

A Voigt profile model recovers the same column density as the integrated apparent column density with a $b(\text{O VI}) = 61 \pm 11 \text{ km s}^{-1}$. In the absence of unidentified line contamination, or unresolved component structure, which we cannot rule out, the broader kinematic profile of O VI implies an origin in a separate phase with $T < 5.0 \times 10^6 \text{ K}$ compared with other metal ions and H I which are considerably narrower and hence tracing cooler gas.

The Mg II $\lambda\lambda 2796, 2803$ lines covered by HIRES and the C IV $\lambda\lambda 1548, 1550$ from STIS are non-detections. The absence of Mg II in the higher S/N HIRES spectrum, is consistent with the non-detections of C II, N II, O II and Si II in the COS and STIS data, as all these ions possess similar ionization potentials. It further alludes to the absence of a prominent high density ($n_{\text{H}} > 10^{-3} \text{ cm}^{-3}$) low ionization phase in the absorber. Similarly, the non-detections of C IV and N IV, despite the presence of a comparatively strong O IV, hints at non-solar $[\text{C}/\text{O}]$ and $[\text{N}/\text{O}]$ in the absorbing gas. The narrow weak feature coinciding with the expected location of Ne VIII 770 is identified as N V 1238 from $z = 0.075$, confirmed by the presence of H I 1215, and C IV $\lambda\lambda 1548, 1550$ lines from the same redshift.

The full range of Lyman series lines are covered by the combined COS and STIS data. A simultaneous fit to these lines with a

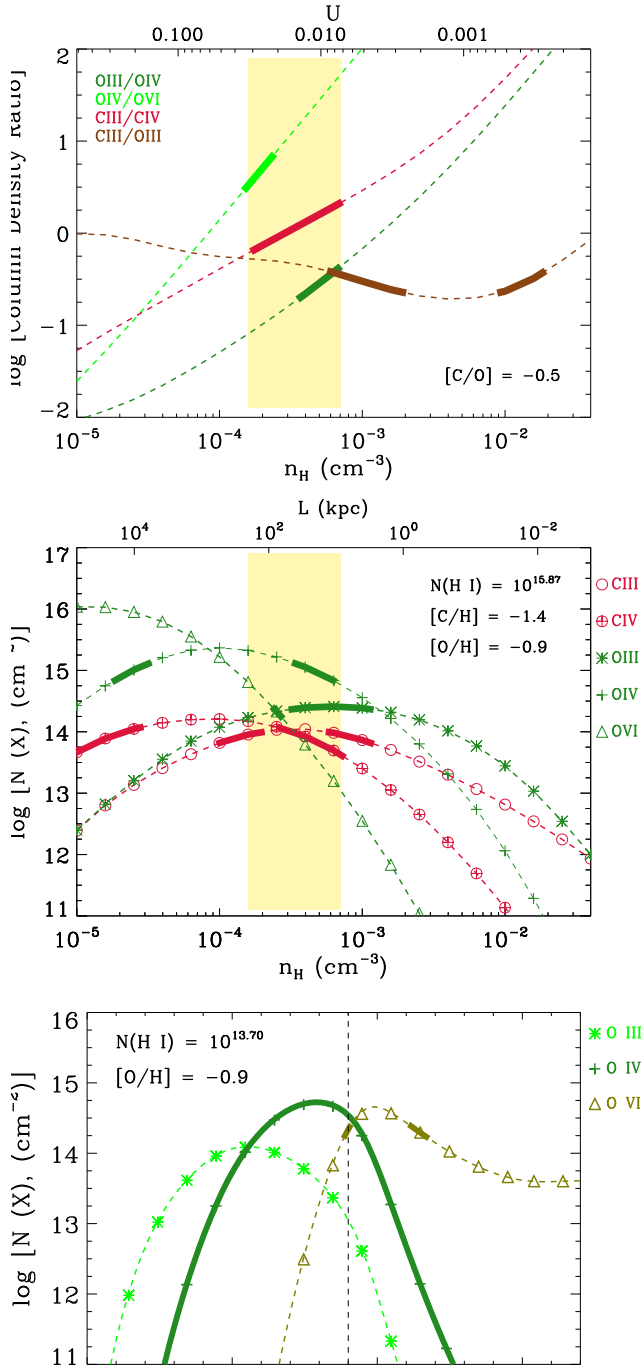


Figure 3C. Photoionization models for the $z_{abs} = 0.67556$ absorber. On the *top* panel is shown the model predictions (*thin* lines) and the observed (*thick* lines) column density ratios between ions plotted against gas density. These ratios confine the gas density to the narrow range indicated by the *yellow* strip. On the *middle* panel are predictions of column densities (*thin* lines) along with their 1σ observed values (*thick* lines). The density range allowed by the column density ratios is represented by the *yellow* region. The elemental abundances in the models are varied to reproduce the observed column densities from a single or nearly similar gas phases. The ionization parameter (u) and line of sight thickness for a given density are given by the *top* X-axis of the panels. The *bottom* panel shows column density predictions from CIE models for different equilibrium temperatures. The vertical dashed line in the bottom panel marks the temperature at which the observed column density ratio between O IV and O VI is recovered by the CIE models.

single component yields $\log [N(\text{H I})] = 16.50 \pm 0.02 \text{ cm}^{-2}$ and $b(\text{H I}) = 26 \pm 2 \text{ km s}^{-1}$. The $\text{Ly}\alpha$ and $\text{Ly}\beta$ features span a broad kinematic range of -100 to 200 km s^{-1} with the metals coinciding in velocity with the stronger component. The weaker H I absorption at $v \sim +150 \text{ km s}^{-1}$ is modeled using a single component profile as shown in Figure 4A. While constraining the metallicity of the absorbing gas, we consider the column density of H I that is coincident with the metal lines. The obtained value of $N(\text{H I})$ is slightly lower than the value quoted by Lehner et al. (2013) and Wotta et al. (2016) (16.66 ± 0.05). We proceed with our measurement which is constrained by a large number of Lyman transitions. The $b(\text{H I}) = 26 \pm 3 \text{ km s}^{-1}$ and $b(\text{O III}) \sim b(\text{C III}) = 17 \pm 3 \text{ km s}^{-1}$ yield a temperature of $T = (0.8 - 4.3) \times 10^4 \text{ K}$ in this intermediate ion phase, which is two orders of magnitude lower than the temperature upper limit implied by the broad O VI.

5.2 Ionization Models for the $z_{abs} = 0.72885$ absorber

The PIE model predictions for this absorber are given in Figure 4C. The constraints imposed by the column density ratio between O III, and O IV suggest the gas density to be $n_{\text{H}} = 7 \times 10^{-4} \text{ cm}^{-3}$, if the two ions are predominantly from the same gas phase. The observed ratio between C III and O III, both of which are measurements from unsaturated lines, is also valid at this density when the relative abundance is $[\text{C}/\text{O}] = -0.8 \pm 0.1$ dex. The column density predictions from the PIE models yield an $[\text{O}/\text{H}] = -2.0 \pm 0.1$ with the uncertainty in metallicity being a cumulative of the measurement errors in H I and O III. At lower abundances, C III and O III will be under-produced at all densities, whereas higher abundances will not yield a model solution that explains the intermediate ions. This phase with $n_{\text{H}} = 7 \times 10^{-4} \text{ cm}^{-3}$ results in $\log N(\text{H}) = 20.03 \text{ cm}^{-2}$, $T = 2.7 \times 10^4 \text{ K}$, $p/K = 18.3 \text{ cm}^{-3} \text{ K}$ and $L = 59.14 \text{ kpc}$. Lehner et al. 2013 estimate the absorber to be a complex multi-phase system with the lower ionization phase arising from $n_{\text{H}} < 1.26 \times 10^{-3} \text{ cm}^{-3}$ and $[\text{X}/\text{H}] < -2.0$. These metallicity and density upper limits are consistent with the values we infer. However, the solar $[\text{C}/\alpha]$ which they report is inconsistent with our findings. They used the non-detection of Mg II to estimate $[\text{C}/\alpha]$ while we use the detected C III to O III column density ratio, which is nearly uniform in photoionized gas over five orders of magnitude in density (see *top* panel of Figure 4C), and hence a better tracer of relative elemental abundance.

The column density of O VI predicted from the PIE model described above is an order of magnitude lower than its observed value. The significantly broader O VI profile compared to the narrow metal ions and H I suggest the presence of an additional gaseous component at $T < 5 \times 10^6 \text{ K}$. The H I in this highly ionized phase should produce a BLA absorption with $b(\text{H I}) < 280 \text{ km s}^{-1}$. The presence of such a broad H I is not evident in the $\text{Ly}\alpha$, suggesting that the feature could be too weak to be detected against the strength of the absorption from cooler gas. Specific constraints on this gas phase, such as its $[\text{O}/\text{H}]$ or exact temperature cannot be gleaned from the O VI profile alone.

From the analysis, one can only conclude that there is a dominant cool photoionized medium in this absorber with $[\text{C}/\text{O}] \sim -0.8$ dex, and a warm/hot phase traced by the O VI. The broad O VI is similar to the $T = (0.6 - 1.6) \times 10^6 \text{ K}$ O VI reported in Savage et al. (2010) where the broad $\text{Ly}\alpha$ absorption with a predicted $b(\text{H I}) \sim 150 \text{ km s}^{-1}$ was too weak to be detected. The absorber, in that instance, was hypothesized as tracing either a hot intergalactic gas filament or the circumgalactic medium of a pair of luminous galaxies at impact parameters of $\rho \lesssim 120 \text{ kpc}$.

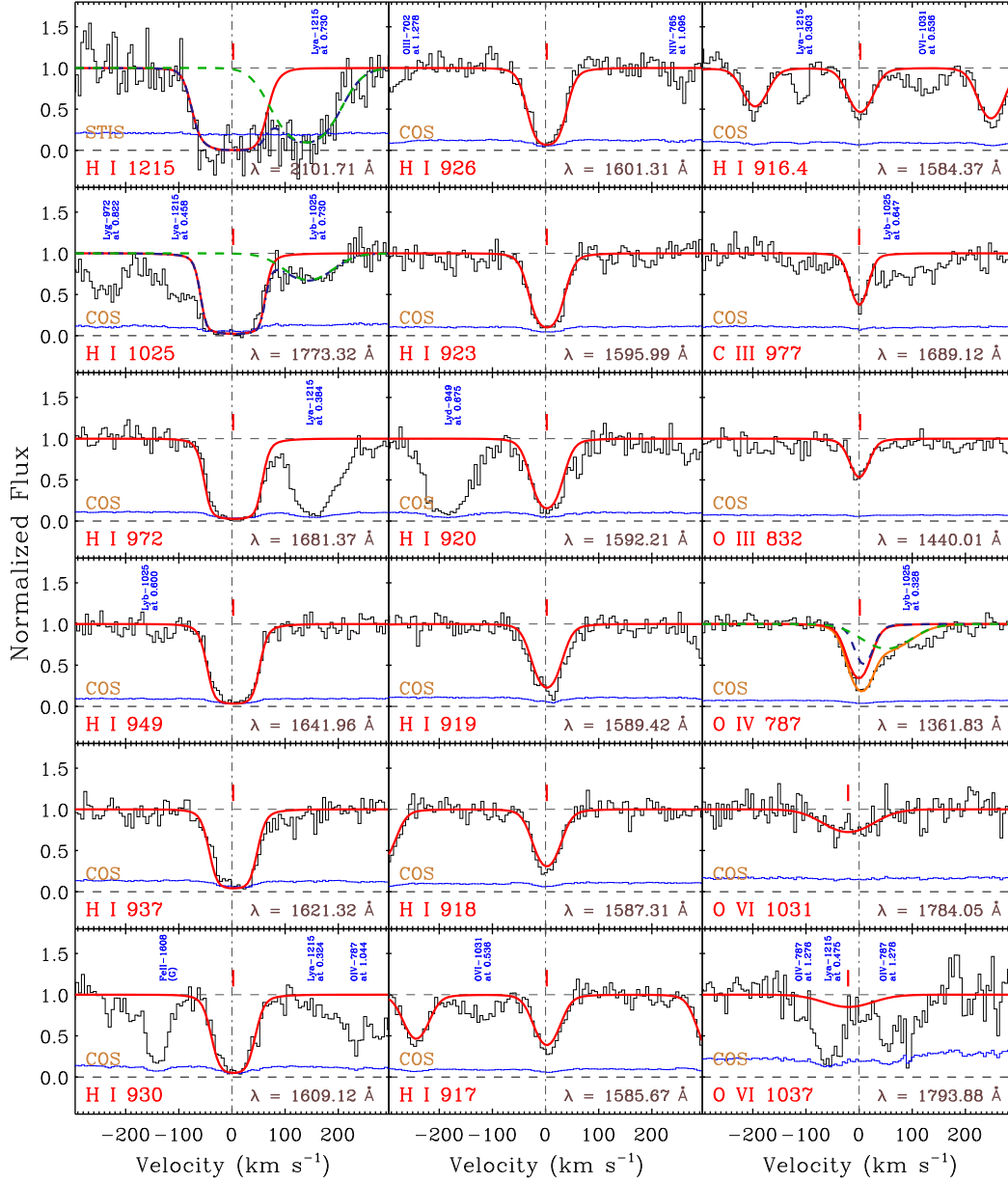


Figure 4A. System plot of the $z_{abs}=0.72885$ absorber, with continuum-normalized flux along the Y-axis and the velocity scale relative to the redshift of the absorber along the X-axis. The $v = 0 \text{ km s}^{-1}$, marked by the *dashed-dotted* vertical line, indicates the absorber redshift. The 1σ uncertainty in flux is indicated by the *blue* curve at the bottom of each panel. The *red* curves are the best-fit Voigt profiles. The observed wavelength of each transition is also indicated in the respective panels. Interloping features unrelated to the absorber are also labeled. The dashed green curves in the H I 1215 Å and H I 1025 Å panels show a fit of the corresponding H I lines at $z \sim 0.730$ and the blue curve shows the composite fit. The O IV 787 Å is severely contaminated by H I 1025 Å at $z \sim 0.327$ and 0.328. The contamination was accounted for in the fit and is displayed as dashed blue and green curve in the panel.

6 THE $Z_{ABS} = 1.09457$ ABSORPTION SYSTEM

6.1 Characterization of the $z_{abs} = 1.09457$ absorber

The system plot for the key transitions in the absorber is shown in Figure 5A (the full version in Appendix Figure B3), and the AOD and Voigt profile fit measurements are listed in Appendix Tables B5 and B6. The combined COS and STIS spectra cover five successive ionization stages of oxygen, viz., O II, O III, O IV, O V and O VI in their multiple lines. Among these, barring O II, all the other ions are detected at $\geq 3\sigma$, with single component line profiles. The non-detection of O II is consistent with the non-detections of C II,

Mg II, and Si II, all of which possess similar ionization potentials. The C IV $\lambda\lambda 1548, 1550$ lines are well detected in the higher *S/N* HIRES data. The single component absorption for C IV at 7 km s^{-1} resolution justifies the single component profile adopted for the metal lines and H I in the *HST* data. The apparent column density profiles and their integrated values for the four O IV lines are all within 0.1 dex of each other suggesting little unresolved saturation in each of them (See Figure 5B and Table B5). A simultaneous profile fit to these four lines offer a robust estimate on the column density and *b*-parameter for O IV. Adopting the *b*-value of C IV also yields good fit to the four O IV lines, with column density that

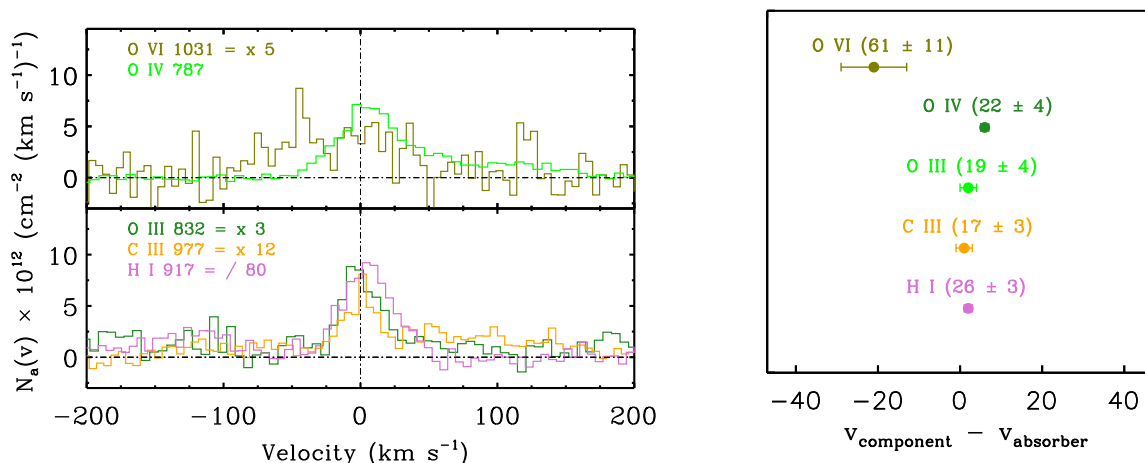


Figure 4B. Apparent column density comparison of different detected species of the absorber at $z_{abs} = 0.72885$. The high ions are plotted on the top panel and the intermediate ions on the bottom panel. The figure on the right shows the velocity centroid of each line derived from profile fitting relative to the redshift of the system. The b -parameter measured for the various ions are indicated within the parentheses.

is within 1σ of the free-fit value. The O v 629 line is strong and saturated. The O v ion has previously been detected in only two other intervening absorbers at $z \lesssim 1$ (Howk et al. 2009, Narayanan et al. 2011). The apparent column density integrated measurement for O v is 0.54 dex lower than the column density obtained from a free fit, suggesting line saturation that is unresolved. Though line profile fitting corrects for saturation to some degree, we found that the column density of O v can be varied by about ~ 0.24 dex by changing the b -parameter over a permissible range yielding satisfactory fits to the O v 629 line feature. The column density we therefore adopt for O v is $\log[N(\text{O v})] = 14.63 \pm 0.24 \text{ cm}^{-2}$. The N III 684 and 685 lines are detected, but both are severely contaminated. A column density upper limit for N III is obtained by integrating the N III 685 profile over the same velocity range as O III. The N IV 765 is a marginal 3σ feature, whereas the N v $\lambda\lambda 1238, 1242$ lines covered by STIS are non-detections.

All other metal ions are non-detections or information on them is severely obscured by line contamination. The region corresponding to Ne VIII 770 line is contaminated by Ly α from an absorber at $z = 0.32773$. The Ne VIII 780 line is a non-detection. The other non-detections include C II, O II, Mg II, Al II, Si II, C II, Al III, Si III, S IV, S V, S VI and Mg X. The non-detections of Ne VIII, S VI and Mg X are an indication of the absence of hot collisionally ionized gas with $T > 10^{5.5}$ K, as these ions are diagnostic of such thermal conditions. The C III 977 line appears strong, and is covered by the G185M NUV grating of COS and the E230M grating of STIS. The STIS spectrum however is at a very low S/N of ~ 3 per 10 km s^{-1} resolution. A single component free fit to the C III 977 COS feature by adopting the b -value of C IV yields $\log [N(\text{C III}), \text{cm}^{-2}] = 14.16 \pm 0.20 \text{ cm}^{-2}$. However, for the saturated line, this solution is not unique. We therefore adopt a conservative lower limit of $\log N(\text{C III}) > 13.6 \text{ cm}^{-2}$ obtained from the AOD method. The detections of C III and O III, along with non-detection of Si III point to non-solar [C/Si] and [O/Si] abundances. The other significant non-detection is of He I 537 and 584 lines, which puts an upper limit of $\log [N(\text{He I}), \text{cm}^{-2}] < 13.0 \text{ cm}^{-2}$.

The STIS and COS observations combined offer coverage of a number of Lyman series lines. Though the Ly α is saturated, the non-detection of higher order Lyman lines yield a measurement of $\log[N(\text{H I}), \text{cm}^{-2}] = 14.68 \pm 0.15$ with $b(\text{H I}) = 25 \pm 3 \text{ km s}^{-1}$

obtained from a simultaneous Voigt profile fit to all the uncontaminated Lyman lines. The profile fit was done assuming a single component, as there is no explicit evidence for additional components in the metal lines or the H I that is kinematically coincident with the metals. We also fit the additional three components seen in Ly α from $+125$ to $+350 \text{ km s}^{-1}$ as shown in Figure 5A. The non-detection of these components in Ly β serves as a good constraint for fitting these lines. No metal lines are detected at this velocity. The first among these offset components could potentially be tracing warm gas as hinted by its broad b -parameter of $\sim 46 \text{ km s}^{-1}$. The absence of metal absorption at these offset velocities limits us from exploring such a possibility further. The well detected oxygen lines all have profiles similar to that of H I indicating that they could all be tracing a kinematically homogeneous medium. The centroid of metal lines and H I obtained from fitting are also within $|\Delta v| \lesssim 15 \text{ km s}^{-1}$ of each other, with the differences primarily coming from the lower S/N STIS spectra compared to HIRES and COS (see Figure 5B). The H I column density is comparable to the O IV column density, pointing at high [O/H] abundance, as the photoionization models later reveal. The b -values of H I and metal ions including their 1σ uncertainty suggest the temperature in the absorber to be in the range $T = (0.3 - 3.6) \times 10^4 \text{ K}$.

6.2 Ionization Models for the $z_{abs} = 1.09457$ absorber

Information on five successive ionization stages of oxygen in this absorber offers robust constraints on the density, independent of metallicity as well as the H I column density. In Figure 5C, the observed column density ratios between the different ionization stages of oxygen are compared with the model predictions. The $N(\text{O III})/N(\text{O IV}) = -0.46 \pm 0.08$, the $N(\text{O IV})/N(\text{O v}) = 0.06 \pm 0.19$, and the $N(\text{O v})/N(\text{O VI}) = 0.6 \pm 0.25$ are valid for densities within the range of $n_{\text{H}} = (0.3 - 1.1) \times 10^{-3} \text{ cm}^{-3}$. It is unrealistic to expect a single uniformly photoionized medium to simultaneously explain five ionization stages of oxygen. Assuming that the kinematically coincident components are also co-spatial, the range may be suggestive of the narrow density-temperature differences that could be present in the absorber at scales unresolved. At the spectral resolutions of the data, such small-scale inhomogeneity will get smoothed-out. The measurements only reveal inte-

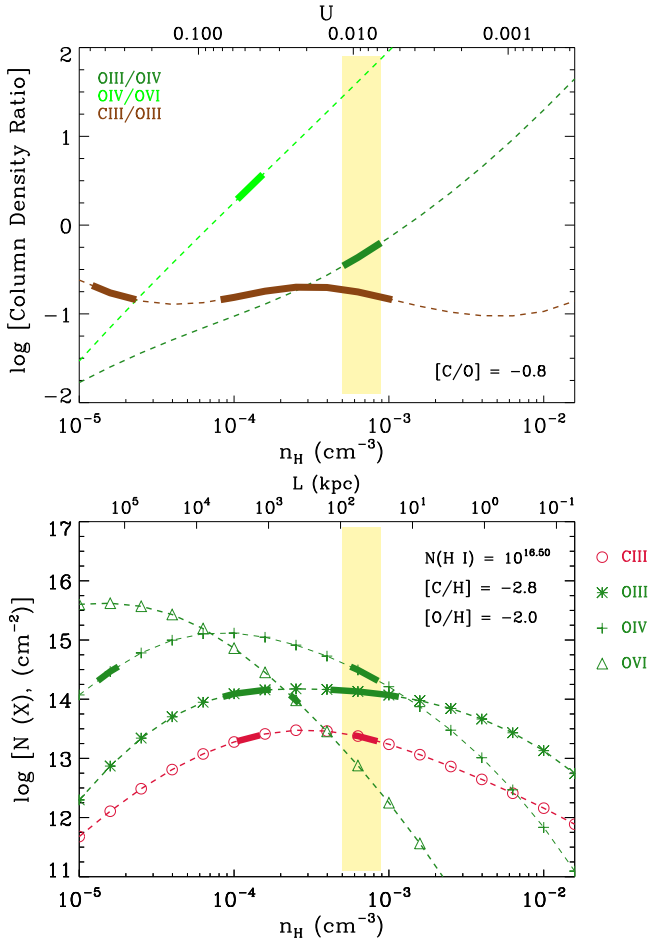


Figure 4C. Photoionization equilibrium models for the $z_{abs} = 0.728850$ absorber. The model predicted ratio between column densities of various ionic species at different densities is shown in the *left* panel, and the column density predictions are in the *right* panel. The *thick* portions of each curve represent the observed column density ratios with its 1σ uncertainty (left-panel) and the measured column density (right-panel). The *yellow* region marks the narrow density range that simultaneously satisfies the column density ratios between the ions of oxygen. The abundances that are required for the models to reproduce the observations are indicated in the panels. The ionization parameter (u) and line of sight thickness for a given density are given by the *top* X-axis of the panels.

grated column densities along the line of sight. Unlike the previous two absorbers, there is no explicit evidence for the O VI to be tracing a separate warm phase.

The oxygen abundance is constrained primarily by $N(\text{O III})$. The observed $N(\text{O III})$ cannot be justified for $[\text{O}/\text{H}] \leq +0.2$ at any density. For $[\text{O}/\text{H}] = +0.2 \pm 0.2$, the PIE models predict column densities of O III, O IV, O V and O VI that agree with their respective observed values within the density range given by the models based on the observed column density ratios. The uncertainty in metallicity is a cumulative of the measurement errors in H I and O III. The narrow density range also predicts the observed C III to C IV and N III to N IV column density ratios. The C IV column density, which is very well measured from the doublet lines in the HIRES spectrum, require $[\text{C}/\text{O}] = -0.2 \pm 0.1$ for an origin from the same phase as the oxygen. For the same reason, the observed $N(\text{N IV})$ require a $[\text{N}/\text{O}] = -0.4 \pm 0.4$. The non-detections of Ne, Mg, Si and S are also consistent with the predic-

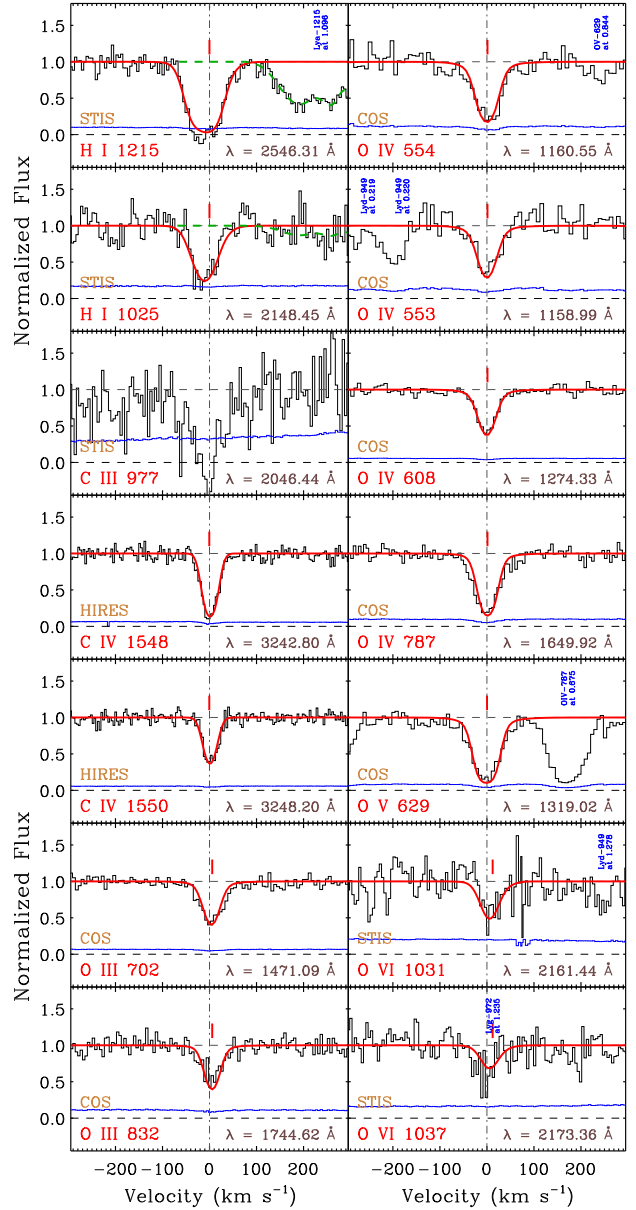


Figure 5A. System plot of the $z_{abs}=1.09457$ absorber, with continuum-normalized flux along the Y-axis and the velocity scale relative to the redshift of the absorber along the X-axis. The $v = 0 \text{ km s}^{-1}$, marked by the *dashed-dotted* vertical line, indicates the absorber redshift. The 1σ uncertainty in flux is indicated by the *blue* curve at the bottom of each panel. The *red* curves are the best-fit Voigt profiles. The observed wavelength of each transition is also indicated in the respective panels. Interloping features unrelated to the absorber are also labeled. Due to the low S/N , a satisfactory Voigt profile model is not obtained for C III 977. The dashed green curves in the H I 1215 Å and H I 1025 Å panels show a three component fit of the corresponding H I lines at $z \sim 1.096$.

tions from the ionization models. For the density range of $n_{\text{H}} = (0.3 - 1.1) \times 10^{-3} \text{ cm}^{-3}$, the PIE models predict a total hydrogen column density in the range of $\log[N(\text{H}), \text{cm}^{-2}] = 18.61 - 17.89$, a gas temperature and pressure of $T = (1.1 - 1.7) \times 10^4 \text{ K}$ and $p/K = (4.8 - 12.3) \text{ cm}^{-3} \text{ K}$, over a path length of $L = (4.7 - 0.2) \text{ kpc}$. The

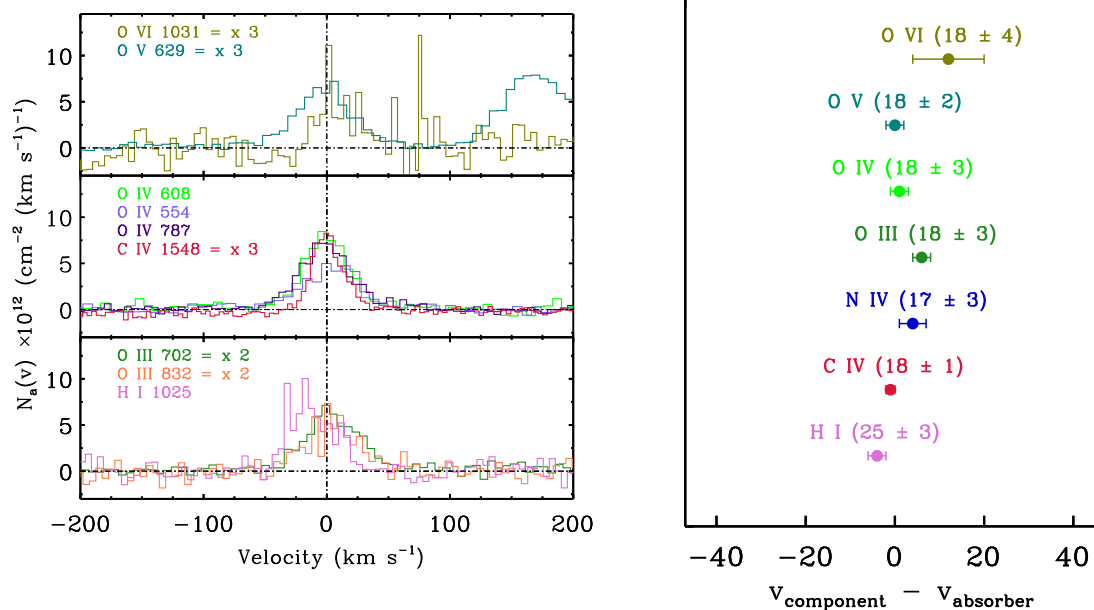


Figure 5B. Apparent column density comparison of different detected species of the absorber at $z_{abs} = 1.09457$. The high ions are plotted on the top panel and the intermediate ions on the bottom panel. The figure on the right shows the velocity centroid of each line derived from profile fitting relative to the redshift of the system. The b -parameter measured for the various ions are indicated within the parentheses.

temperature is within the $(0.3 - 3.6) \times 10^4$ K range predicted by the separate b -values of H I and metal lines.

The non-detection of the He I 584 line can be used to establish an upper limit on the He abundance in the absorber. At the mean density of $n_{\text{H}} = 0.7 \times 10^{-3} \text{ cm}^{-3}$, the neutral fraction of H and He are $f_{\text{H I}} = 3.7 \times 10^{-4}$, and $f_{\text{He I}} = 8.6 \times 10^{-5}$ respectively. Applying these ionization corrections to $N(\text{He I}) < 10^{13.0} \text{ cm}^{-2}$, and $N(\text{H I}) = 10^{14.68} \text{ cm}^{-2}$, we estimate a He abundance of $y_p = N(\text{He})/N(\text{H}) < 0.0892$, and a He mass-fraction of $Y_p = 4y_p/(1 + 4y_p) < 0.26304$. The mass-fraction thus obtained is consistent with the $Y_p = 0.24672 \pm 0.00017$ given by primordial nucleosynthesis models (Pitrou et al. 2018), and CMB anisotropy measurements (Planck Collaboration et al. 2016). Quasar absorption line measurements of gas with near-primordial chemical composition estimate the $[\text{He}/\text{H}]$ mass fraction as $0.25^{+0.033}_{-0.025}$ Cooke & Fumagalli (2018).

7 THE $Z_{ABS} = 1.16592$ ABSORPTION SYSTEM

7.1 Characterization of the $z_{abs} = 1.16592$ absorber

The system plot for the key transitions in the absorber is shown in Figure 6A (the full version is Appendix Figure B4), and the AOD and Voigt profile fit measurements are listed in Appendix Tables B7 and B8. Information on five different ionization stages of oxygen are available for this absorber. The O III, O IV, O V and O VI 1031 are $> 3\sigma$ detections, whereas O II is a non-detection. The O VI 1037 line predicted from a fit to the 1031 line is weak and consistent with its formal non-detection in the STIS spectrum with $S/N \sim 7$ per 0.05 \AA resolution. The O IV ion is detected in four transitions. The O IV 554 line is contaminated by the interstellar N I 1200. The integrated apparent column densities of the other three uncontaminated O IV lines are within 0.1 dex of each other

indicating that unresolved saturation is nearly absent. The O V 629 also has only mild levels of unresolved saturation at the line core as revealed by its 0.07 dex lower integrated apparent column density compared to the profile fit. The non-detections of high ionization state ions such as Ne VIII, and Mg X indicate the absence of warm-hot temperatures ($T > 10^{5.5} \text{ K}$) and high degree of ionization characteristic of collisionally ionized gas.

The O IV lines show asymmetry in the negative velocity portion of their profiles, which is more evident in O V 629 (see $N_d(v)$ comparison in Figure 6B). The excess absorption is also seen at a lesser significance in the C IV $\lambda\lambda 1548, 1550$ lines detected by HIRES. A two component model was therefore adopted to model the metal lines. The mild excess absorption at the negative velocity edge is not distinctly evident in the O VI 1031, 1037, C III 977 and Si III 1206 lines covered by the noisier STIS data. For the O VI a two component model still yields a satisfactory fit, but for C III and Si III a single component was adequate.

The Lyman series absorption lines from Ly α to H I 930 covered by STIS are strong saturated lines. The COS coverage of Lyman transitions continue from H I 918, which are weak and the higher order transitions are non-detections. The S/N of STIS spectra is inadequate to know the exact kinematic substructure in H I. Taking a cue from the metal lines detected by COS, we fit the H I lines simultaneously with a two component model. The contribution from the two components is separately shown in the system plot of Figure 6A. The free-fit positions the two H I components at the same velocity as the components seen in the unsaturated metal lines. The bulk of the absorption is dominated by the central component. The $v \sim -25 \text{ km s}^{-1}$ component has an H I column density that is two orders of magnitude lower.

The metal lines all have similar b -values in each component of the absorption (see right panel Figure 6B). For the negative velocity component, $b(\text{H I}) = 29 \pm 3 \text{ km s}^{-1}$ and $b(\text{O V}) = 22 \pm 7 \text{ km s}^{-1}$ imply metal line broadening that is significantly non-thermal with

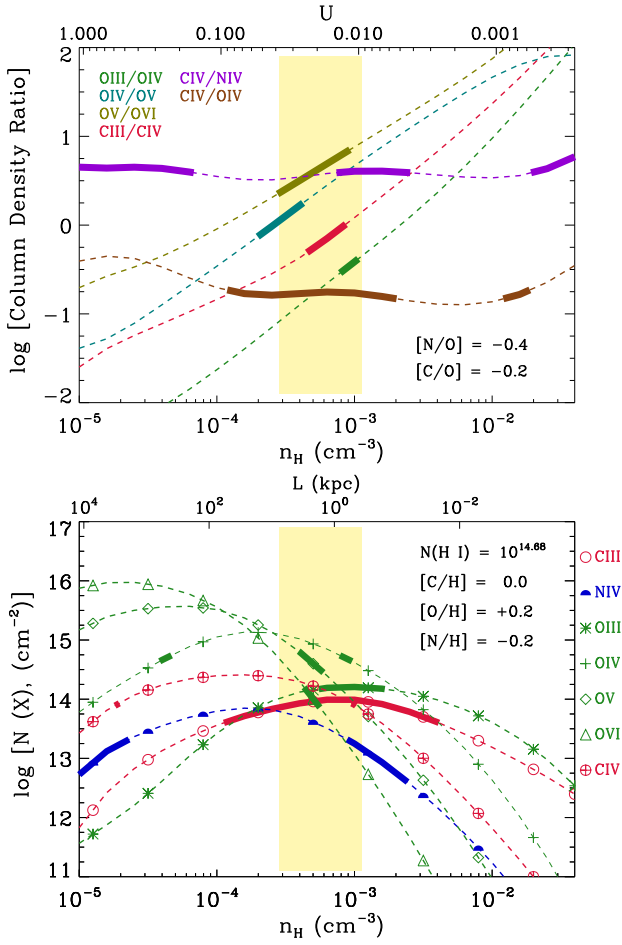


Figure 5C. Photoionization equilibrium model for the $z_{abs} = 1.09457$ absorber. On the *left* panel is the prediction for the ionic column density ratios (*thin* lines) and their observed values (*thick* lines) plotted for various gas number densities. The ratio between successive ions of oxygen limits the plausible gas density to a narrow range indicated by the *yellow* strip. On the *right* panel is the model-predicted column densities of various species (*thin* lines) and their observed values (*thick* lines). The density range allowed by the column density ratios is represented by the *yellow* region. The elemental abundances in the models are varied to reproduce the observed column densities from similar gas phase. The ionization parameter (u) and line of sight thickness for a given density are given by the *top* X-axis of the panels.

a temperature upper limit of $T < 5.2 \times 10^4$ K (considering the 1σ limits). For the stronger positive velocity component, the $b(\text{H I}) = 21 \pm 1 \text{ km s}^{-1}$ and $b(\text{O V}) = 10 \pm 1 \text{ km s}^{-1}$ result in $T = (1.8 - 2.6) \times 10^4$ K.

The COS G130M spectrum covers He I 584 and 537 lines, both of which are detections. The He I 584 line is contaminated from $-70 \lesssim v \lesssim -30 \text{ km s}^{-1}$, and hence these particular pixels were de-weighted while profile fitting. The apparent column density comparison between these two lines shown in *bottom* row of Figure 6B shows unresolved saturation in the line core for the stronger He I 584 line. By adopting the method given by Savage & Sembach (1991), the AOD measured column density of He I will be $\log N_a(\text{He I}) = \log N_a(\text{He I}) 537 + \Delta \log N_a = 14.36 + 0.22 = 14.58$, which is consistent with the $\log N(\text{He I}) = 14.48 \pm 0.17$ obtained from simultaneous Voigt profile fitting of the two lines. The detection of He I constrains the density in the absorber as discussed in the next section 7.2.

7.2 Ionization Models for the $z_{abs} = 1.16592$ absorber

The two components of the absorption are modeled separately. The photoionization curves are shown in Figure 6C. The observed O III to O IV, and O IV to O V column density ratios for the central component are recovered by the PIE models over the density range $n_{\text{H}} = (0.4 - 2.5) \times 10^{-3} \text{ cm}^{-3}$. The O V to O VI ratio require slightly lower densities. Similar to the previous absorber, the range in density can be suggestive of mildly different gas phases that are kinematically adjacent contributing to the absorption. The constraints are however inadequate for modeling such a scenario with multiple phases.

An $[\text{O}/\text{H}] = -2.1 \pm 0.2$ is the minimum oxygen abundance required to produce O III at the density of $n_{\text{H}} = 0.95 \times 10^{-3} \text{ cm}^{-3}$ corresponding to its peak ionization fraction. The uncertainty in metallicity is a cumulative of the measurement errors in H I and O III. The same oxygen abundance also produces the observed O IV, O V and O VI within a density range of $n_{\text{H}} = (0.4 - 2.5) \times 10^{-3} \text{ cm}^{-3}$ as shown in Figure 6C. The observed column density of Si III is also recovered within this density range for $[\text{Si}/\text{H}] = -2.0 \pm 0.25$. The observed C IV however requires $[\text{C}/\text{H}] = -2.4 \pm 0.15$ for the C IV to be originating from the same environment as the oxygen ions. For the density range of $n_{\text{H}} = (0.4 - 2.5) \times 10^{-3} \text{ cm}^{-3}$, the models predict a total hydrogen column density in the range $\log N(\text{H}) = 20.60 - 19.70 \text{ cm}^{-2}$, a gas temperature and pressure of $T = (2.3 - 3.4) \times 10^4$ K and $p/K = (14.7 - 57.5) \text{ cm}^{-3} \text{ K}$, and path length thickness of $L = (296.2 - 6.5) \text{ kpc}$. The temperature given by the model agrees with the $T = (1.8 - 2.6) \times 10^4$ K from the b -values of H I and metal lines.

A more binding constraint on the density can be derived by equating the (He/H) abundance in the absorber to its primordial value. From the photoionization model we find that at $n_{\text{H}} = 0.4 \times 10^{-3} \text{ cm}^{-3}$ ($\log [n_{\text{H}}, \text{cm}^{-3}] = -3.36 \pm 0.25$), the He and H ionization corrections of $f_{\text{He I}} = 8.95 \times 10^{-6}$ and $f_{\text{H I}} = 8.27 \times 10^{-5}$ result in $(\text{He}/\text{H}) = 0.0843$ which is close to the primordial $(\text{He}/\text{H}) = 0.085^{+0.015}_{-0.011}$. The density thus obtained, which is within the range predicted by the photoionization models of the other ions, yield $\log N(\text{H}) = 20.6 \text{ cm}^{-2}$, $T = 3.4 \times 10^4$ K, $p/K \sim 14.7 \text{ cm}^{-3} \text{ K}$, and $L = 296.2 \text{ kpc}$.

The inferred length scale points at the absorption coming from a photoionized phase occupying bulk of the CGM of a massive galaxy (Muzahid 2014, Prochaska et al. 2011). A direct example of galaxies possessing such a widely extended envelope of diffuse gas has come from the pair QSO sightline observations by Muzahid (2014) in which they arrived at a size of $\sim 330 \text{ kpc}$ for the photoionized O VI absorbing halo around a $1.2 L^*$ galaxy. The absorption along either sightlines with a transverse separation of 280 kpc suggested a nearly coherent medium of high ionization gas with a photoionization model predicted line of sight length scale of $\sim 700 \text{ kpc}$. An alternative to such a large-scale CGM origin is for the absorption to be tracing a high column density node in the network of intergalactic filaments and sheets, which typically possess a thickness of several hundred kpc (Zhang et al. 1998). The estimated low metallicity of $\sim 1/100$ -th of solar is consistent with such an origin as well.

The blueward offset component with $\log [N(\text{H I})/\text{cm}^{-2}] = 14.69 \pm 0.16$ requires a higher metallicity of $[\text{X}/\text{H}] = -1.2 \pm 0.4$ for the observed C IV, O IV, O V, and O VI to be produced in the density range of $n_{\text{H}} = (1 - 6.3) \times 10^{-4} \text{ cm}^{-3}$. The models predict a total hydrogen column density in the range $\log N(\text{H}) = 19.42 - 18.50 \text{ cm}^{-2}$, a gas temperature and pressure of $T = (4.1 -$

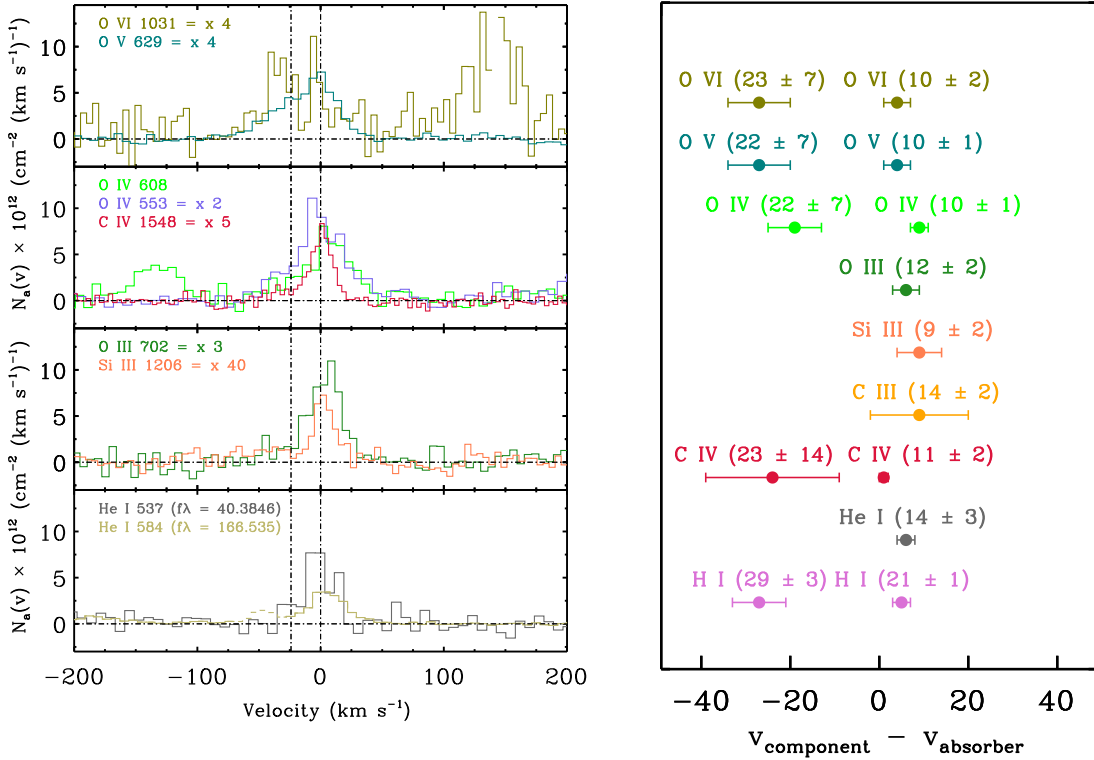


Figure 6B. Apparent column density comparison of different detected species of the absorber at $z_{abs} = 1.16592$. The high ions are plotted on the top panel and the intermediate ions on the bottom panel. The figure on the right shows the velocity centroid of each line derived from profile fitting relative to the redshift of the system. The b -parameter measured for the various ions are indicated within the parentheses.

fer to the $N_a(v)$ comparison in Figure 7B). The intermediate and high ionization metal lines such as O IV, O V, O VI, Ne V, Ne VI, and S VI seen at lower S/N and/or resolution by COS and STIS are also likely to possess narrow b -values if they are tracing the same gas phase. Indeed, the free-fit done for O IV does yield such a result.

The positive velocity side of the O V 629 is contaminated by N III from the $z = 1.09457$ absorber (refer Appendix Figure B3). The contaminated region was excluded during profile fitting. The O V line is saturated at the line core as shown by the 0.5 dex lower column density from the AOD integration compared to the profile fitting. We applied a two component profile for the saturated O V by simultaneously fitting it with the well measured O IV. Even so, the uncertainty in O V column density is likely to be larger than what the profile fitting routine yields. The O VI 1031 line is strong and saturated. A two component model was used to fit the O VI 1031 line by adopting the same b value as O IV for the stronger and saturated component. The effect of line saturation is reflected in the uncertainty in the column density which comes out as ~ 0.8 dex. The 1037 Å line of the O VI doublet is heavily blended with Ly α at $z = 0.945$. The extent of contamination is evident in the system plot (refer Appendix Figure B5) where the expected 1037 Å profile is shown based on the Voigt model for the O VI 1031 Å line.

The b parameters of the various metal lines are similar to each other to within their 1σ uncertainty. The profile fit shows the H I lines to be broader in comparison to metal lines. The $b(\text{H}) \sim 25 \text{ km s}^{-1}$, $b(\text{O}) \sim b(\text{C}) \sim 9 \text{ km s}^{-1}$ imply the temperature to be $T \sim 3.5 \times 10^4 \text{ K}$ in both components.

Additionally, there is detection of Ne V, and Ne VI where the same velocity structure is evident. The COS spectra of these lines

show an asymmetry that is consistent with the presence of a second component, albeit at a lower significance compared to the oxygen ions. This is most likely due to the Ne absorption being intrinsically weaker due to the low cosmic abundance of Ne, and also the decline in spectral resolution towards shorter wavelengths. There is also detection of S VI 933 in the STIS data, but a sub-component structure is not conspicuous at the lower S/N . The important non-detections in the absorber include C II, C III, Si II, Ne VIII, Mg X and He I.

8.2 Ionization Models for the $z_{abs} = 1.27768$ absorber

The absorber is separated from the background quasar by $\Delta v = -6540 \text{ km s}^{-1}$. The difference in redshift between the absorber and the quasar corresponds to a comoving separation of 105 Mpc.⁶ We assess whether the radiation from the background quasar plays any role in the ionization by estimating its intensity at $\sim 910 \text{ Å}$ near the absorber redshift. The intrinsic emission from the quasar is modeled by fitting a power-law continuum to the flux calibrated *HST* spectrum shifted to the quasar rest-frame. Using a flat cosmology model with $\Omega_m = 0.3$ and $H_0 = 70 \text{ km s}^{-1} \text{ Mpc}^{-1}$, we obtain the intrinsic intensity near the Lyman limit to be $j_\nu = (5.2 \times 10^{-26}) e^{\tau_{\text{eff}}} \text{ erg s}^{-1} \text{ cm}^{-2} \text{ Hz}^{-1} \text{ sr}^{-1}$ where τ_{eff} is the effective optical depth between the quasar and the absorber (see Appendix section A for a more detailed calculation). In comparison, the KS19 ionizing background has a 910 Å intensity of

⁶ estimated using Nick Gnedin's cosmology calculator for the flat universe <https://home.fnal.gov/gnedin/cc>

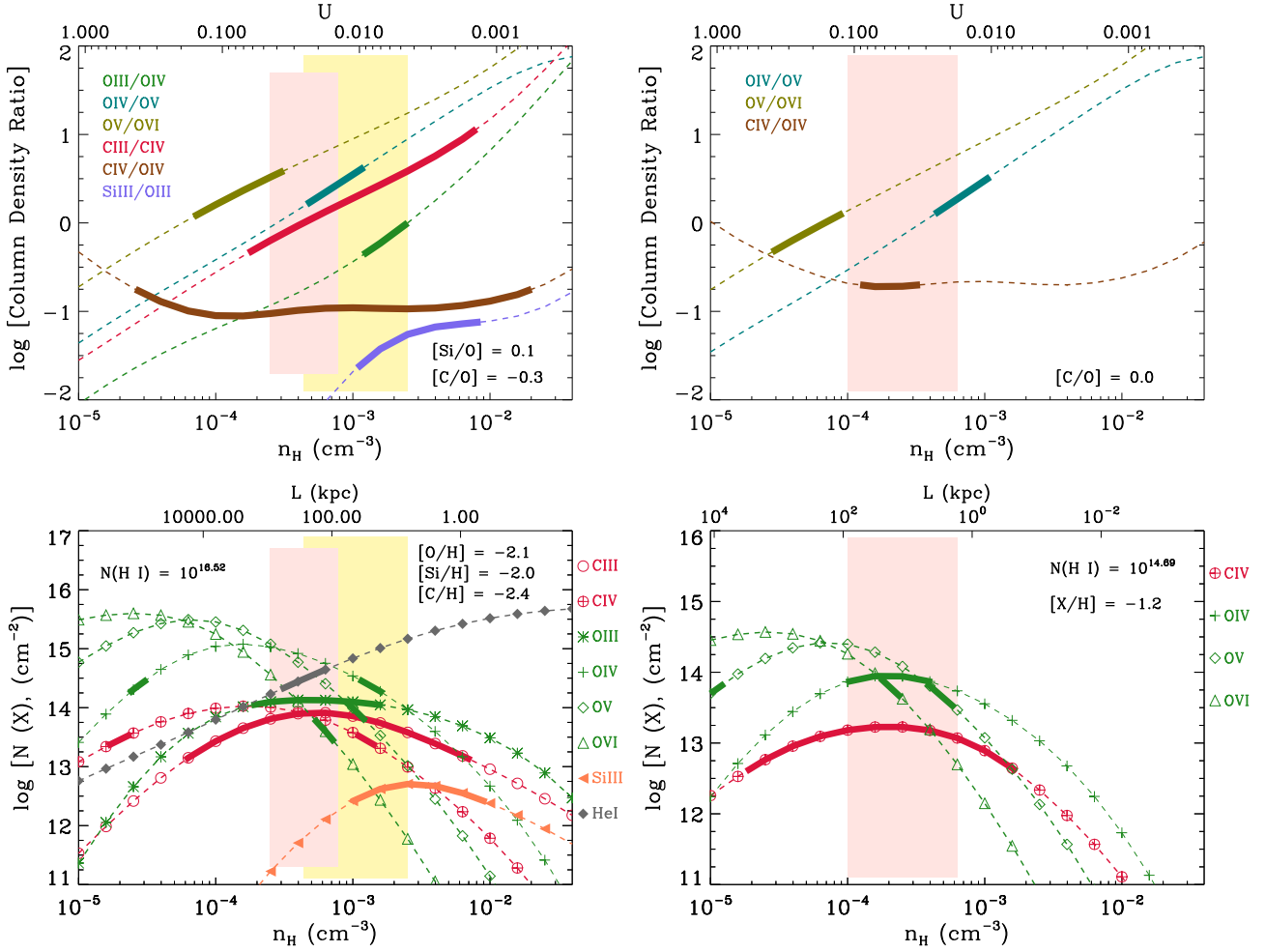


Figure 6C. Photoionization equilibrium model for the two components of $z_{abs} = 1.16592$ absorber towards PG1522+101. The left panels display the PIE model for the red component and the right panels display the PIE model for the blue component. The model of the red component assumes an abundance of -1.8 solar for all elements and the model of the right component assumes an abundance of -1.2 solar for all elements. On the *top* is shown the model predicted (*thin* lines) and the observed (*thick* lines) column density ratios of successive ionization stages of the same element. This ratio, independent of metallicity, constrains the gas density in the absorber to a narrow range indicated by the *yellow* strip. On the *bottom* panels are the model-predicted column densities of various species (*thin* lines), along with their observed values (*thick* lines), plotted against gas density. The density range allowed by the column density ratios is represented by the *yellow* region. The elemental abundances in the models are varied to reproduce the observed column densities (as many as possible) from a single phase. The ionization parameter (u) and line of sight thickness for a given density are given by the *top* X-axis of the panels. On the *left bottom* panel are the range of abundances permitted by the photoionization models for the various elements. The *pink* zone shows the density range for which the primordial He/H can be recovered.

$j_v^{UVB} = 3.7 \times 10^{-22} \text{ erg s}^{-1} \text{ cm}^{-2} \text{ Hz}^{-1} \text{ sr}^{-1}$. The quasar ionizing radiation at the location of the absorber is thus several orders of magnitude weaker than the extragalactic UV background and is therefore unlikely to have regulated the ionization in the absorber in any significant way. We therefore proceed with the KS19 model for the background radiation field.

In the PIE models, the two components of this absorber, separated by $|\Delta v| \sim 40 \text{ km s}^{-1}$, are considered separately. The observed $N(\text{C III})/N(\text{C IV})$, $N(\text{O III})/N(\text{O IV})$, $N(\text{O IV})/N(\text{O V})$, $N(\text{O V})/N(\text{O VI})$ and $N(\text{Ne V})/N(\text{Ne VI})$ are the principal measurements constraining the density. The column density in either component is well determined for all the ions except O V, and O VI which have unresolved saturation and also S VI in which the component structure is less evident because of the absorption being weak and at lower S/N . It can be noticed from the PIE column density ratio curves of Figure 7C that there is no common

density where these five column density ratios exactly overlap, indicating that there exists a multiphase structure. In both components, the O III to O IV, C III to C IV and O IV to O V ratios roughly coincide at a density of $n_{\text{H}} \sim 4.5 \times 10^{-4} \text{ cm}^{-3}$, whereas the Ne V with Ne VI is recovered at $n_{\text{H}} \sim 1.0 \times 10^{-4} \text{ cm}^{-3}$ for solar abundance pattern. The O V to O VI ratio is less constraining because of the large uncertainty in both column densities. Yet, the ratio with its 1σ cumulative error suggests lower densities of $n_{\text{H}} \sim (1 - 10) \times 10^{-5} \text{ cm}^{-3}$ if they are tracing photoionized gas.

The predictions from the PIE models for both components are shown in the *bottom* panels of Figure 7C. Rather than a single density, the column densities of all ions are recovered to within their 1σ uncertainty if we consider the density range of $n_{\text{H}} = (1 - 7) \times 10^{-4} \text{ cm}^{-3}$. It is possible that the absorbing medium may not have uniform ionization throughout. Assuming that the kinematically coincident components are also co-spatial, the line of

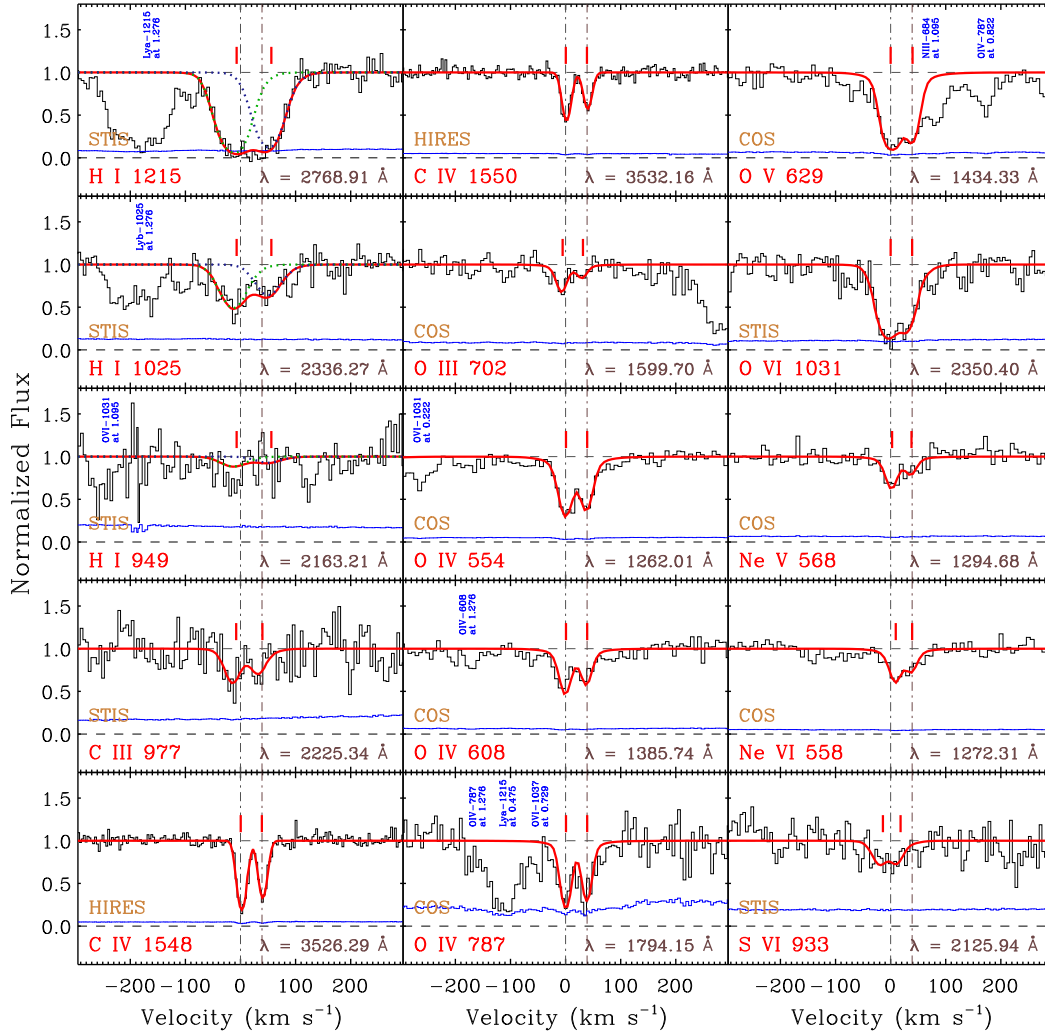


Figure 7A. System plot of the $z_{abs}=1.27768$ absorber, with continuum-normalized flux along the Y-axis and the velocity scale relative to the redshift of the absorber along the X-axis. The $v = 0 \text{ km s}^{-1}$, marked by the *dashed-dotted* vertical line, indicates the absorber redshift. The 1σ uncertainty in flux is indicated by the *blue* curve at the bottom of each panel. The *red* curves are the best-fit Voigt profiles. The observed wavelength of each transition is also indicated in the respective panels. Interloping features unrelated to the absorber are also labeled.

sight is most likely probing a region with differences in ionization parameter at small physical scales that are unresolved, resulting in absorption from ions of different ionization levels roughly coinciding in velocity space.

Such a photoionized medium requires $[O/H]$ and $[Ne/H]$ to be solar and the $[C/H]$ and $[N/H]$ to be sub-solar. Oxygen and Neon enrichment happens through Type II SN explosions involving $\geq 10 M_{\odot}$ stars (Iwamoto et al. 1999, Nomoto et al. 2006), whereas C is returned into the ISM primarily through mass loss during the AGB phase of intermediate mass stars ($\sim 1 - 8 M_{\odot}$) and from Type Ia SNe (Thielemann et al. 1993, Chiappini et al. 2003). The difference in stellar evolution time-scales between massive and intermediate mass stars can give rise to sub-solar $[C/O]$, especially in a medium that is recently enriched. The absorbing gas could be tracing such a medium of high metallicity primarily enriched via contemporaneous Type II SN events.

Interestingly the O VI is barely explained by the above PIE phase over the wide density range considered, indicating the presence of a distinct higher ionization phase. Due to line saturation,

the O VI b -parameter is not independently constrained. In deriving the Voigt profile model, we have assumed $b(O \text{ VI}) \sim b(O \text{ IV}) \sim b(C \text{ IV}) \sim 10 \text{ km s}^{-1}$, which implies a maximum temperature of $T \sim 9.8 \times 10^4 \text{ K}$. If the O VI is tracing a phase separate from O IV and C IV, the temperature of that phase will have to be $T < 4 \times 10^5 \text{ K}$ for the Ne VIII to remain a non-detection. Such an upper bound on the temperature leads to $b(O \text{ VI}) < 20 \text{ km s}^{-1}$ in either component.

To summarize, the absorption line information suggests the presence of multiphase photoionized gas having $n_{\text{H}} = (1 - 7) \times 10^{-4} \text{ cm}^{-3}$ and $[O/H] \sim 0.0 \pm 0.2$, with relative elemental abundances favouring Type II SNe enrichment history. The uncertainty in metallicity is a cumulative of the measurement errors in H I and O III. No firm conclusions can be drawn on the origin of O VI or the properties of gas it traces. The ion could be from a low density ($n_{\text{H}} \lesssim 10^{-5} \text{ cm}^{-3}$) highly photoionized medium, or gas at $T \sim (2 - 4) \times 10^5 \text{ K}$ where collisional ionizations are dominant.

The multiphase nature and the symmetry between the profiles of the two components raises the possibility that the line of sight

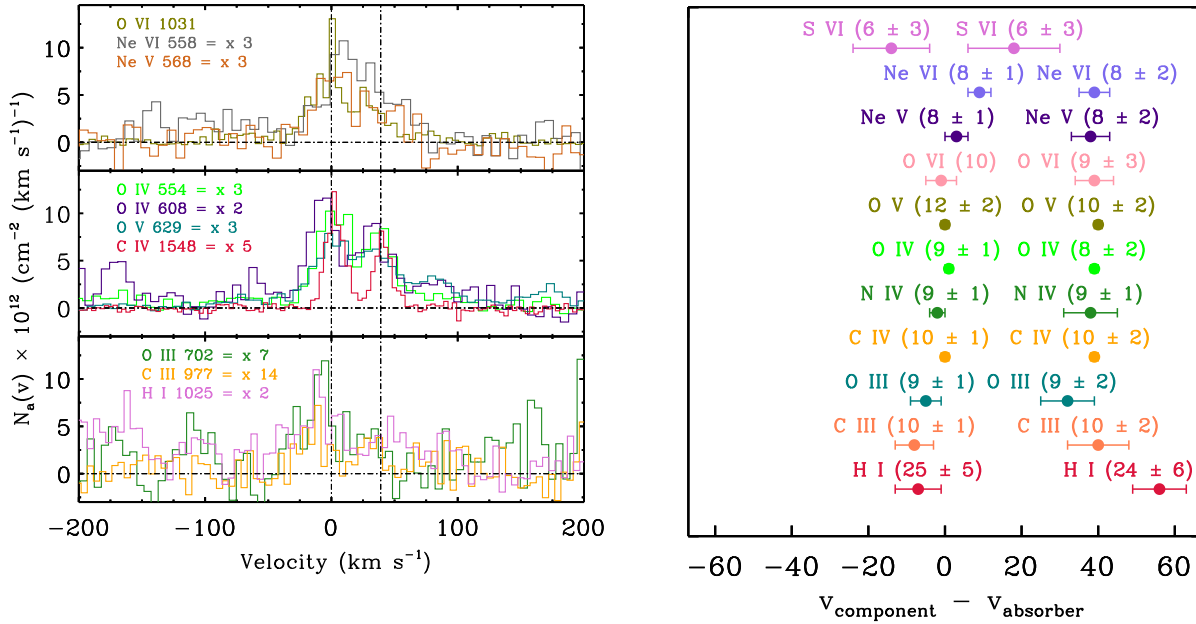


Figure 7B. Apparent column density comparison of different detected species of the absorber at $z_{abs} = 1.27768$. The high ions are plotted on the top panel and the intermediate ions on the bottom panel. The figure on the right shows the velocity centroid of each line derived from profile fitting relative to the redshift of the system. The b -parameter measured for the various ions are indicated within the parentheses. The S VI data is very noisy although it appears to have a 15 km s^{-1} offset. The velocity separation between the two H I components is strongly influenced by the noisy 1025 line.

is passing through a biconical outflow such as superwind or superbubble shell created by multiple supernovae. Such expanding shells can give rise to warm/hot interface layers between the hot ($T \sim 10^6 - 10^7$ K) interior of the bubble and the outer shell of cooler ($T \sim 10^4$ K) interstellar gas swept-up by the supernovae (e.g., Heckman et al. 2000, Savage et al. 2001, Bond et al. 2001), or between hot gas flowing alongside fragments within the shell. The latter scenario was proposed by Heckman et al. (2001) to explain the absorption created by superwind driven material in the starburst dwarf galaxy NGC 1705. The O VI was hypothesized as due to mixing of the hot outflowing material and the cooler fragments of swept-up material resulting in gas that is initially heated to $T > 3 \times 10^5$ K, and subsequently radiatively cooling. The O V, O VI, Ne V and Ne VI in the $z = 1.277$ absorber can be from such cooling interface gas with the lower ions tracing less ionized shells or fragments. At $T \lesssim 10^5$ K, such gas would produce little Ne VIII, consistent with what we observe.

9 DISCUSSION & SUMMARY OF RESULTS

We report on the physical and chemical properties of five multi-phase absorbers from 0.67–1.28 towards the quasar PG 1522+101. The *HST/COS* and STIS spectra of this sightline cover several important redshifted FUV and EUV metal absorption lines in addition to Lyman series lines, all of which serve as diagnostic of the gas phases and abundances. The Keck/HIRES spectra provide additional robust constraints through coverage of C IV and Mg II. The results of photoionization modelling of the systems are summarized in Table 2.

Surveys of O VI absorbers have previously reported an anti-correlation between $\log [N(\text{O VI})/N(\text{H I})]$ and $\log N(\text{H I})$. Savage et al. (2014) explained this trend as due to the O VI in absorber samples spanning a significantly narrow range in column density when compared to H I. A negative correlation is expected

from plotting $1/N(\text{H I})$ against $N(\text{H I})$. However, it is also seen from Figure 8 that the trend remains largely unaffected even when the column density ratio of O VI to H I is plotted. This happens due to the O VI column density remaining nearly a constant in absorbers spanning seven orders of magnitude in H I. Danforth & Shull (2005) reason that this would be the case if O VI and H I are tracing multiple gas phases. The O VI, in their empirical model, comes from a shell-like ionized structure surrounding a low ionization cloud possessing bulk of the H I. The arbitrary size of the neutral cloud would imply that the H I column densities will be different between absorbers while ionizations by energetic photons and electrons would result in a highly ionized boundary layer of similar O VI column densities across absorbers.

As shown in Figure 8, the O VI to H I column density ratio in our sample follows the anti-correlation trend with H I similar to previous studies. The consistently well measured $\log N(\text{O III})$ and $\log N(\text{O IV})$ sample a combined narrow range of 13.2 – 15.0 compared to $\log N(\text{H I}) \sim 14.4 - 16.5$. The O VI in the absorber at $z = 1.27768$ is not well constrained and thus the upper end of the range of $\log N(\text{O VI})$ in our sample is not accurately established. We find that both $N(\text{O III})/N(\text{H I})$ and $N(\text{O IV})/N(\text{H I})$ obey the anti-correlation with $N(\text{H I})$ (Spearman’s rank correlation $\rho = -0.85$, $p = 0.00023$). The non-detections of C II, O II, and Si II indicate that the gas is at intermediate to moderately high ionization levels. The observed anti-correlation trend is therefore more likely due to inefficient mixing of metals with gas. As Schaye et al. (2007) argue, metals displaced from galaxies could be confined to patchy zones within larger H I clouds of the CGM or IGM. Observations sampling such regions will yield a wide range for the column densities of H I depending on the absorber environment and the arbitrary line of sight probing it. From ionization models we derive an overabundance of oxygen relative to carbon in all the absorbers with $[C/O]$ in the range of 0.0 ± 0.4 to -0.8 ± 0.1 relative to solar suggesting that the gas has preferentially been enriched by feedback from Type II SNe (Telfer et al. 2002). Despite this, the metallicity

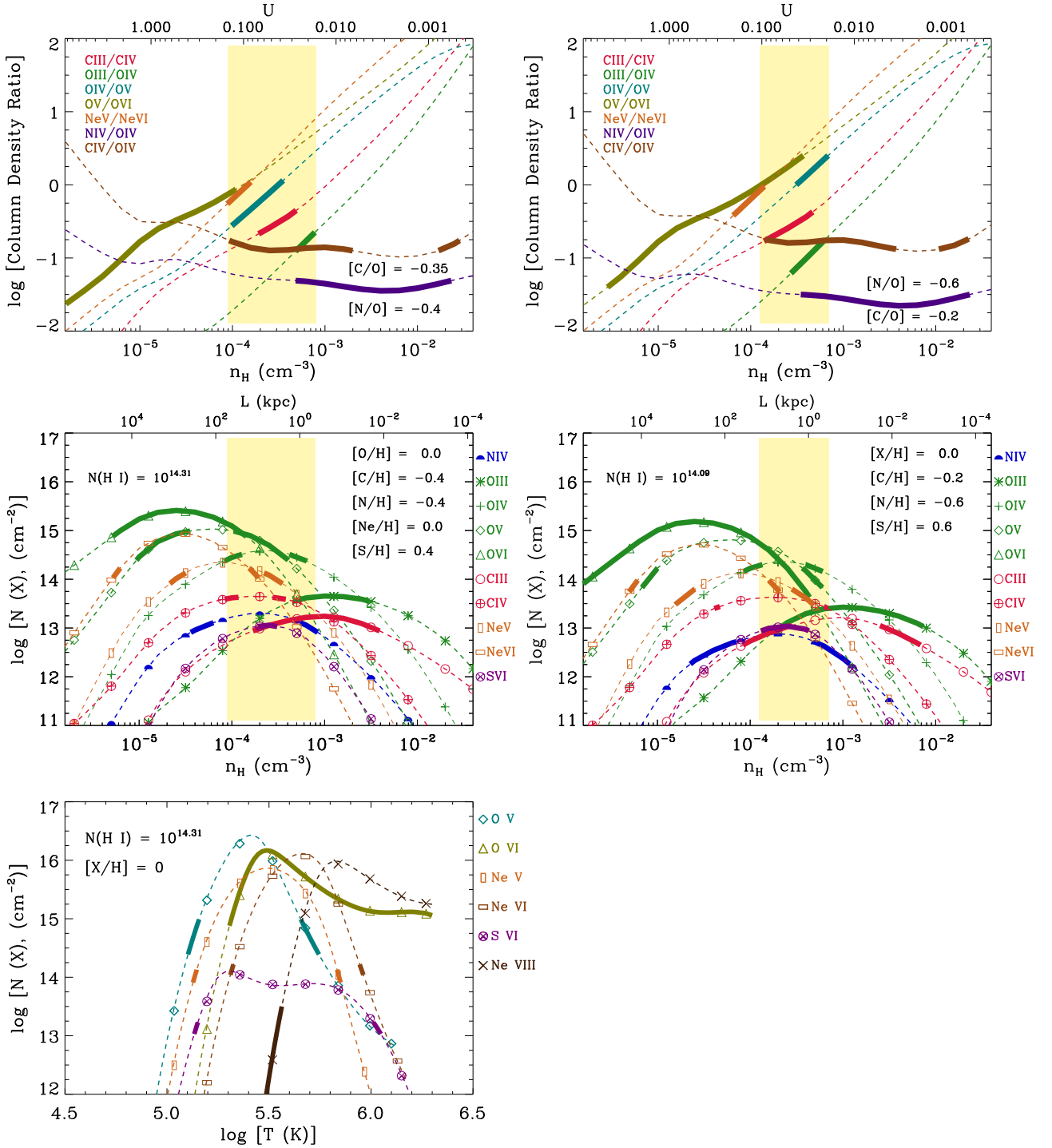


Figure 7C. Photoionization equilibrium model for both components of the $z_{abs} = 1.27768$ absorber towards PG1522+101. The left panels display the PIE model for the blue component and the right panels display the PIE model for the red component. On the *top* is shown the model predicted (*thin* lines) and the observed (*thick* lines) column density ratios of successive ionization stages of the same element. This ratio, independent of metallicity, constrains the gas density in the absorber to a narrow range indicated by the *yellow* strip. On the *bottom* panels are the model-predicted column densities of various species (*thin* lines), along with their observed values (*thick* lines), plotted against gas density. The density range allowed by the column density ratios is represented by the *yellow* region. The elemental abundances in the models are varied to reproduce the observed column densities (as many as possible) from a single phase. The line of sight thickness for a given density is given by the *top* X-axis. On the *left bottom* panel are the range of abundances permitted by the photoionization models for the various elements.

being low for the $z = 0.67556$, $z = 0.72885$ and $z = 1.16592$ absorbers can be due to poor mixing of gas and metals. The lowest metallicity absorbers in our sample are indeed partial Lyman limit systems (see Figure 9). Their low metallicities are consistent with one of conclusions of the COS CGM Compendium (CCC) survey (Wotta et al. (2016)) that more than half the pLLS systems at $z \lesssim 1$ have $[X/H] < -1.0$. Depending on the amount of neutral hydrogen present along a line of sight, inferred metal abundances can turn out as high or low, for a clumpy distribution of metals. This would also mean that metallicities of CGM gas inferred from moderate resolution absorption line studies cannot be used as a definitive marker to distinguish inflows of gas into galaxies, which are necessarily metal poor, from feedback driven metal-rich outflows. Additional information from the kinematics of the absorbing gas, comparison with the ISM metallicities of galaxies in close proximity, and their orientation with respect to the line of sight are needed to draw conclusions on the physical origin of the absorbing gas (e.g., Nielsen et al. 2015, Lan & Mo 2018, Kacprzak et al. 2019).

Based on the observed trend of declining gas column densities with increasing galaxy impact parameters, Prochaska et al. 2011 had proposed that strong Ly α ($W_r > 300$ mÅ) and O VI ($W_r > 70$ mÅ) preferentially trace gas linked to the CGM of $L > 0.1L^*$ galaxies, than the intergalactic clouds of the cosmic web. The H I and metal absorption in intervening systems are also often associated with the multiphase CGM of dwarf galaxies, though the halo covering fractions of gas of various ionization are found to be lower in dwarfs compared to more massive systems. Johnson et al. (2015) estimated that as much as 20% of the O VI absorption at low redshift ($z \sim 0.2$) can potentially be from the CGM of star-forming field dwarf galaxies ($10^{7.7} < (M^*/M_\odot) < 10^{9.2}$). Similarly, the COS-Dwarfs study found that $\sim 60\%$ of C IV absorbers with $W_r > 0.1$ Å are statistically consistent with tracing the CGM of dwarfs ($M^* < 10^{10} M_\odot$, Bordoloi et al. 2014). Such photoionized CGM gas with H I column densities in the sub-Lyman limit ranges ($15.0 < \log [N/\text{cm}^{-2}] < 18.0$) possess a wide range of metallicities from near-pristine to super-solar, due to the diverse processes that are at work at the interface regions of galaxies with the IGM (Werk et al. 2014, Keeney et al. 2017, Lehner et al. 2019, Wotta et al. 2019). The absorbers in our sample have metal and H I equivalent widths and column densities that support close association ($\rho < R_{vir}$) with galaxies than the IGM. Among them, the metal-poor absorbers ($z = 0.67556, 0.72885, 1.16592$) could potentially be tracing clouds of large H I column resulting in diluted inferred metal concentrations along the line of sight. The farthest absorber ($z = 1.27768$) has strong and saturated O VI with $\log N(\text{O VI}) \gtrsim 14.6$, and strong O V as well. Such strong O VI absorbers are closely associated with the extended environments of star forming galaxies of wide mass ranges (Chen & Mulchaey 2009, Wakker & Savage 2009, Tumlinson et al. 2011, Johnson et al. 2015, Bielby et al. 2019, Rudie et al. 2019).

Straightforward evidence for a warm thermal phase is only present in two out of five absorbers in our sample. The first is the $z = 0.67556$ absorber where the O IV and O VI are displaced in velocity from the C III, O III, and H I with the simplest explanation for O VI in this case being collisional ionization at $T \sim 2.5 \times 10^5$ K, at which its ionization fraction peaks. The other is the $z = 0.72885$ absorber where the broader line width of O VI compared to O IV, O III, and H I clearly indicates a higher phase with a $T < 5 \times 10^6$ K associated with a very broad BLA that is undetected. In rest of the absorbers, photoionization by the UV background is a feasible mechanism for the production of O VI and lower ionization metals. Here we note that Zahedy et al. (2019) had found simi-

lar differences in centroid velocities and line widths between O VI and low ions in some of the absorbers identified with the halos of Luminous Red Galaxies (LRGs). Their estimates show that these massive ellipticals ($M_* > 10^{11} M_\odot$) retain CGM mass comparable to that of star-forming massive galaxies. The density prediction from PIE models based on intermediate and high ions as constraints comes out in the range of $n_{\text{H}} \sim (1 - 25) \times 10^{-4} \text{ cm}^{-3}$. The range indicates that the line of sight is probing a multiphase medium, though the exact density-temperature structure is blurred at the resolution of COS. Roca-Fàbrega et al. (2019) show that the ionization of the CGM (and the origin of O VI) is redshift dependant, with photoionization playing a dominant role in the epochs between $0.5 \lesssim z \lesssim 2$ due to the enhanced intensity of the extragalactic UV background following the peak in cosmic AGN activity and star-formation rates. On the other hand, collisional ionization is predominant at the very high ($z \gtrsim 2$) and very low ($z < 0.5$) redshift epochs. Their simulations further show that photoionization tends to dominate the production of O VI in low mass halos (halo virial mass of $M_h \lesssim 10^{10} M_\odot$), and even the outskirts of high-mass galaxies. Thus, it is possible for the photoionized absorbers in our sample to have a circumgalactic origin.

Finally, we comment on the non-detection of Ne VIII in all five absorbers presented here. The presence of Ne VIII in O VI absorbers have been decisive in revealing the presence of gas with $T \sim (0.5 - 1.5) \times 10^6$ K associated with the IGM and the gaseous halos of luminous galaxies (Savage et al. 2005, Savage et al. 2011, Narayanan et al. 2011, Tripp et al. 2011, Meiring et al. 2013, Husain et al. 2015, Qu & Bregman 2016, Pachat et al. 2017, Bordoloi et al. 2017, Rosenwasser et al. 2018, Burchett et al. 2019). Based on a small sample of Ne VIII detections in O VI absorbers, Narayanan et al. (2009) had predicted the redshift number density of Ne VIII systems to be $\sim 1/7 \times dN(\text{O VI})/dz \sim 2.1$ at $z < 0.5$. Through agnostic stacking⁷ of absorption lines along 26 high S/N COS spectra, Frank et al. (2018) arrive at a similar $dN/dz \sim 1.38 (+0.97, -0.82)$ for the interval $0.47 \lesssim z \lesssim 1.34$. On the other hand, Burchett et al. (2019), from a search for Ne VIII in the CGM of 29 galaxies over a similar redshift path, found 9 Ne VIII detections (with all of them also having O VI), arriving at a higher value $dN/dz \sim 5$.

The absorbers in the PG 1522 + 101 sightline presented here cover a redshift path length of $\Delta z = 0.6021^8$. If we adopt the $dN/dz \sim 5$ from Burchett et al. (2019), we expect three Ne VIII detections with $\log [N(\text{Ne VIII})/\text{cm}^{-2}] > 13.0$ along this sightline. On the other hand, the $dN/dz = 1.38$ from Frank et al. (2018) predict no Ne VIII detection, consistent with what we find for the pathlength probed. The column density upper limit of $\log N \lesssim 13.7$ from the non-detection of Ne VIII in the five absorbers presented here implies $T < 10^6$ K, since for temperatures larger than that, we expect $N(\text{Ne VIII}) > N(\text{O VI})$, for solar $[\text{Ne}/\text{O}]$. The absence of Ne VIII could mean that the line of sight towards the PG 1522 + 101 may not be passing through the hot components of the WHIM or the diffuse hot coronal halos of galaxies at the absorber redshifts, though some of these could still be probing the warm ($T \sim 10^5$ K) and the photoionized phases of the CGM and IGM.

A summary of the key results are as follows :

⁷ Presuming every absorption feature to be a Ne VIII 770 Å line, stacking them in the rest frame of the absorber, and searching for Ne VIII 780 Å feature in the stacked spectrum.

⁸ Δz is taken as the difference between the lowest and highest redshift absorber in our sample, i.e., $\delta_z = 1.2776 - 0.6755$

(i) We present the absorption line properties and ionization analysis of five O VI absorbers in the combined *HST*/COS, *HST*/STIS, and Keck/HIRES spectra of PG 1522 + 101. A range of metal lines including successive ionizations of oxygen (O II to O VI), C II, Mg II, Si II, C III, Si III, C IV, Si IV, Ne V, Ne VI, Ne VIII, Mg X etc are covered. Three of the absorbers also cover the redshifted EUV lines of He I 584.334, 537.029 Å, in one of which it is a $> 3\sigma$ detection.

(ii) A prominent high density ($n_{\text{H}} \gtrsim 10^{-3} \text{ cm}^{-3}$), low ionization phase is absent in all the five absorbers as revealed by the non-detections of C II, O II, N II, Mg II and Si II. In four out of the five absorbers, the column densities of oxygen ions follow a trend of $N(\text{O IV}) > N(\text{O III}) > N(\text{O VI})$.

(iii) The metal ions and H I show simple kinematic structures of only one or two sub-components. The presence of a collisionally ionized warm ($T \sim 10^5 \text{ K}$) phase can be deduced directly from the data in the $z = 0.675$ and $z = 0.728$ absorbers in which the O VI is broader and has a significant velocity offset with O III and H I. In the $z = 1.095$ absorber, all observed ions, including O VI, are consistent with photoionization in a medium with a narrow range of densities. In the remaining two absorbers, the ionization origin of O VI is ambiguous.

(iv) Photoionization equilibrium models require densities spread over the range $n_{\text{H}} \sim 10^{-4} - 10^{-3} \text{ cm}^{-3}$ to explain the observed C III, O III, C IV, and O IV column densities suggesting that the absorbing medium does not have uniform ionization throughout.

(v) The observed column densities of O III, O IV, and O VI in all the absorbers are in the relatively narrow ranges of $\log[N/\text{cm}^{-2}] = [13.2, 14.4]$, $[13.9, 15.0]$, and $[13.9, 15.6]$ respectively, whereas the H I column density spans a much wider range of $[14.1 - 16.5]$, resulting in [O/H] values as varied as 1/100-th of solar to super-solar. Ionization models also predict an overabundance of oxygen relative to carbon in all the absorbers with [C/O] in the range of 0.0 ± 0.4 to -0.8 ± 0.1 suggesting that the gas has preferentially been enriched by feedback from Type II SNe. The $z = 0.67556$, $z = 0.72885$ and $z = 1.16592$ absorbers with the lowest [O/H] also have the highest H I column densities, indicating that the inferred low metallicities could be due to poor mixing of gas and metals on small scales.

(vi) The He I 537, 584 Å lines are detected in the $z = 1.16592$ absorber with $N(\text{He I}) = 14.47 \pm 0.16$. Intergalactic He I lines have been detected in only two other instances (Reimers & Vogel 1993, Cooke & Fumagalli 2018). This absorber is the lowest redshift He I detection known till date. The observed He I to H I column density ratio along with the primordial (He/H) abundance places a strong constraint on the gas density in this absorber. This absorber is found to be tracing metal poor gas with [O/H] = -1.9 ± 0.2 . The He I lines are undetected in the $z = 1.09457$ and $z = 1.27768$ absorbers, for which the suggested upper limits on He-mass fraction are consistent with the primordial nucleosynthesis value.

(vii) The Ne VIII and Mg X ions are non-detections, pointing to the absence of hot gas with $T > 10^{5.5} \text{ K}$. The absence of Ne VIII could mean that the line of sight towards the PG 1522 + 101 may not be passing through the hot components of the WHIM or the diffuse hot coronal halos of galaxies at the absorber redshifts, though some of these could still be probing the warm ($T \sim 10^5 \text{ K}$) and the photoionized phases of the CGM and IGM.

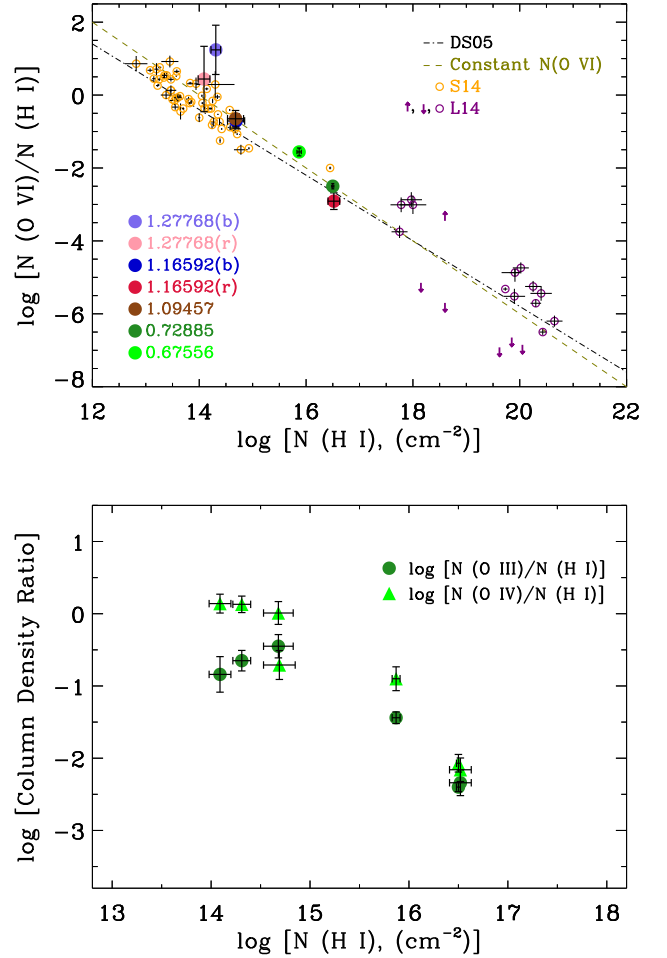


Figure 8. The *top* panel shows the observed O VI to H I column density ratio against the H I column density. Data points are taken from Savage et al. 2014 and Lehner et al. 2014. The *dash-dot* line is a power law fit to the data, identical to the one given by Danforth & Shull 2005 formalizing the trend seen between $\log [N(\text{O VI})/N(\text{H I})]$ and $\log [N(\text{H I})]$. Measurements on the five absorbers in our sample closely follows this trend. The *dash* line represents the negative correlation from plotting $1/N(\text{H I})$ against $N(\text{H I})$ for a constant $N(\text{O VI}) = 10^{14}$. The DS05 curve and the data points closely follow this trend as O VI is roughly constant in 7 orders of magnitude of $N(\text{H I})$. The *bottom* panel shows the observed anti-correlation between O III to H I column density ratio and $N(\text{H I})$, and O IV to H I column density ratio against the H I column density ($\rho = -0.85$, $p = 0.0023$). The anti-correlation comes about as a result of Oxygen ionization column density in samples of absorbers spanning a much narrower range compared to H I, which can be interpreted as evidence of poor mixing of metals with ambient gas assuming that the kinematically coincident components are also co-spatial.

ACKNOWLEDGEMENTS

We thank the referee, Dr. Sean Johnson for the valuable feedback and suggestions on the manuscript. SS thanks Jayadev Pradeep for discussions on line measurements at the initial stages of this work. SS and AN thank Raghunathan Srianand for several useful inputs on modeling in the early stages of this work. We thank the people responsible for the tools and packages used in this work (Cloudy, Makee, VPFIT, Astropy). We thank the people behind the creation and maintenance of COS, STIS, and HIRES instruments and their

z_{abs}	$\log N(\text{HI})$ (cm^{-2})	n_{H} (cm^{-3})	$\log N_{\text{H}}$ (cm^{-2})	p/k (K cm^{-3})	T (K)	L (kpc)	Origin of O VI	[O/H]	[C/O]
0.67556	15.87 ± 0.04	$(1.6 - 7.1) \times 10^{-4}$	19.93 – 19.20	4.6 – 15.9	$(2.9 - 2.2) \times 10^4$	172.4 – 7.2	CI	-0.9 ± 0.1	-0.5 ± 0.2
0.72885	16.50 ± 0.02	$(5.0 - 8.9) \times 10^{-4}$	20.15 – 19.86	14.3 – 22.3	$(2.8 - 2.5) \times 10^4$	92.2 – 26.1	CI	-2.0 ± 0.1	-0.8 ± 0.1
1.09457	14.68 ± 0.15	$(2.8 - 11.2) \times 10^{-4}$	18.61 – 17.89	4.8 – 12.3	$(1.7 - 1.1) \times 10^4$	4.7 – 0.2	PI	$+0.2 \pm 0.2$	-0.2 ± 0.1
1.16592(-25)	14.69 ± 0.16	$(1 - 6.3) \times 10^{-4}$	19.42 – 18.50	4.1 – 18.2	$(4.1 - 2.9) \times 10^4$	85.8 – 1.6	PI/CI	-1.2 ± 0.2	0.0 ± 0.4
1.16592(1)	16.52 ± 0.11	$(4.4 - 25.1) \times 10^{-4}$	20.60 – 19.70	14.7 – 57.5	$(3.4 - 2.3) \times 10^4$	296.2 – 6.5	PI	-2.1 ± 0.2	-0.3 ± 0.2
1.27768(0)	14.31 ± 0.09	$1.4 - 7.9 \times 10^{-4}$	18.73 – 17.81	3.3 – 10.8	$(2.3 - 1.4) \times 10^4$	12.3 – 0.3	PI/CI	0.0 ± 0.2	-0.4 ± 0.2
1.27768(39)	14.09 ± 0.11	$1.3 - 7.1 \times 10^{-4}$	18.56 – 17.63	3.0 – 9.5	$(2.4 - 1.3) \times 10^4$	9.4 – 0.5	PI/CI	0.0 ± 0.3	-0.2 ± 0.3

Table 2. Summary of phase solution results from Photoionization Modelling of absorbers. The first column indicates the absorber redshift (z_{abs}). Successive columns correspond to the logarithm of neutral hydrogen column density ($\log N(\text{H I})$) measured from Lyman series lines, the logarithm of total hydrogen column density ($\log N_{\text{H}}$), the solution phase gas density (n_{H}), gas pressure (p) normalized by k , photoionization equilibrium temperature (T), the path length (L) of the absorber along the sightline indicating the size of the absorber in kpc, and the possible origin scenario that could give rise to the observed O VI. The final two columns indicate the obtained relative abundance of Carbon to Oxygen, [C/O] and the abundance of Oxygen [O/H] in each absorber respectively. We note that the values quoted are extracted from the photoionization models of each individual absorber. The [O/H] has an additional systematic uncertainty of ~ 0.5 dex coming from the generic EBR model (Howk et al. 2009).

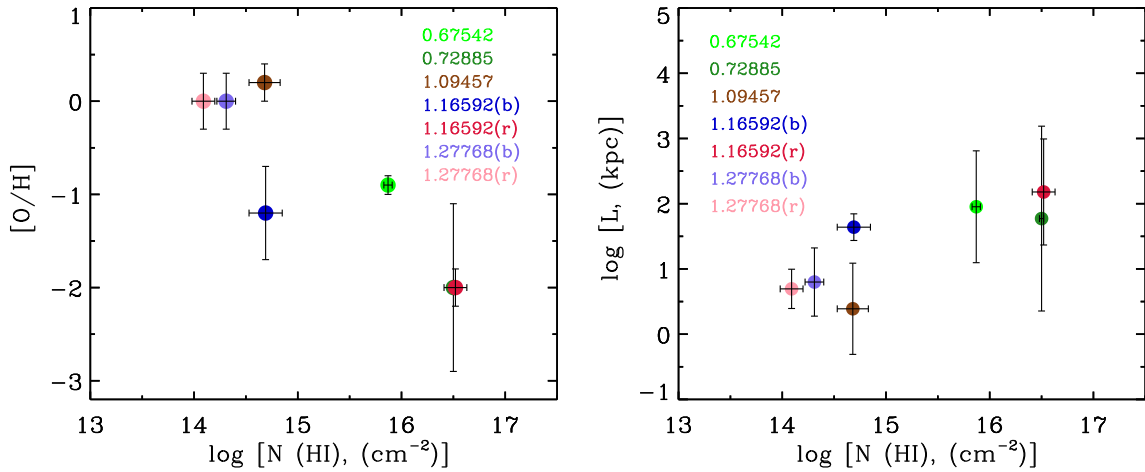


Figure 9. The panel on the *left* shows the trend between the inferred abundance of oxygen from PIE models and the H I column density for each absorber in our sample. Metals confining to small physical scales results in low values of inferred metallicity in higher H I column density systems, which also leads to large values for inferred path length sizes for the absorbers from the PIE models (*right* panel). However we note that components that are close-by in velocity need not be co-spatial.

respective public archives. Support for this work was provided by SERB through grant number EMR/2017/002531 from the Department of Science & Technology, Government of India. Based on observations made with the NASA/ESA Hubble Space Telescope, support for which was given by NASA through grant HST GO-14655 from the Space Telescope Science Institute. STScI is operated by the Association of Universities for Research in Astronomy, Inc. under NASA contract NAS 5-26555. This research has made use of the Keck Observatory Archive (KOA), which is operated by the W. M. Keck Observatory and the NASA Exoplanet Science Institute (NExSci), under contract with the National Aeronautics and Space Administration.

DATA AVAILABILITY

The data underlying this article are from Archival HST and Keck databases and are publicly available from the Mikulski Archive for Space Telescopes (MAST, <https://archive.stsci.edu/hst/>) and Keck Observatory Archive (KOA, <https://koa.ipac.caltech.edu/cgi-bin/KOA/nph-KOAllogin>) respectively.

REFERENCES

- Anderson M. E., Bregman J. N., 2010, *The Astrophysical Journal*, 714, 320
 Anderson M. E., Bregman J. N., Dai X., 2013, *The Astrophysical Journal*, 762, 106
 Asplund M., Grevesse N., Sauval A. J., Scott P., 2009, *Annual Review of Astronomy and Astrophysics*, 47, 481

- Barai P., et al., 2013, *Monthly Notices of the Royal Astronomical Society*, 430, 3213
- Bielby R. M., et al., 2019, *Monthly Notices of the Royal Astronomical Society*, 486, 21
- Boehringer H., Hartquist T. W., 1987, *Monthly Notices of the Royal Astronomical Society*, 228, 915
- Bond N. A., Churchill C. W., Charlton J. C., Vogt S. S., 2001, *The Astrophysical Journal*, 557, 761
- Bordoloi R., et al., 2014, *The Astrophysical Journal*, 796, 136
- Bordoloi R., Wagner A. Y., Heckman T. M., Norman C. A., 2017, *The Astrophysical Journal*, 848, 122
- Burchett J. N., et al., 2019, *The Astrophysical Journal Letters*, 877, L20
- Butsky I. S., Burchett J. N., Nagai D., Tremmel M., Quinn T. R., Werk J. K., 2019, *Monthly Notices of the Royal Astronomical Society*, 490, 4292
- Carswell R. F., Webb J. K., 2014, Astrophysics Source Code Library, p. ascl:1408.015
- Chen H.-W., Mulchaey J. S., 2009, *The Astrophysical Journal*, 701, 1219
- Chiappini C., Romano D., Matteucci F., 2003, *Monthly Notices of the Royal Astronomical Society*, 339, 63
- Churchill C. W., Vander Vliet J. R., Trujillo-Gomez S., Kacprzak G. G., Klypin A., 2015, *The Astrophysical Journal*, 802, 10
- Conselice C. J., Gallagher III J. S., Wyse R. F. G., 2001, *The Astronomical Journal*, 122, 2281
- Cooke R., Fumagalli M., 2018, arXiv:1810.06561 [astro-ph]
- Crighton N. H. M., Hennawi J. F., Prochaska J. X., 2013, *The Astrophysical Journal Letters*, 776, L18
- Croom S. M., et al., 2009, *Monthly Notices of the Royal Astronomical Society*, 399, 1755
- Danforth C. W., Shull J. M., 2005, *The Astrophysical Journal*, 624, 555
- Ehlert S., Werner N., Simionescu A., Allen S. W., Kenney J. D. P., Million E. T., Finoguenov A., 2013, *Monthly Notices of the Royal Astronomical Society*, 430, 2401
- Emerick A., Bryan G., Putman M. E., 2015, *Monthly Notices of the Royal Astronomical Society*, 453, 4051
- Ferland G. J., et al., 2017, *Revista Mexicana de Astronomia y Astrofisica*, 53, 385
- Fox A. J., et al., 2013, *ApJ*, 778, 187
- Fox A. J., et al., 2014, *The Astrophysical Journal*, 787, 147
- Frank S., Pieri M. M., Mathur S., Danforth C. W., Shull J. M., 2018, *Monthly Notices of the Royal Astronomical Society*, 476, 1356
- Gnat O., Sternberg A., 2007, *The Astrophysical Journal Supplement Series*, 168, 213
- Haardt F., Madau P., 2001, p. 64
- Hafen Z., et al., 2019, *Monthly Notices of the Royal Astronomical Society*, 488, 1248
- Heckman T. M., Lehnert M. D., Strickland D. K., Armus L., 2000, *The Astrophysical Journal Supplement Series*, 129, 493
- Heckman T. M., Sembach K. R., Meurer G. R., Strickland D. K., Martin C. L., Calzetti D., Leitherer C., 2001, *The Astrophysical Journal*, 554, 1021
- Hewett P. C., Wild V., 2010, *Monthly Notices of the Royal Astronomical Society*, 405, 2302
- Howk J. C., Ribaldo J. S., Lehner N., Prochaska J. X., Chen H.-W., 2009, *Monthly Notices of the Royal Astronomical Society*, 396, 1875
- Hummels C. B., Bryan G. L., Smith B. D., Turk M. J., 2013, *Monthly Notices of the Royal Astronomical Society*, 430, 1548
- Hummels C. B., et al., 2019, *The Astrophysical Journal*, 882, 156
- Hussain T., Muzahid S., Narayanan A., Srianand R., Wakker B. P., Charlton J. C., Pathak A., 2015, *Monthly Notices of the Royal Astronomical Society*, 446, 2444
- Iwamoto K., Brachwitz F., Nomoto K., Kishimoto N., Umeda H., Hix W. R., Thielemann F.-K., 1999, *The Astrophysical Journal Supplement Series*, 125, 439
- Johnson S. D., Chen H.-W., Mulchaey J. S., 2015, *Monthly Notices of the Royal Astronomical Society*, 449, 3263
- Kacprzak G. G., Pionton S. K., Nielsen N. M., Churchill C. W., Muzahid S., Charlton J. C., 2019, *The Astrophysical Journal*, 886, 91
- Keeney B. A., et al., 2017, *The Astrophysical Journal Supplement Series*, 230, 6
- Kereš D., Katz N., Weinberg D. H., DavĀr R., 2005, *Monthly Notices of the Royal Astronomical Society*, 363, 2
- Khaire V., Srianand R., 2015, *The Astrophysical Journal*, 805, 33
- Khaire V., Srianand R., 2019, *Monthly Notices of the Royal Astronomical Society*, 484, 4174
- Lan T.-W., Mo H., 2018, *The Astrophysical Journal*, 866, 36
- Lehner N., et al., 2013, *The Astrophysical Journal*, 770, 138
- Lehner N., O'Meara J. M., Fox A. J., Howk J. C., Prochaska J. X., Burns V., Armstrong A. A., 2014, *The Astrophysical Journal*, 788, 119
- Lehner N., Wotta C. B., Howk J. C., O'Meara J. M., Oppenheimer B. D., Cooksey K. L., 2019, arXiv e-prints, p. arXiv:1902.10147
- Lehner N., et al., 2020, arXiv e-prints, 2002, arXiv:2002.07818
- Li J.-T., Bregman J. N., Wang Q. D., Crain R. A., Anderson M. E., 2018, *The Astrophysical Journal Letters*, 855, L24
- Liang C. J., Chen H.-W., 2014, *Monthly Notices of the Royal Astronomical Society*, 445, 2061
- Liang C. J., Kravtsov A. V., Agertz O., 2016, *Monthly Notices of the Royal Astronomical Society*, 458, 1164
- Lilly S. J., Carollo C. M., Pipino A., Renzini A., Peng Y., 2013, *The Astrophysical Journal*, 772, 119
- Lopez S., Reimers D., Gregg M. D., Wisotzki L., Wucknitz O., Guzman A., 2005, *The Astrophysical Journal*, 626, 767
- Macquart J.-P., et al., 2020, *Nature*, 581, 391
- Manuwal A., Narayanan A., Muzahid S., Charlton J. C., Khaire V., Chand H., 2019, *Monthly Notices of the Royal Astronomical Society*, 485, 30
- Martizzi D., et al., 2019, *Monthly Notices of the Royal Astronomical Society*, 486, 3766
- McCourt M., Oh S. P., O'Leary R., Madigan A.-M., 2018, *Monthly Notices of the Royal Astronomical Society*, 473, 5407
- McQuinn M., 2014, *The Astrophysical Journal Letters*, 780, L33
- Meiring J. D., Tripp T. M., Werk J. K., Howk J. C., Jenkins E. B., Prochaska J. X., Lehner N., Sembach K. R., 2013, *The Astrophysical Journal*, 767, 49
- Misawa T., Charlton J. C., Eracleous M., Ganguly R., Tytler D., Kirkman D., Suzuki N., Lubin D., 2007, *The Astrophysical Journal Supplement Series*, 171, 1
- Misawa T., Inada N., Ohsuga K., Gandhi P., Takahashi R., Oguri M., 2013, *The Astronomical Journal*, 145, 48
- Morton D. C., 2003, *The Astrophysical Journal Supplement Series*, 149, 205
- Mshar A. C., Charlton J. C., Lynch R. S., Churchill C., Kim T.-S., 2007, *The Astrophysical Journal*, 669, 135
- Muzahid S., 2014, *The Astrophysical Journal*, 784, 5
- Narayanan A., Wakker B. P., Savage B. D., 2009, *The Astrophysical Journal*, 703, 74
- Narayanan A., Wakker B. P., Savage B. D., Keeney B. A., Shull J. M., Stocke J. T., Sembach K. R., 2010, *The Astrophysical Journal*, 721, 960
- Narayanan A., et al., 2011, *The Astrophysical Journal*, 730, 15
- Narayanan A., Savage B. D., Wakker B. P., 2012, *The Astrophysical Journal*, 752, 65
- Narayanan A., Savage B. D., Mishra P. K., Wakker B. P., Khaire V., Wadadekar Y., 2018, *Monthly Notices of the Royal Astronomical Society*, 475, 3529
- Nielsen N. M., Churchill C. W., Kacprzak G. G., Murphy M. T., Evans J. L., 2015, *The Astrophysical Journal*, 812, 83
- Nomoto K., Tominaga N., Umeda H., Kobayashi C., Maeda K., 2006, *Nuclear Physics A*, 777, 424
- Nuza S. E., Parisi F., Scannapieco C., Richter P., GottlĀuber S., Steinmetz M., 2014, *Monthly Notices of the Royal Astronomical Society*, 441, 2593
- Oppenheimer B. D., Schaye J., 2013, *Monthly Notices of the Royal Astronomical Society*, 434, 1043
- Oppenheimer B. D., et al., 2016, *Monthly Notices of the Royal Astronomical Society*, 460, 2157
- Oppenheimer B. D., Segers M., Schaye J., Richings A. J., Crain R. A., 2018, *Monthly Notices of the Royal Astronomical Society*, 474, 4740

- Pachat S., Narayanan A., Muzahid S., Khaire V., Sriand R., Wakker B. P., Savage B. D., 2016, *Monthly Notices of the Royal Astronomical Society*, 458, 733
- Pachat S., Narayanan A., Khaire V., Savage B. D., Muzahid S., Wakker B. P., 2017, *Monthly Notices of the Royal Astronomical Society*, 471, 792
- Palanque-Delabrouille N., et al., 2013, *Astronomy and Astrophysics*, 551, A29
- Peeples M. S., Werk J. K., Tumlinson J., Oppenheimer B. D., Prochaska J. X., Katz N., Weinberg D. H., 2014, *The Astrophysical Journal*, 786, 54
- Peeples M. S., et al., 2019, *The Astrophysical Journal*, 873, 129
- Pitrou C., Coc A., Uzan J.-P., Vangioni E., 2018, *Physics Reports*, 754, 1
- Planck Collaboration et al., 2016, *Astronomy and Astrophysics*, 594, A16
- Pradeep J., Narayanan A., Muzahid S., Nagai D., Charlton J. C., Sriand R., 2019, *Monthly Notices of the Royal Astronomical Society*, 488, 5327
- Pradeep J., Sankar S., Umasree T. M., Narayanan A., Khaire V., Gebhardt M., Sameer Charlton J. C., 2020, *Monthly Notices of the Royal Astronomical Society*
- Prochaska J. X., Zheng Y., 2019, *Monthly Notices of the Royal Astronomical Society*, 485, 648
- Prochaska J. X., Weiner B., Chen H.-W., Mulchaey J., Cooksey K., 2011, *The Astrophysical Journal*, 740, 91
- Prochter G. E., Prochaska J. X., O'Meara J. M., Burles S., Bernstein R. A., 2010, *The Astrophysical Journal*, 708, 1221
- Qu Z., Bregman J. N., 2016, *The Astrophysical Journal*, 832, 189
- Rauch M., Sargent W. L. W., Barlow T. A., 2001a, *The Astrophysical Journal*, 554, 823
- Rauch M., Sargent W. L. W., Barlow T. A., Carswell R. F., 2001b, *The Astrophysical Journal*, 562, 76
- Ravi V., 2019, *The Astrophysical Journal*, 872, 88
- Ravi V., et al., 2019, *Nature*, 572, 352
- Reimers D., Vogel S., 1993, *Astronomy and Astrophysics*, 276, L13
- Richards G. T., York D. G., Yanny B., Kollgaard R. I., Laurent-Muehleisen S. A., Vanden Berk D. E., 1999, *The Astrophysical Journal*, 513, 576
- Richter P., 2020, arXiv e-prints, 2002, arXiv:2002.10486
- Richter P., Krause F., Fechner C., Charlton J. C., Murphy M. T., 2011, *Astronomy and Astrophysics*, 528, A12
- Richter P., Wakker B. P., Fechner C., Herenz P., Tepper-García T., Fox A. J., 2016, *Astronomy and Astrophysics*, 590, A68
- Roca-Fàbrega S., et al., 2019, *Monthly Notices of the Royal Astronomical Society*, 484, 3625
- Rodríguez Hidalgo P., Wessels K., Charlton J. C., Narayanan A., Mshar A., Cucchiara A., Jones T., 2012, *Monthly Notices of the Royal Astronomical Society*, 427, 1801
- Rosenwasser B., Muzahid S., Charlton J. C., Kacprzak G. G., Wakker B. P., Churchill C. W., 2018, *Monthly Notices of the Royal Astronomical Society*, 476, 2258
- Rudie G. C., Steidel C. C., Pettini M., Trainor R. F., Strom A. L., Hummels C. B., Reddy N. A., Shapley A. E., 2019, *The Astrophysical Journal*, 885, 61
- Savage B. D., Lehner N., 2006, *The Astrophysical Journal Supplement Series*, 162, 134
- Savage B. D., Sembach K. R., 1991, *The Astrophysical Journal*, 379, 245
- Savage B. D., Sembach K. R., Howk J. C., 2001, *The Astrophysical Journal*, 547, 907
- Savage B. D., Lehner N., Wakker B. P., Sembach K. R., Tripp T. M., 2005, *The Astrophysical Journal*, 626, 776
- Savage B. D., et al., 2010, *The Astrophysical Journal*, 719, 1526
- Savage B. D., Narayanan A., Lehner N., Wakker B. P., 2011, *The Astrophysical Journal*, 731, 14
- Savage B. D., Kim T.-S., Wakker B. P., Keeney B., Shull J. M., Stocke J. T., Green J. C., 2014, *The Astrophysical Journal Supplement Series*, 212, 8
- Schaye J., Carswell R. F., Kim T.-S., 2007, *Monthly Notices of the Royal Astronomical Society*, 379, 1169
- Schaye J., et al., 2015, *Monthly Notices of the Royal Astronomical Society*, 446, 521
- Shull J. M., Danforth C. W., 2018, *The Astrophysical Journal Letters*, 852, L11
- Shull J. M., Smith B. D., Danforth C. W., 2012, *The Astrophysical Journal*, 759, 23
- Shull J. M., Danforth C. W., Tilton E. M., 2014, *The Astrophysical Journal*, 796, 49
- Simcoe R. A., Sargent W. L. W., Rauch M., Becker G., 2006, *The Astrophysical Journal*, 637, 648
- Singh P., Majumdar S., Nath B. B., Silk J., 2018, *Monthly Notices of the Royal Astronomical Society*, 478, 2909
- Suresh J., Nelson D., Genel S., Rubin K. H. R., Hernquist L., 2019, *Monthly Notices of the Royal Astronomical Society*, 483, 4040
- Telfer R. C., Kriss G. A., Zheng W., Davidsen A. F., Tytler D., 2002, *The Astrophysical Journal*, 579, 500
- Thielemann F.-K., Bitouzet J.-P., Kratz K.-L., Mäüller P., Cowan J. J., Truran J. W., 1993, *Physics Reports*, 227, 269
- Tripp T. M., Sembach K. R., Bowen D. V., Savage B. D., Jenkins E. B., Lehner N., Richter P., 2008, *The Astrophysical Journal Supplement Series*, 177, 39
- Tripp T. M., et al., 2011, *Science*, 334, 952
- Tumlinson J., et al., 2011, *Science*, 334, 948
- Tumlinson J., Peeples M. S., Werk J. K., 2017, *Annual Review of Astronomy and Astrophysics*, 55, 389
- Veilleux S., Cecil G., Bland-Hawthorn J., 2005, *Annual Review of Astronomy and Astrophysics*, 43, 769
- Verner D. A., Ferland G. J., 1996, *The Astrophysical Journal Supplement Series*, 103, 467
- Wakker B. P., Savage B. D., 2009, *The Astrophysical Journal Supplement Series*, 182, 378
- Wakker B. P., Hernandez A. K., French D. M., Kim T.-S., Oppenheimer B. D., Savage B. D., 2015, *The Astrophysical Journal*, 814, 40
- Werk J. K., Prochaska J. X., Thom C., Tumlinson J., Tripp T. M., O'Meara J. M., Peeples M. S., 2013, *The Astrophysical Journal Supplement Series*, 204, 17
- Werk J. K., et al., 2014, *The Astrophysical Journal*, 792, 8
- Wotta C. B., Lehner N., Howk J. C., O'Meara J. M., Prochaska J. X., 2016, *The Astrophysical Journal*, 831, 95
- Wotta C. B., Lehner N., Howk J. C., O'Meara J., Oppenheimer B. D., Cooksey K. L., 2019, *The Astrophysical Journal*, 872, 81
- Zahedy F. S., Chen H.-W., Johnson S. D., Pierce R. M., Rauch M., Huang Y.-H., Weiner B. J., Gauthier J.-R., 2019, *Monthly Notices of the Royal Astronomical Society*, 484, 2257
- Zhang Y., Meiksin A., Anninos P., Norman M. L., 1998, *The Astrophysical Journal*, 495, 63
- Zinger E., Dekel A., Birnboim Y., Kravtsov A., Nagai D., 2016, *Monthly Notices of the Royal Astronomical Society*, 461, 412
- Zonak S. G., Charlton J. C., Ding J., Churchill C. W., 2004, *The Astrophysical Journal*, 606, 196

APPENDIX A: ESTIMATING THE IONIZATION DUE TO QUASAR FLUX AT $Z = 1.277$

Since the $z = 1.27768$ absorber is close to QSO emission redshift of $z_{\text{em}} = 1.328$, it is important to estimate whether the ionizing radiation ($\lambda < 912 \text{ \AA}$) from the QSO is going to have a significant impact on the absorber compared to the ionization brought about by the diffuse extragalactic UV background. The details of such a calculation is provided here.

The angle averaged specific intensity (j_{ν_0} in units $\text{erg s}^{-1} \text{ cm}^{-2} \text{ Hz}^{-1} \text{ sr}^{-1}$) of the radiation received by the absorber at z_{abs} from QSO at z_{em} is given by,

$$j_{\nu_0} = \frac{L_{\nu}^{\text{QSO}}}{(4\pi\Delta D_L)^2} e^{-\tau_{\text{eff}}(\nu_0, z_{\text{em}}, z_{\text{abs}})} \quad (\text{A1})$$

where L_{ν_0} is the specific intensity of the QSO radiation at frequency ν_0 (in units of $\text{erg s}^{-1} \text{ cm}^{-2} \text{ Hz}^{-1}$), $\Delta D_L = D_L(z_{\text{em}}) - D_L(z_{\text{abs}})$ where D_L is the luminosity distance, and $\tau_{\text{eff}}(\nu_0, z_{\text{em}}, z_{\text{abs}})$ is the effective optical depth suffered by ionizing photons travelling from z_{em} to z_{abs} which was emitted at frequency $\nu = (1 + z_{\text{em}})\nu_0/(1 + z_{\text{abs}})$. The intensity of QSO radiation L_{ν}^{QSO} at frequency ν can be obtained using flux calibrated COS QSO spectrum f_{ν} ,

$$L_{\nu}^{\text{QSO}} = f_{\nu} 4\pi D_L^2(z_{\text{em}}) e^{\tau_{\text{eff}}(\nu', z_{\text{em}}, 0)} \quad (\text{A2})$$

where $\tau_{\text{eff}}(\nu', z_{\text{em}}, 0)$ is the effective optical depth suffered by ionizing photons travelling from z_{em} to $z = 0$ which was emitted at frequency $\nu = \nu'(1 + z_{\text{em}})$. Therefore, combining Eq. A1 and A2,

$$j_{\nu_0} = \frac{f_{\nu} D_L^2(z_{\text{em}})}{4\pi(\Delta D_L)^2} e^{\tau_{\text{eff}}(\nu', z_{\text{abs}}, 0)}. \quad (\text{A3})$$

One can compare this j_{ν_0} to the one from extra-galactic UV background, however the spectral slopes of both can be different. Therefore, comparing the H I photoionization rates (Γ_{HI}) is more intuitive. The Γ_{HI} is defined as

$$\Gamma_{\text{HI}} = \int_{\nu_{\text{th}}}^{\infty} d\nu_0 \frac{4\pi j_{\nu_0}}{h\nu_0} \sigma_{\text{HI}}(\nu_0), \quad (\text{A4})$$

where, ν_{th} is a threshold frequency for ionization of H I, h is the Planck's constant, and σ_{HI} is the photoionization cross-section of hydrogen.

To crudely estimate an order of magnitude contribution from the QSO, we ignore the frequency dependence of the τ_{eff} in Eq. A3 and use power-law fits to the flux calibrated rest frame QSO spectrum $f_{\nu} = f_{\nu_{\text{th}}}(\nu/\nu_{\text{th}})^{-\alpha}$ and photoionization cross-section $\sigma_{\text{HI}}(\nu_0) = \sigma_{\text{HI}}(\nu_{\text{th}})(\nu_0/\nu_{\text{th}})^{-\beta}$ which simplifies Eq. A4 to

$$\Gamma_{\text{HI}} \approx \frac{f_{\nu_{\text{th}}} \sigma_{\text{HI}}(\nu_{\text{th}}) D_L^2(z_{\text{em}})}{h(\alpha + \beta)(\Delta D_L)^2} e^{\tau_{\text{eff}}(\nu', z_{\text{abs}}, 0)}, \quad (\text{A5})$$

We fit a power-law to the rest frame QSO spectra ($z_{\text{em}} = 1.328$) at $\lambda < 890 \text{ \AA}$ which is equivalent of fitting power law QSO spectra at $\lambda_{\text{abs}} < 912 \text{ \AA}$ at the absorber redshift $z_{\text{abs}} = 1.28$. We obtain $\alpha = 3.13$ and $f_{\nu_{\text{th}}} = 1.43 \times 10^{-27} \text{ erg s}^{-1} \text{ cm}^{-2} \text{ Hz}^{-1}$. Using the value of $\beta = 3$, $\sigma_{\text{HI}}(\nu_{\text{th}}) = 6.3 \times 10^{-18} \text{ cm}^2$ and luminosity distances obtained assuming flat cosmology parameters ($\Omega_m = 0.3$, $\Omega_{\Lambda} = 0.7$ and $H_0 = 70 \text{ km s}^{-1} \text{ Mpc}^{-1}$) we obtain $\Gamma_{\text{HI}} \approx 10^{-16} e^{\tau_{\text{eff}}(\nu', z_{\text{abs}}, 0)} \text{ s}^{-1}$ which is lower by four orders of magnitude than the fiducial value obtained using the KS19 extragalactic UV background at z_{abs} .

Given the fact that there are no DLAs along the sight-line and the contribution from IGM opacity to $e^{\tau_{\text{eff}}}$ is quite small at $z < 1$, the extragalactic UVB dominates the ionizing radiation received by absorber over the radiation from QSO by orders of magnitude.

Therefore we safely ignore the QSO contribution during the PIE modelling of this absorber.

APPENDIX B: ABSORPTION LINE MEASUREMENTS AND ABSORPTION SYSTEM VELOCITY PLOTS

The appendix contains full system plots of each absorber (See Figures from B1 to B5) and the line measurements of all detected and covered species in each of the systems (See Tables from B1 to B10)

This paper has been typeset from a $\text{\TeX}/\text{\LaTeX}$ file prepared by the author.

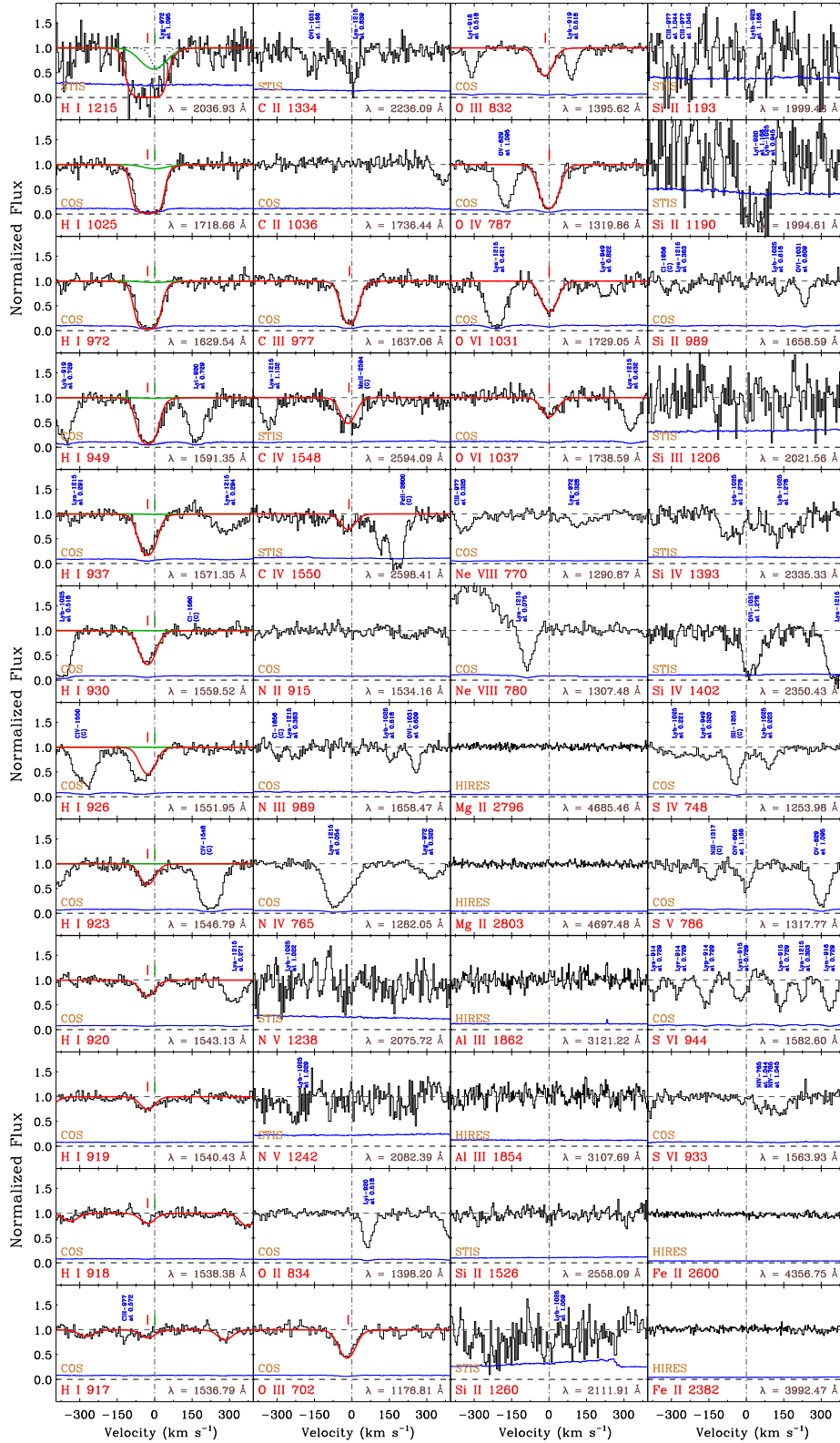


Figure B1. System plot of the $z_{abs}=0.67556$ absorber, with continuum-normalized flux along the Y-axis and the velocity scale relative to the redshift of the absorber along the X-axis. The $v = 0 \text{ km s}^{-1}$, marked by the *dashed-dotted* vertical line, indicates the absorber redshift. The 1σ uncertainty in flux is indicated by the *blue* curve at the bottom of each panel. The *red* curves are the best-fit Voigt profiles. The observed wavelength of each transition is also indicated in the respective panels. Interloping features unrelated to the absorber are also labeled.

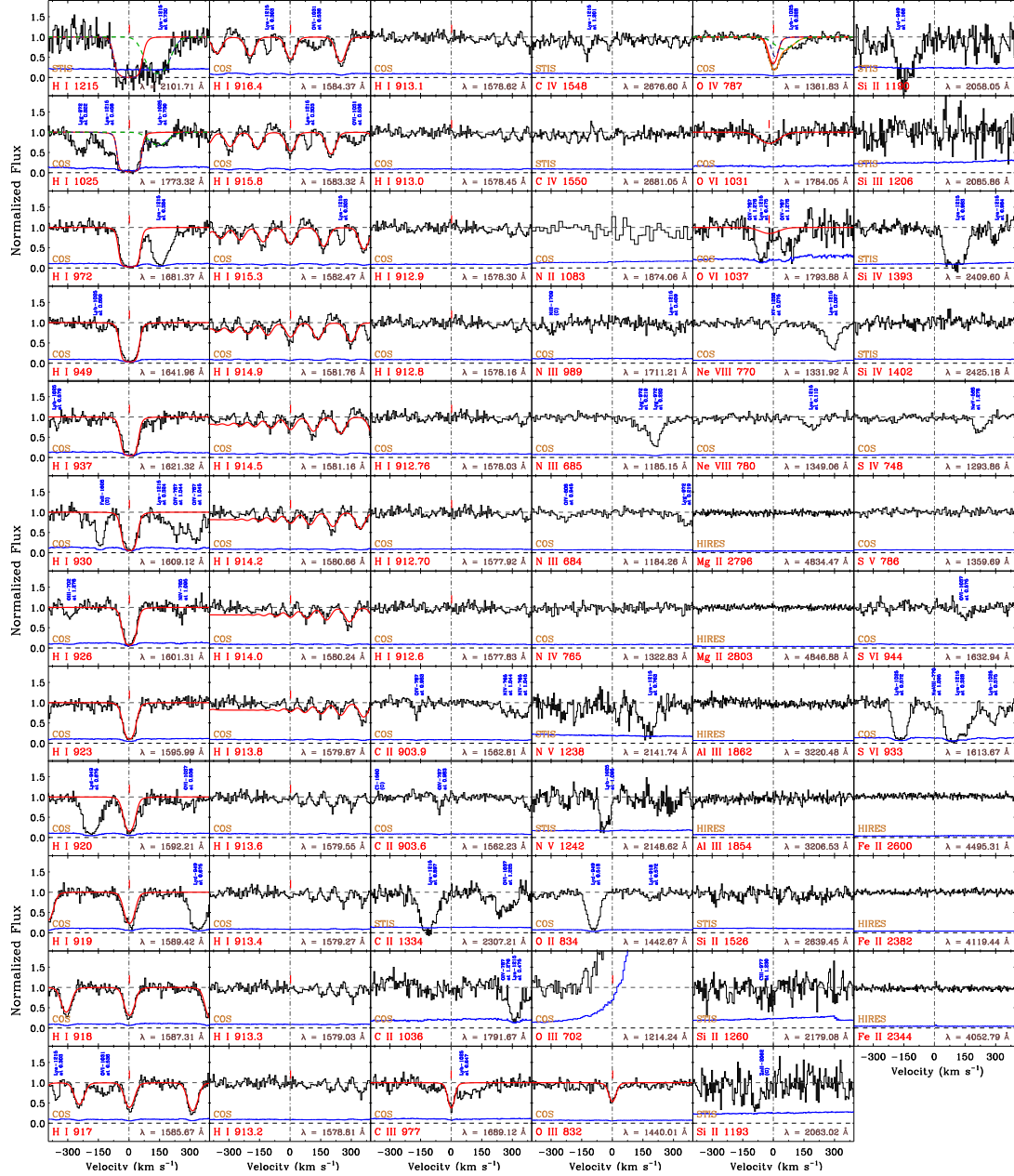


Figure B2. System plot of the $z_{abs}=0.72885$ absorber, with continuum-normalized flux along the Y-axis and the velocity scale relative to the redshift of the absorber along the X-axis. The $v = 0 \text{ km s}^{-1}$, marked by the *dashed-dotted* vertical line represents the absorber redshift. The 1σ uncertainty in flux is the *blue* curve at the bottom of each panel. The *red* curves are the best-fit Voigt profiles. The observed wavelength of each transition is also indicated in the respective panels. The dashed green curves in the H I 1215 Å and H I 1025 Å panels show a fit of the corresponding H I lines at $z \sim 0.730$ and the blue curve shows the composite fit. The O IV 787 Å is severely contaminated by H I 1025 Å at $z \sim 0.327$ and 0.328 . The contamination was accounted for in the fit and is displayed as dashed blue and green curve in the panel.

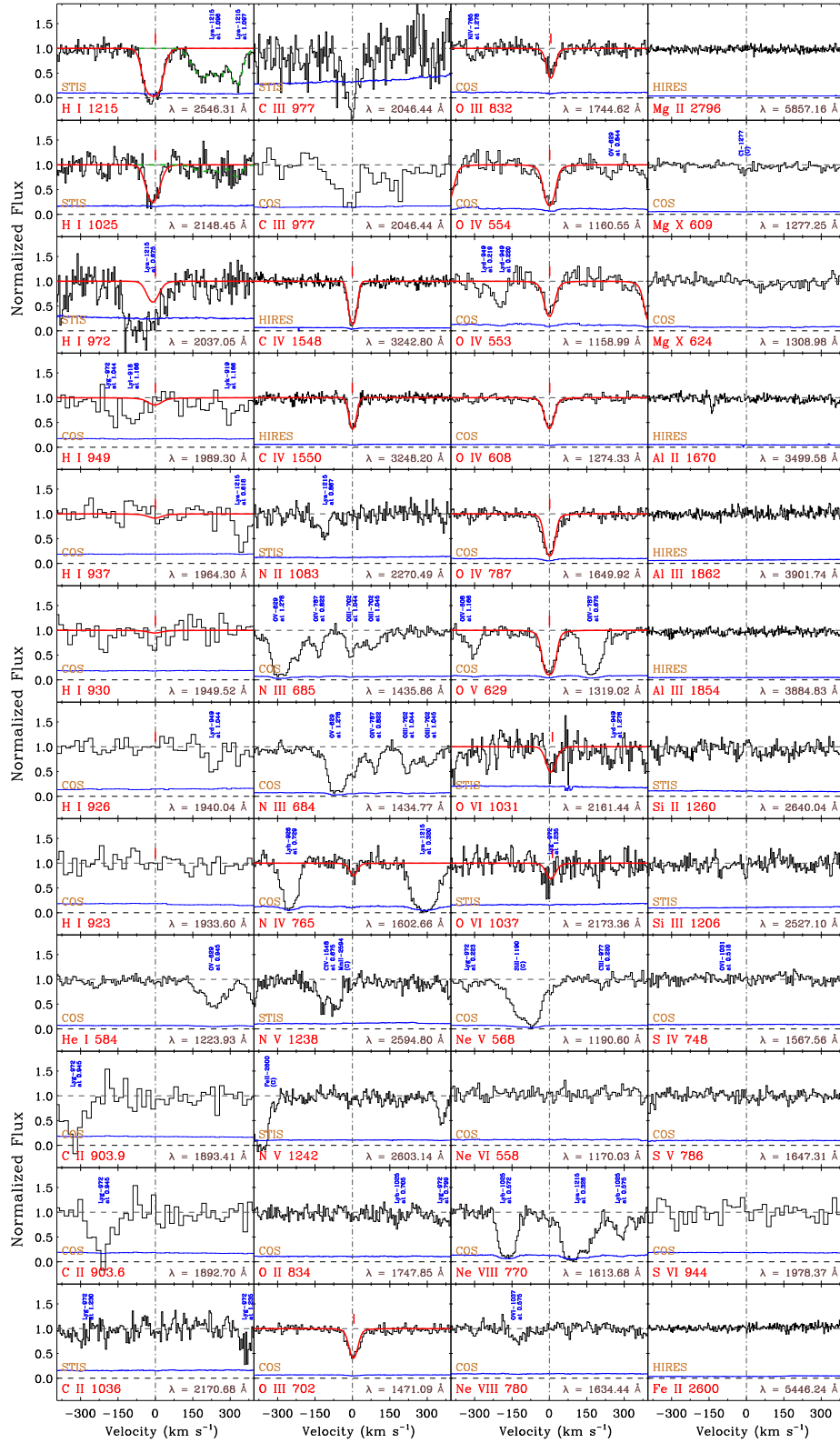


Figure B3. System plot of the $Z_{abs}=1.09457$ absorber, with continuum-normalized flux along the Y-axis and the velocity scale relative to the redshift of the absorber along the X-axis. The 1σ uncertainty in flux is indicated by the *blue* curve at the bottom of each panel. The *red* curves are the best-fit Voigt profiles. The observed wavelength of each transition is also indicated in the respective panels. The dashed green curves in the H I 1215 Å and H I 1025 Å panels show a three component fit of the corresponding H I lines at $z \sim 1.096$. The absorption seen at the location of C II 1334 in the FOS data is Galactic Mg II 2796. The C II ion is a non-detection as seen from the C II 1036 panel. Similarly, the strong absorption in the Ne V 568 panel is Galactic Si II 1190.

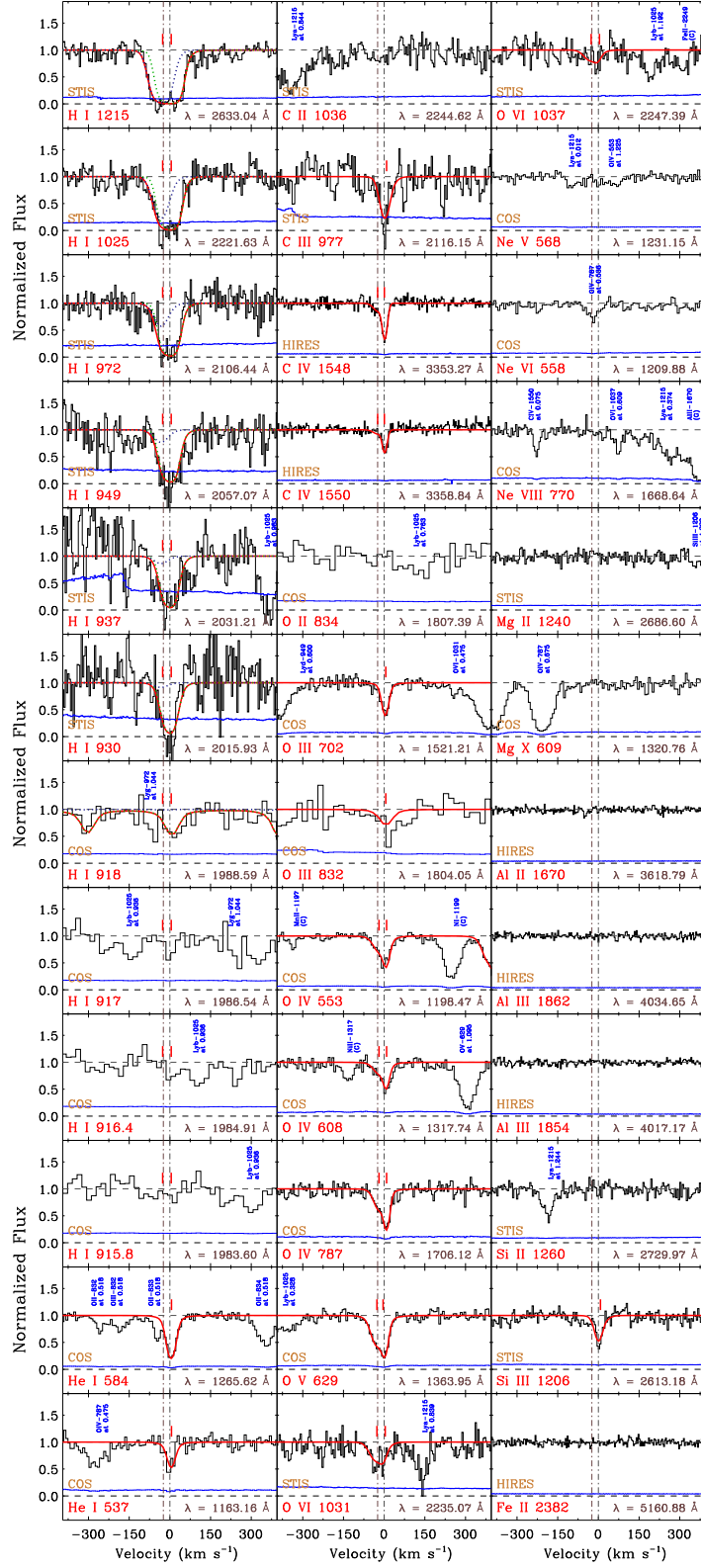


Figure B4. System plot of the $z_{abs}=1.16592$ absorber, with continuum-normalized flux along the Y-axis and the velocity scale relative to the redshift of the absorber along the X-axis. The $v = 0 \text{ km s}^{-1}$, marked by the *dashed-dotted* vertical line, indicates the absorber redshift. The 1σ uncertainty in flux is indicated by the *blue* curve at the bottom of each panel. The *red* curves are the best-fit Voigt profiles. The observed wavelength of each transition is also indicated in the respective panels.

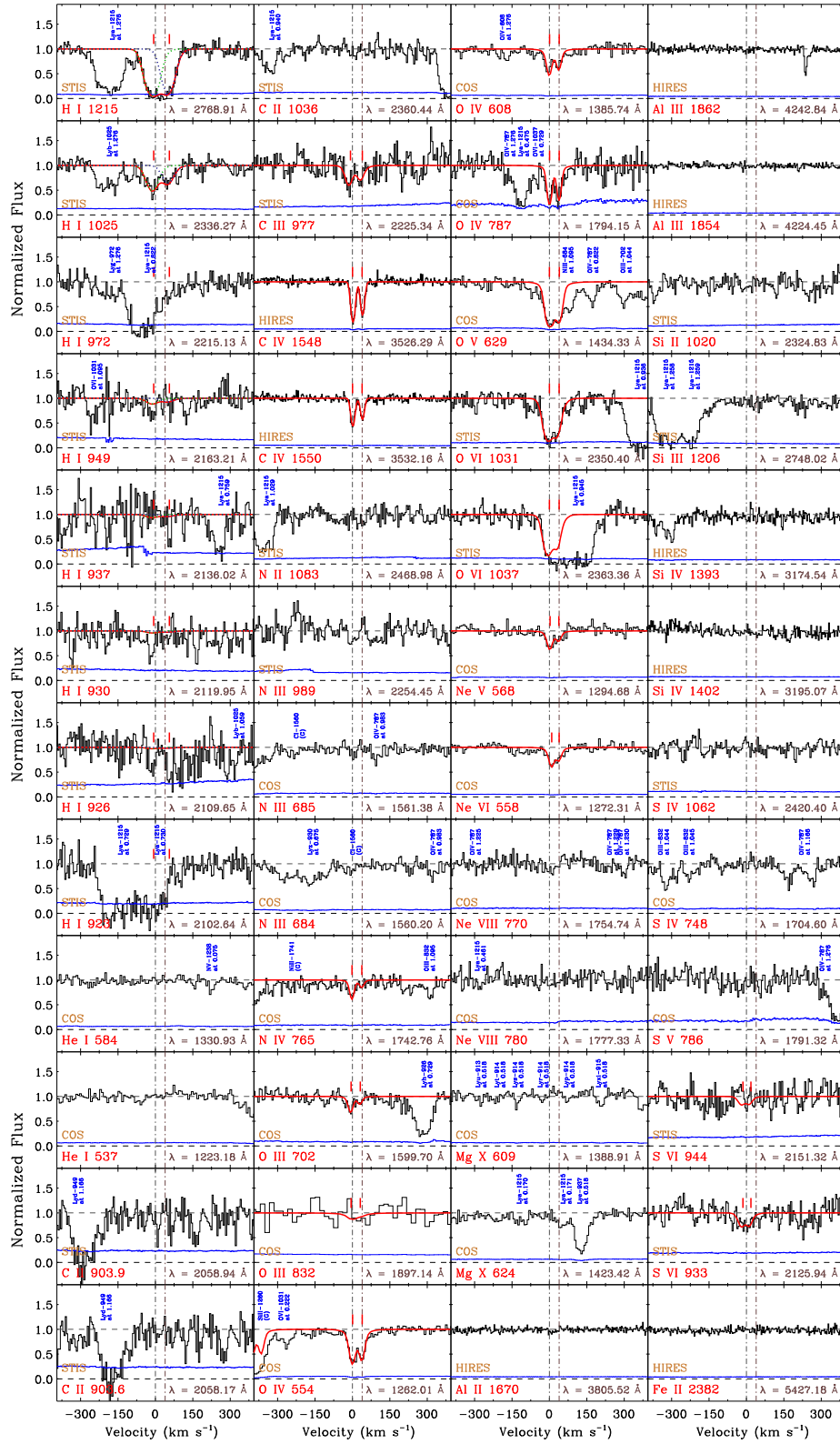


Figure B5. System plot of the $z_{abs}=1.27768$ absorber, with continuum-normalized flux along the Y-axis and the velocity scale relative to the redshift of the absorber along the X-axis. The $v = 0 \text{ km s}^{-1}$, marked by the *dashed-dotted* vertical line, indicates the absorber redshift. The 1σ uncertainty in flux is indicated by the *blue* curve at the bottom of each panel. The *red* curves are the best-fit Voigt profiles. The observed wavelength of each transition is also indicated in the respective panels.

Table B1. Line measurements for the $z_{abs} = 0.67556$ absorber towards PG 1522 + 101 with the successive columns indicating the equivalent width in the rest-frame of the absorber, the column density measured using the AOD method, or the Voigt profile measured column density and Doppler b parameter. The final column shows the velocity range over which the equivalent width and apparent column densities were integrated, or the velocity centroid for the profile-fitted absorption components. For lines that are not detected with a significance of $\geq 3\sigma$, upper limits are quoted for the equivalent width and the corresponding column density is obtained from the linear part of the curve of growth. The H I 926 line suffers from contamination. ^c - contaminated lines.

Line	$W_r(mA^\circ)$	$\log[N (cm^{-2})]$	$b (km s^{-1})$	$v (km s^{-1})$
H I 1215	> 635	> 14.4		[-145, 95]
H I 1025	> 451	> 15.3		[-110, 85]
H I 972	346 ± 8	15.52 ± 0.04		[-110, 85]
H I 949	298.4 ± 9	15.73 ± 0.03		[-110, 85]
H I 937	212 ± 8	15.75 ± 0.02		[-110, 85]
H I 930	166 ± 8	15.80 ± 0.01		[-110, 85]
H I 926	213 ± 7	16.11 ± 0.01		[-110, 85]
H I 923	112 ± 8	15.90 ± 0.02		[-110, 85]
H I 920	81 ± 8	15.89 ± 0.02		[-110, 85]
H I 919	84 ± 9	16.02 ± 0.02		[-110, 85]
H I 918	< 25	< 15.5		[-110, 85]
H I 917	< 25	< 15.6		[-110, 85]
H I		15.87 ± 0.04	36 ± 2	-28 ± 3
H I		< 13.7	< 64	1 ± 8
C II 1334 ^c	< 197	< 14.1		[-80, 70]
C II 1036	< 34	< 13.4		[-80, 70]
C III 977	236 ± 7	13.82 ± 0.02		[-80, 70]
C III		13.90 ± 0.10	33 ± 6	-10 ± 4
C IV 1548	291 ± 15	14.01 ± 0.03		[-80, 70]
C IV 1550	137 ± 15	13.89 ± 0.04		[-80, 70]
C IV		13.83 ± 0.25	33 ± 8	-12 ± 18
N II 915	< 22	< 13.3		[-80, 70]
N III 989	< 29	< 13.5		[-80, 70]
N IV 765 ^c	< 192	< 14.03		[-80, 70]
N V 1238	< 86	< 13.6		[-80, 70]
N V 1242	< 77	< 13.8		[-80, 70]
O II 834	< 18	< 13.3		[-80, 70]
O III 702	98 ± 6	14.33 ± 0.01		[-80, 70]
O III 832	130 ± 5	14.42 ± 0.01		[-80, 60]
O III		14.43 ± 0.07	36 ± 6	-15 ± 6
O IV 787	210 ± 6	14.83 ± 0.02		[-80, 70]
O IV		14.97 ± 0.16	33 ± 8	1 ± 5
O VI 1031	171 ± 9	14.28 ± 0.02		[-80, 70]
O VI 1037	93 ± 11	14.25 ± 0.04		[-80, 70]
O VI		14.31 ± 0.10	39 ± 11	1 ± 8

Table B2. Table of line measurements for the $z=0.67556$ absorber towards PG 1522 + 101, continued from Table B1. ^c - contaminated lines.

Line	$W_r(mA^\circ)$	$\log[N (cm^{-2})]$	$b (km s^{-1})$	$v (km s^{-1})$
Ne VIII 770	< 15	< 13.4		[-80, 70]
Ne VIII 780	< 21	< 13.8		[-80, 70]
Mg II 2796	< 27	< 11.8		[-80, 70]
Mg II 2803	< 26	< 12.0		[-80, 70]
Al III 1862	< 53	< 12.8		[-80, 70]
Al III 1854	< 56	< 12.5		[-80, 70]
Si II 1526	< 43	< 13.2		[-80, 70]
Si II 1260 ^c	< 117	< 13.0		[-80, 70]
Si II 1193 ^c	< 221	< 13.7		[-80, 70]
Si II 1190 ^c	< 333	< 13.8		[-80, 70]
Si II 989	< 29	< 13.2		[-80, 70]
Si III 1206	< 108	< 12.7		[-80, 70]
Si IV 1393 ^c	< 204	< 13.5		[-80, 70]
Si IV 1402 ^c	< 351	< 14.2		[-80, 70]
S IV 748	< 12	< 12.6		[-80, 70]
S V 786 ^c	< 77	< 13.1		[-80, 70]
S VI 944 ^c	< 46	< 13.6		[-80, 70]
S VI 933	< 23	< 12.8		[-80, 70]
Fe II 2600	< 22	< 12.2		[-80, 70]
Fe II 2382	< 23	< 12.1		[-80, 70]

Table B3. Line measurements for the $z_{abs} = 0.72885$ absorber towards PG 1522 + 101 with the successive columns indicating the equivalent width in the rest-frame of the absorber, the column density measured using the AOD method, or the Voigt profile measured column density and Doppler b parameter. The final column shows the velocity range over which the equivalent width and apparent column densities were integrated, or the velocity centroid for the profile-fitted absorption components. ^c - contaminated lines.

Line	$W_r(m\text{\AA}^o)$	$\log[N (cm^{-2})]$	$b (km s^{-1})$	$v (km s^{-1})$
H I 1215	> 565	> 14.1		[-70, 80]
H I 1025	> 434	> 15.2		[-70, 80]
H I 972	352 ± 6	15.62 ± 0.32		[-70, 80]
H I 949	297 ± 6	15.80 ± 0.05		[-70, 80]
H I 937	287 ± 9	16.03 ± 0.11		[-70, 80]
H I 930	241 ± 8	16.16 ± 0.08		[-70, 80]
H I 926	206 ± 9	16.26 ± 0.06		[-70, 80]
H I 923	212 ± 7	16.41 ± 0.03		[-70, 80]
H I 920	196 ± 6	16.49 ± 0.03		[-45, 50]
H I 919	182 ± 5	16.56 ± 0.02		[-45, 50]
H I 918	137 ± 6	16.50 ± 0.02		[-45, 50]
H I 917	124 ± 6	16.53 ± 0.02		[-45, 50]
H I 916.4	97 ± 6	16.49 ± 0.02		[-45, 50]
H I 915.8	82 ± 7	16.49 ± 0.02		[-45, 50]
H I 915.3	65 ± 6	16.44 ± 0.02		[-45, 50]
H I 914.9	67 ± 6	16.56 ± 0.02		[-45, 50]
H I 914.5	31 ± 7	16.25 ± 0.04		[-45, 50]
H I 914.2	36 ± 7	16.39 ± 0.03		[-45, 50]
H I 914.0	< 15	< 16.1		[-45, 50]
H I 913.8	< 20	< 16.3		[-45, 50]
H I 913.6	< 19.4	< 16.2		[-45, 50]
H I 913.4	< 19.2	< 16.3		[-45, 50]
H I 913.3	< 19.4	< 16.3		[-45, 50]
H I 913.2	< 19.6	< 16.4		[-45, 50]
H I 913.1	< 19.9	< 16.4		[-45, 50]
H I 913.0	< 19.7	< 16.5		[-45, 50]
H I 912.9	< 20.0	< 16.5		[-45, 50]
H I 912.8	< 20.6	< 16.6		[-45, 50]
H I 912.76	< 20.5	< 16.6		[-45, 50]
H I 912.70	< 20.4	< 16.7		[-45, 50]
H I 912.6	< 20.5	< 16.7		[-45, 50]
H I		16.50 ± 0.02	26 ± 3	2 ± 1
C II 903.9	< 15.6	< 12.8		[-30, 30]
C II 903.6	< 14.9	< 13.0		[-30, 30]
C II 1334	< 30.9	< 13.1		[-30, 30]
C II 1036	< 38.4	< 13.5		[-30, 30]
C III 977	80 ± 6	13.24 ± 0.02		[-30, 30]
C III		13.34 ± 0.05	17 ± 3	1 ± 2

Table B4. Table of line measurements for the $z=0.72885$ absorber towards PG 1522 + 101, continued from Table B3. ^c - contaminated lines.

Line	$W_r(m\text{\AA}^o)$	$\log[N (cm^{-2})]$	$b (km s^{-1})$	$v (km s^{-1})$
C IV 1548 ^c	< 41	< 13.1		[-30, 30]
C IV 1550 ^c	< 31	< 13.2		[-30, 30]
N II 1083	< 59	< 13.7		[-30, 30]
N III 989	< 22	< 13.3		[-30, 30]
N III 685	< 11	< 13.0		[-30, 30]
N III 684	< 11	< 13.3		[-30, 30]
N IV 765	< 14	< 12.6		[-30, 30]
N V 1238 ^c	< 55	< 13.5		[-30, 30]
N V 1242 ^c	< 84	< 14.1		[-30, 30]
O II 834	< 12.7	< 13.1		[-30, 30]
O III 832	53 ± 4	14.01 ± 0.01		[-30, 30]
O III		14.10 ± 0.06	19 ± 4	2 ± 2
O IV 787	114 ± 3	14.51 ± 0.01		[-30, 30]
O IV		14.43 ± 0.12	22 ± 4	1 ± 4
O VI 1031	92 ± 15	13.94 ± 0.08		[-100, 50]
O VI 1037	60 ± 12	14.07 ± 0.10		[-30, 30]
O VI		14.00 ± 0.07	61 ± 11	-21 ± 8
Ne VIII 770 ^c	< 21	< 13.6		[-30, 30]
Ne VIII 780	< 11	< 13.6		[-30, 30]
Mg II 2796	< 16	< 11.5		[-30, 30]
Mg II 2803	< 15	< 11.8		[-30, 30]
Al III 1862	< 18	< 12.3		[-30, 30]
Al III 1854	< 21	< 12.1		[-30, 30]
Si II 1526	< 30	< 13.0		[-30, 30]
Si II 1260	< 51	< 12.4		[-30, 30]
Si II 1193	< 56	< 12.8		[-30, 30]
Si II 1190	< 51	< 13.1		[-30, 30]
Si II 989	< 21	< 13.1		[-30, 30]
Si III 1206	< 55	< 12.4		[-30, 30]
Si IV 1393	< 26	< 12.4		[-30, 30]
Si IV 1402	< 24	< 12.7		[-30, 30]
S IV 748	< 11	< 12.6		[-30, 30]
S V 786	< 12	< 12.1		[-30, 30]
S VI 944	< 16	< 12.9		[-30, 30]
S VI 933 ^c	< 33	< 13.0		[-30, 30]
Fe II 2600	< 14	< 12.0		[-30, 30]
Fe II 2382	< 15	< 11.9		[-30, 30]
Fe II 2344	< 17	< 12.4		[-30, 30]

Table B5. Line measurements for the $z_{abs} = 1.09457$ absorber towards PG 1522 + 101 with the successive columns indicating the equivalent width in the rest-frame of the absorber, the column density measured using the AOD method, or the Voigt profile measured column density and Doppler b parameter. The final column shows the velocity range over which the equivalent width and apparent column densities were integrated, or the velocity centroid for the profile-fitted absorption components. (a) - STIS Spectra. continued in Table B6. ^c - contaminated lines.

Line	W_r (mÅ)	$\log[N$ (cm^{-2})]	b (km s $^{-1}$)	v (km s $^{-1}$)
H I 1215	348 ± 9	13.99 ± 0.25		[-70, 50]
H I 1025	153 ± 14	14.55 ± 0.18		[-70, 50]
H I 972	< 301	< 15.2		[-70, 50]
H I 949	< 80	< 14.8		[-70, 50]
H I 937	< 83	< 15.1		[-70, 50]
H I 930	< 86	< 15.3		[-70, 50]
H I 926	< 62	< 15.4		[-70, 50]
H I 923	< 86	< 15.7		[-70, 50]
H I		14.65 ± 0.15	25 ± 3	-4 ± 2
He I 584	< 10	< 13.0		[-40, 35]
C II 903.9	< 66	< 13.4		[-40, 35]
C II 903.6	< 68	< 13.7		[-40, 35]
C II 1036	< 32	< 13.4		[-40, 35]
C III 977	194 ± 20	13.76 ± 0.16		[-40, 35]
C III 977(a)	> 215	> 13.6		[-40, 35]
C IV 1548	179 ± 5	13.91 ± 0.01		[-40, 35]
C IV 1550	113 ± 5	13.89 ± 0.01		[-40, 35]
C IV		13.91 ± 0.02	18 ± 1	-1 ± 1
N II 1083	< 25	< 13.3		[-40, 35]
N II 915	< 67	< 13.7		[-40, 35]
N III 685	62 ± 3	13.85 ± 0.01		[-40, 35]
N III 684	108 ± 3	14.52 ± 0.01		[-40, 35]
N IV 765	20 ± 6	12.85 ± 0.07		[-40, 35]
N IV		12.96 ± 0.36	17 ± 2	4 ± 3
N V 1238	< 29	< 13.1		[-40, 35]
N V 1242	< 26	< 13.3		[-40, 35]
O II 834	< 18	< 13.3		[-40, 35]
O III 702	77 ± 4	14.23 ± 0.01		[-55, 55]
O III 832	68 ± 7	14.12 ± 0.03		[-55, 55]
O III		14.23 ± 0.06	18 ± 3	6 ± 2
O IV 554	100 ± 5	14.42 ± 0.02		[-55, 55]
O IV 553	69 ± 6	14.49 ± 0.03		[-55, 55]
O IV 608	62 ± 3	14.57 ± 0.01		[-55, 55]
O IV 787	137 ± 5	14.56 ± 0.02		[-55, 55]
O IV		14.69 ± 0.05	18 ± 3	1 ± 2
O V 629	127 ± 4	14.09 ± 0.01		[-55, 55]
O V		14.63 ± 0.18	18 ± 2	0 ± 2

Table B6. Table of line measurements for the $z=1.09457$ absorber towards PG 1522 + 101, continued from Table B5. ^c - contaminated lines.

Line	W_r (mÅ)	$\log[N$ (cm^{-2})]	b (km s $^{-1}$)	v (km s $^{-1}$)
O VI 1031	59 ± 16	13.84 ± 0.17		[-55, 55]
O VI 1037	80 ± 13	14.25 ± 0.10		[-55, 55]
O VI		14.03 ± 0.17	18 ± 4	12 ± 8
Ne V 568 ^c	< 52	< 14.4		[-40, 35]
Ne VI 558	< 15	< 13.7		[-40, 35]
Ne VIII 770 ^c	< 32	< 13.8		[-40, 35]
Ne VIII 780	< 15	< 13.7		[-40, 35]
Mg II 2796	< 17	< 11.6		[-40, 35]
Mg X 609 ^c	< 14	< 13.7		[-40, 35]
Mg X 624	< 11	< 13.8		[-40, 35]
Al II 1670	< 13	< 11.4		[-40, 35]
Al III 1862	< 19	< 12.3		[-40, 35]
Al III 1854	< 13	< 11.9		[-40, 35]
Si II 1260	< 26	< 12.2		[-40, 35]
Si II 1193	< 29	< 12.5		[-40, 35]
Si II 1190	< 23	< 12.7		[-40, 35]
Si III 1206	< 25	< 12.0		[-40, 35]
Si IV 1393	< 20	< 12.3		[-40, 35]
S IV 748	< 14	< 12.7		[-40, 35]
S V 786	< 16	< 12.3		[-40, 35]
S VI 944	< 69	< 13.6		[-40, 35]
S VI 933	< 75	< 13.3		[-40, 35]
Fe II 2600	< 15	< 12.0		[-40, 35]
Fe II 2382	< 15	< 11.9		[-40, 35]
Fe II 2344	< 17	< 12.4		[-40, 35]

Table B7. Line measurements for the $z_{abs} = 1.16592$ absorber towards PG 1522+101 with the successive columns indicating the equivalent width in the rest-frame of the absorber, the column density measured using the AOD method, or the Voigt profile measured column density and Doppler b parameter. The final column shows the velocity range over which the equivalent width and apparent column densities were integrated, or the velocity centroid for the profile-fitted absorption components. ^c - contaminated lines.

Line	$W_r(mA^\circ)$	$\log[N (cm^{-2})]$	$b (km s^{-1})$	$v (km s^{-1})$
H I 1215	> 541	> 14.3		[-100, 65]
H I 1025	> 374	> 14.9		[-100, 65]
H I 972	> 274	> 15.2		[-100, 65]
H I 949	> 304	> 15.6		[-100, 65]
H I 937	> 280	> 15.9		[-100, 65]
H I 930	> 187	> 15.8		[-100, 65]
H I 918	115 ± 24	16.34 ± 0.08		[-35, 70]
H I 917	< 73	< 16.1		[-35, 70]
H I 916.4	< 74	< 16.2		[-35, 70]
H I 915.8	< 75	< 16.3		[-35, 70]
H I		16.52 ± 0.11	21 ± 1	5 ± 2
		14.69 ± 0.16	29 ± 3	-27 ± 6
He I 584	75 ± 2	14.15 ± 0.01		[-30, 50]
He I 537	32 ± 4	14.36 ± 0.03		[-35, 30]
He I		14.48 ± 0.17	14 ± 3	6 ± 2
C II 1036 ^c	< 37	< 13.6		[-30, 50]
C III 977	114 ± 17	13.33 ± 0.50		[-30, 50]
C III		13.81 ± 0.70	14 ± 2.0	9 ± 11
C IV 1548	97 ± 5	13.53 ± 0.01		[-30, 50]
C IV 1550	49 ± 5	13.47 ± 0.01		[-30, 50]
C IV		13.45 ± 0.10	11 ± 2	1 ± 1
		12.93 ± 0.33	23 ± 14	-24 ± 15
O II 834	< 58	< 13.8		[-30, 50]
O III 702	53 ± 4	14.06 ± 0.01		[-30, 50]
O III 832	88 ± 22	14.28 ± 0.12		[-30, 50]
O III		14.18 ± 0.14	12 ± 2	6 ± 3
O IV 554	100 ± 2	14.47 ± 0.01		[-30, 50]
O IV 553	55 ± 3	14.36 ± 0.01		[-50, 50]
O IV 608	56 ± 4	14.51 ± 0.01		[-50, 50]
O IV 787	101 ± 6	14.38 ± 0.02		[-50, 50]
O IV		14.36 ± 0.12	10 ± 1	9 ± 2
		13.98 ± 0.12	22 ± 7	-19 ± 6
O V 629	106 ± 4	13.95 ± 0.01		[-85, 45]
O V		13.94 ± 0.17	10 ± 1	4 ± 3
		13.67 ± 0.17	22 ± 7	-27 ± 7
O VI 1031	104 ± 13	14.03 ± 0.07		[-85, 45]
O VI 1037	54 ± 13	14.02 ± 0.09		[-85, 45]
O VI		13.61 ± 0.20	10 ± 2	4 ± 3
		13.78 ± 0.14	23 ± 7	-27 ± 7

Table B8. Table of line measurements for the $z=1.16592$ absorber towards PG1522+101, continued from Table B7. ^c - contaminated lines.

Line	$W_r(mA^\circ)$	$\log[N (cm^{-2})]$	$b (km s^{-1})$	$v (km s^{-1})$
Ne V 568 ^c	< 16	< 13.7		[-30, 50]
Ne VI 558 ^c	< 21	< 14.0		[-30, 50]
Ne VIII 770	< 16	< 13.4		[-30, 50]
Ne VIII 780	< 18	< 13.8		[-30, 50]
Mg II 1240	< 21	< 16.0		[-30, 50]
Mg X 609	< 13	< 13.6		[-30, 50]
Al II 1670	< 11	< 11.3		[-30, 50]
Al III 1862	< 13	< 12.2		[-30, 50]
Al III 1854	< 12	< 11.8		[-30, 50]
Si II 1260	< 24	< 12.1		[-30, 50]
Si II 1193	< 21	< 12.4		[-30, 50]
Si II 1190 ^c	< 31	< 13.0		[-30, 50]
Si III 1206	75 ± 7	12.66 ± 0.02		[-30, 50]
Si III		12.80 ± 0.40	11	8 ± 7
Fe II 2600	< 19	< 12.1		[-30, 50]
Fe II 2382	< 16	< 12.0		[-30, 50]
Fe II 2344	< 17	< 12.4		[-30, 50]

Table B9. Line measurements for the $z_{abs} = 1.27768$ absorber towards PG1522+101 with the successive columns indicating the corresponding equivalent width in the rest-frame of the absorber, the column density measured through the AOD method or Voigt profile fitting and the Doppler parameters obtained through profile fitting. The final column shows the velocity range over which the equivalent width and apparent column densities were integrated, or the centroid for the profile-fitted absorption components. Continued in Table B10. ^c - contaminated lines.

Line	$W_r(m\text{\AA}^o)$	$\log[N(\text{cm}^{-2})]$	$b(\text{km s}^{-1})$	$v(\text{km s}^{-1})$
H I 1215	> 502	> 14		[-45, 115]
H I 1025	178 ± 12	14.49 ± 0.04		[-45, 115]
H I 972 ^c	< 284	< 15.3		[-45, 115]
H I 949	60 ± 16	14.84 ± 0.14		[-45, 115]
H I 937	< 64	< 15		[-45, 115]
H I 930 ^c	< 90	< 15.5		[-45, 115]
H I 926 ^c	< 136	< 16.0		[-45, 115]
H I 923 ^c	< 331	< 16.4		[-45, 115]
H I		14.31 ± 0.09	25 ± 5	-7 ± 6
		14.09 ± 0.11	24 ± 6	56 ± 7
He I 584	< 10	< 13.0		[-30, 60]
He I 537	< 9	< 13.6		[-30, 60]
C II 903.9	< 45	< 13.2		[-30, 60]
C II 903.6	< 46	< 13.5		[-30, 60]
C II 1334	< 25	< 13.0		[-30, 60]
C II 1036	< 27	< 13.3		[-30, 60]
C III 977	74 ± 12	13.17 ± 0.09		[-30, 60]
C III		13.10 ± 0.16	10 ± 1	-8 ± 5
		12.84 ± 0.21	10 ± 2	40 ± 8
C IV 1548	173 ± 4	13.82 ± 0.01		[-30, 60]
C IV 1550	107 ± 4	13.82 ± 0.01		[-30, 60]
C IV		13.61 ± 0.02	10 ± 1	0 ± 1
		13.42 ± 0.02	10 ± 2	39 ± 1
N II 1083	< 29	< 13.4		[-30, 60]
N II 915	< 50	< 13.6		[-30, 60]
N III 989	< 33	< 13.5		[-30, 60]
N III 685	< 12	< 13.0		[-30, 60]
N III 684	< 12	< 13.3		[-30, 60]
N IV 765	37 ± 5	13.11 ± 0.03		[-30, 60]
N IV		13.01 ± 0.10	9 ± 1	-2 ± 2
		12.49 ± 0.23	9 ± 2	38 ± 7
N V 1238	< 13	< 12.7		[-30, 60]
N V 1242	< 14	< 13.1		[-30, 60]
O III 702	29 ± 4.47	13.74 ± 0.03		[-30, 60]
O III 832	< 54	< 13.9		[-30, 60]
O III		13.66 ± 0.11	9 ± 1	-5 ± 4
		13.25 ± 0.22	9 ± 2	32 ± 7

Table B10. Table of line measurements for the $z=1.27768$ absorber towards PG1522+101, continued from Table B9. ^c - contaminated lines.

Line	$W_r(m\text{\AA}^o)$	$\log[N(\text{cm}^{-2})]$	$b(\text{km s}^{-1})$	$v(\text{km s}^{-1})$
O IV 554	80 ± 2	14.28 ± 0.00		[-30, 60]
O IV 608	55 ± 3	14.49 ± 0.01		[-30, 60]
O IV 787	119 ± 10	14.48 ± 0.10		[-30, 60]
O IV		14.44 ± 0.07	9 ± 1	1 ± 1
		14.23 ± 0.07	8 ± 2	39 ± 1
O V 629	144 ± 2	14.19 ± 0.01		[-30, 60]
O V		14.69 ± 0.30	12 ± 2	0 ± 1
		14.03 ± 0.19	10 ± 2	40 ± 1
O VI 1031	> 220	> 14.57		[-20, 75]
O VI 1037	> 281	> 15.11		[-20, 75]
O VI		15.55 ± 0.67	10	-1 ± 4
		14.53 ± 0.89	9 ± 3	39 ± 5
Ne V 568	33 ± 3	14.08 ± 0.01		[-20, 75]
Ne V		14.02 ± 0.11	8 ± 1	3 ± 3
		13.64 ± 0.16	8 ± 2	38 ± 5
Ne VI 558	40 ± 2	14.26 ± 0.01		[-20, 75]
Ne VI		14.13 ± 0.09	8 ± 1	9 ± 3
		13.86 ± 0.12	8 ± 2	39 ± 4
Ne VIII 770	< 17	< 13.5		[-30, 60]
Ne VIII 780	< 26	< 13.9		[-30, 60]
Mg X 609	< 10	< 13.5		[-30, 60]
Mg X 624	< 9	< 13.8		[-30, 60]
Al II 1670	< 12	< 11.4		[-30, 60]
Al III 1862	< 14	< 12.2		[-30, 60]
Al III 1854	< 13	< 11.9		[-30, 60]
Si II 1260	< 18	< 12.0		[-30, 60]
Si II 1020	< 28	< 14.2		[-30, 60]
Si III 1206	< 23	< 12.0		[-30, 60]
Si IV 1393	< 22	< 12.4		[-30, 60]
Si IV 1402	< 19	< 12.6		[-30, 60]
S IV 1062	< 26	< 13.8		[-30, 60]
S IV 748	< 16	< 12.8		[-30, 60]
S V 786	< 32	< 12.6		[-30, 60]
S VI 944	< 39	< 13.3		[-20, 75]
S VI 933	63 ± 13	13.33 ± 0.11		[-20, 75]
S VI		13.13 ± 0.10	6 ± 3	-14 ± 10
		13.05 ± 0.11	6 ± 3	18 ± 12
Fe II 2382	< 17	< 12.0		[-30, 60]
Fe II 2344	< 16	< 12.4		[-30, 60]